

The Impact of Irrigated Biomass Plantations on Mesoscale Climate in Coastal Arid Regions

by Oliver Branch



The Impact of Irrigated Biomass Plantations on Mesoscale Climate in Coastal Arid Regions

Dissertation zur Erlangung des Doktorgrades
der Naturwissenschaften (Dr. rer. nat.)

Fakultät Naturwissenschaften
Universität Hohenheim

Institut für Physik und Meteorologie (IPM)

vorgelegt von
Oliver Branch

aus York, UK
2014



Dekan: Prof. Dr. rer. nat. Heinz Breer

1. berichtende Person: Prof. Dr. rer. nat. Volker Wulfmeyer

2. berichtende Person: Prof. Dr. Martin Claussen

Eingereicht am: 1st July 2014

Mündliche Prüfung am: 21st November 2014

Die vorliegende Arbeit wurde am 01.07.2014 von der Fakultät Naturwissenschaften der Universität Hohenheim als “Dissertation zur Erlangung des Doktorgrades der Naturwissenschaften” angenommen.

Abstract - English

Large-scale agroforestry in coastal arid and semi-arid regions could provide a geoengineering solution to anthropogenic climate change. Since agroforestry may impact on mesoscale climate in unknown ways, urgent research into potential impacts of large-plantations is needed to fully assess the viability and optimal placement for such schemes. Validated mesoscale simulations provide insights into feedbacks between land surface and atmosphere, particularly with respect to convective processes.

Simulations of irrigated *Simmondsia chinensis* (jojoba) plantations were carried out with the WRF-NOAH atmosphere-land surface model using prescribed land surface and plant parameters. A sub-surface irrigation algorithm was developed based on critical soil moisture stress levels and implemented into the model code. The simulation of desert and plantation land surfaces was validated with field data from two sites in the Negev Desert - an arid desert site and a 400 ha jojoba plantation. For desert and vegetated surfaces, the model output of diurnal meteorological quantities and energy fluxes generally match well with the respective observations. Diurnal 2m-temperatures over the desert and plantation are matched by the model to within $\pm 0.2^\circ\text{C}$ and $\pm 1.5^\circ\text{C}$, respectively. Wind speeds for both surfaces match to within 0.5 ms^{-1} and plantation latent heat is reproduced to within $\pm 20\text{ Wm}^{-2}$.

Subsequent to validation, larger plantations of $100\text{ km} \times 100\text{ km}$ were then simulated in two coastal arid regions, Israel and Oman over a period of one month and compared with control runs, without plantations. In Oman, convection and precipitation were triggered or enhanced by the plantation over multiple days whereas in Israel almost no impacts were observed. Two mechanisms were responsible for observed convection initiation: turbulent vertical transport of scalars due to increased surface heating and roughness as well as a low pressure-induced convergence at the canopy leeward side.

The main contributors to the surface heating effect were reduced albedo and the high water-use efficiency exhibited by specialist desert species. The combination of increased net surface radiation and high stomatal resistances significantly limited transpiration and led to a surplus in sensible heat flux compared with the surrounding soils ($> 100\text{ Wm}^{-2}$).

In Oman, convection initiation triggered by the plantation tended to occur on days when a high mid-tropospheric temperature lapse rate and significant surface air humidity were

present. Israel exhibits more stable lapse rates during summer and drier conditions aloft, both of which suppressed convection significantly, even with a similar land surface perturbation. The initiation of moist convection at the mesoscale is therefore strongly controlled by prevailing synoptic conditions.

A regional climatological analysis of temperature and humidity ECMWF reanalysis data and station precipitation data indicate that the south-west of North America has particularly suitable conditions for impacts. Coastal locations in Baja California and the Sonoran Desert exhibit a seasonal concurrence of monsoonal instability, high surface humidity and integrated column water vapor, but at the same time low precipitation. Therefore plantation impacts on convection there are likely and could be beneficial in terms of higher amounts of precipitation.

These findings indicate that mesoscale convective events can be triggered by large plantations within arid and semi-arid regions and that these effects may be controllable via judicious placement of such schemes. Thus arid agroforestry has the potential not only to increase precipitation and reverse desertification within arid and semi-arid regions, but also to mitigate climate change if implemented on very large scales.

Zusammenfassung

Großräumige Agrarforstwirtschaft in küstennahen ariden und semiariden Gebieten stellt eine Möglichkeit dar, mittels Geoengineering anthropogenem Klimawandel zu begegnen. Agrarforstwirtschaft wird das mesoskalige Klima jedoch in bisher unbekannter Weise beeinflussen. Daher ist es dringend notwendig, die möglichen Auswirkungen von großräumigen Plantagen in Bezug auf Durchführbarkeit und optimale Ausführung zu erforschen. Dazu geben validierte, mesoskalige Modellsimulationen Einblicke in die Wechselwirkungen zwischen Landoberfläche und Atmosphäre, insbesondere in Bezug auf konvektive Prozesse.

Bewässerte Jojobaplantagen wurden mit dem Atmosphären-Landoberflächenmodell WRF-NOAH simuliert. Dazu wurden die Landoberfläche und geeignete Pflanzenparameter fest vorgegeben. Ein neuer Algorithmus für die unterirdische Bewässerung wurde entwickelt und in den Modellcode implementiert. Die Simulation von Wüsten und Plantagenflächen wurde dann mittels Vergleich der Ergebnisse mit Feldmessungen von zwei Stationen in der Wüste Negev getestet. Eine Station befand sich an einem Wüsten-Standort und eine in einer 400 ha großen Jojobaplantage. Über den simulierten Wüsten und bewachsenen Flächen stimmen die Modellergebnisse der meteorologischen Größen und der Energie flüsse im Tagesverlauf im Allgemeinen gut mit den entsprechenden Beobachtungen überein. Der Tagesverlauf der 2m-Temperaturen in der Wüste und der Plantage bewegt sich im Bereich von $\pm 0,2^\circ\text{C}$ beziehungsweise $\pm 1,5^\circ\text{C}$ verglichen mit der Beobachtung. Die Windgeschwindigkeiten bewegen sich im Bereich von $\pm 0,5\text{ ms}^{-1}$ um die beobachteten Werte und der latente Wärmefluss zeigt Abweichungen von $\pm 20\text{ Wm}^{-2}$.

Im Anschluss an die Validierung wurden größere Plantagen von je $100\text{ km} \times 100\text{ km}$ in zwei repräsentativen ariden Küstengebieten (Israel und Oman) über einen Zeitraum von einem Monat simuliert und mit einem Kontrollexperiment ohne Plantagen verglichen. Im Oman löste die Plantage über mehrere Tage Feuchtekonzektion und Niederschläge aus oder verstärkte diese, während sie in Israel fast keinen Einfluss zeigte. Zwei Mechanismen waren im Wesentlichen verantwortlich für die Entstehung der Feuchtekonzektion im Oman: der turbulente, vertikale Austausch der meteorologischen Größen durch eine stärkere Erwärmung der Landoberfläche und erhöhte Rauigkeit sowie eine durch tieferen Luftdruck ausgelöste Konvergenz auf der Leeseite der Plantage.

Wesentlich zur Oberflächenerwärmung tragen die verringerte Albedo sowie die effiziente Wasserverwertung der auf Wüstengebiete spezialisierten Pflanzenarten bei. Die Kombination aus erhöhter Nettostrahlung am Boden und erhöhtem Stomatawiderstand begrenzt die Transpiration erheblich und führt zu einem Anstieg des sensiblen Wärmeflusses von ca. 100 Wm^{-2} im Vergleich zum umgebenden Boden.

Im Oman besteht die Tendenz zu einer Beeinflussung der Konvektion durch die Plantage im Fall von starken Temperaturgradienten in der mittleren Troposphäre und signifikant erhöhter Luftfeuchte an der Erdoberfläche. Israel hat im Sommer eine stabilere atmosphärische Schichtung und ist in höheren Lagen sehr viel trockener. Dies unterdrückt den Einfluss auf die Konvektion signifikant, selbst bei einer Änderung der Landnutzung. Die Auslösung von Feuchtekonvektion auf der Mesoskala wird also stark durch die großräumige Zirkulation bestimmt.

Eine auf Temperatur- und Feuchtefeldern der EZMW-Reanalysen sowie Niederschlagsdaten basierenden Analyse der regionalen Klimatologie zeigt, dass der Südwesten Nordamerikas besonders geeignete Bedingungen für eine Beeinflussung der Konvektion durch eine Plantage bietet. In der Monsunzeit zeichnen sich die Küstengebiete der Baja California und der Wüste Sonora durch das Zusammentreffen von instabiler Schichtung, hoher Luftfeuchte am Boden und hohem vertikal integrierten Wasserdampfgehalt aus, haben aber gleichzeitig kaum Niederschlag. Daher kann man einen Einfluss von Plantagen auf Konvektion und somit grössere Niederschlagsmengen erwarten.

Die Resultate zeigen zum einen, dass konvektive Niederschläge durch einen geeigneten Aufbau größerer Plantagen ausgelöst und zum anderen bezüglich ihrer Intensität beeinflusst werden können. Dies unterstreicht das große Potential der Agrarforstwirtschaft, nicht nur die Niederschlagsmenge zu erhöhen und die Wüstenbildung rückgängig zu machen, sondern auch dem Klimawandel abzuschwächen sofern die Plantagen groß genug sind.

Contents

Abstract - English	i
Abstract - Deutsch	iii
Contents	vi
1 Introduction	1
1.1 Background and motivation	1
1.2 Desert biomes and the climate of Israel and Oman	5
1.3 Arid agroforestry	9
1.4 Vegetation impacts on the arid land surface	12
1.5 Vegetation feedbacks to the arid climate	17
1.6 Precursors for convection initiation	22
1.7 Summary of key knowledge gaps	26
1.8 Objectives	27
2 Setting up and validating the model: simulating irrigated plantations	29
2.1 Introduction	29
2.2 Methodology - Model configuration, duration & spin-up	31
2.3 Methodology - Parameterization of irrigated Jojoba	33
2.4 Methodology - Validation	35
2.5 Results - Validation	38
2.6 Summary of results	42
3 Applying the model: impact study of arid plantations - Oman and Israel	45
3.1 Introduction	45
3.2 Methodology - Model domains, duration and spin-up	45
3.3 Results and discussion - Impacts, processes, precursors	47
3.4 Summary of results	72

4 Global Perspectives	77
4.1 Methodology - Analysis of regional and local climates	78
4.2 Results and discussion - Potential arid plantation zones	80
5 Conclusions and Outlook	91
Symbols and Abbreviations	101
List of Figures	108
List of Tables	109
Bibliography	110
6 Appendices	125
6.1 Israel summer of 2012 observations	125
6.2 Penman Monteith evapotranspiration models	130
6.3 Plots of mean max turbulent fluxes over plantation	131
6.4 Climate station data sources	132
6.5 Climate variance maps	133
6.6 Data and software used	139

Chapter 1

Introduction

1.1 Background and motivation

Emissions of atmospheric greenhouse gases are rising unabated, and a doubling of pre-industrial concentrations is expected by 2100, even if a substantial and timely reduction of fossil fuels is pursued (Wood et al., 2013). Unfortunately, this alarming trajectory now appears increasingly inevitable given the lack of a global political consensus on emission reductions. As such, urgent research into geoengineering methods is being ramped up to provide policy makers and other stakeholders with a basis upon which to assess the risks and potentials of such methods (e.g. see IPCC, 2012, 2013). Geoengineering, or “..the deliberate large-scale manipulation of the planetary environment to counteract anthropogenic climate change” (Shepherd, 2009), covers a range of methods, some of them controversial. Developing criteria for objective assessment of geoengineering methods remains a huge challenge, but various assessments have been carried out focusing on single methods (such as Hulme, 2012; Becker et al., 2013) as well as comparisons of various methods (e.g. Keith et al., 2005; Boyd, 2008; Izrael et al., 2009; Lenton and Vaughan, 2009, 2013). Some propose method rankings or recommendations, but there is a wide variability of opinion due to high uncertainty associated with the methods themselves, and also the difficulties involved in framing such assessments (Bellamy et al., 2012).

Two broad categories of geoengineering methods were proposed by the Royal Society (2009)¹: Solar Radiation Management (SRM) and Carbon Drawdown and Removal (CDR). SRM methods involve the reduction of solar energy absorption by the climate system, e.g. atmospheric sulfate aerosol injection or cloud brightening. CDR methods on the other hand introduce net carbon sinks on scales large enough to alter the climate (see IPCC, 2012; Wood et al., 2013). Examples are afforestation and carbon capture and sequestration (CCS) (see Betts, 2007; IPCC, 2012).

¹ Geoengineering the climate: science, governance and uncertainty. Report 10/09, 2009, 82 pp. Technical report.

Large-scale afforestation (or LSA) falls under the CDR umbrella and could incorporate a whole range of semi-natural or managed vegetated ecosystems and within various biomes (e.g. see Montagnini and Nair, 2004). LSA has major potential for carbon sequestration in vegetation and soils; impacts on environmental services (Lal, 2005; Lorenz and Lal, 2009); international or national carbon trading agreements (e.g. see Torres et al., 2010); and deforestation reduction initiatives such as REDD+². One study estimates that in the last few decades, the planting of 250 million hectares of forest globally, has provided a sink of around 0.3 Pg C year⁻¹, representing around 3% of current emissions (Lenton and Vaughan, 2013). If such a trend could be accelerated, LSA could potentially form a significant part of a “wedge” approach to anthropogenic climate change mitigation.

There are still major uncertainties though. Firstly, for LSA schemes to become net carbon sinks, net conversions or plantings must be permanent and losses to decay would need to be replaced if those schemes are not to become sources of CO₂. Secondly, it is not certain how much of the negative forcing due to CO₂ reduction, will be offset by the increase in shortwave absorption (Betts, 2000; Bird et al., 2008) although Bird et al. (2008) suggest that only a 30% benefit reduction is likely. This assumption may be complicated by regional aspects of LSA implementation. For instance, in a lower latitude afforestation site (Yatir Forest in Israel), a shift in seasonal peak photosynthesis and a long wave suppression effect was observed - yielding a net positive forcing (Rotenberg and Yakir, 2010). Thirdly, there could be major regional and global climate impacts of LSA (beyond CO₂ reduction). The IPCC (2012) cite areas of concern as a) effects on global or regional climate, and also b) effects that span national boundaries. On very large scales, land use/climate feedbacks have been demonstrated, e.g. by Avissar and Werth (2005), who linked Amazonian deforestation with higher latitude rainfall patterns using GCM³ simulations. Remote impacts such as this are sometimes called teleconnections (Potter et al., 2004; Avissar and Werth, 2005) and include phenomena such as El Niño which triggers non-linear feedbacks between ocean, atmosphere and land. At smaller scales, land use/climate modifications can occur at regional and mesoscales and have been observed/simulated in a variety of studies (e.g. see Pielke et al., 2007). The exact mechanisms involved are not necessarily fully understood yet though. Potentially, such impacts could be so significant, according to Stohlgren et al. (1998) that they might effectively obscure impacts from increased global mean temperatures. On the other side of the coin, a modification of e.g. rainfall frequency or spatial distribution is likely to modify the distribution and abundance of vegetation, producing complex feedbacks (Ramankutty et al., 2006; Mahmood et al., 2013). Finally, LSA has the potential to cause land use conflicts and reduced food security. A UNFCCC⁴

² UN-REDD or United Nations collaborative initiative on Reducing Emissions from Deforestation and forest Degradation (REDD) in developing countries

³ General Circulation Model

⁴ United Nations Framework Convention on Climate Change

criterion for CDM⁵ schemes, is that none should compete with food production, due to scarcity of arable land. According to Costanza et al. (1997), only 1.4 billion ha of land is still arable from the total 15 billion ha of global land surface. Becker et al. (2013) estimate through current trends and including effects of land degradation, that $\sim 1100 \text{ m}^2$ of land will be available to feed each of the 9 billion inhabitants projected for 2050.

One way of avoiding land use competition would be to cultivate biomass plantations only on marginal lands, within arid or semi-arid coastal regions, e.g. Namibia, Oman, and California (Becker et al., 2013). These areas currently cover ~ 1 billion ha globally. If only marginal lands were used, this could reduce competition with other land uses to some extent. Arid plantations could also halt recent desertification trends which have been particularly severe in drier regions (Mueller et al., 2014). This type of LSA scheme involving biomass plantations, consisting of small trees or shrubs will be hereafter known as arid agroforestry. Large-scale implementation of arid agroforestry, will have biogeophysical, societal, technological and economic implications - spheres which are inevitably interrelated. Societal and economic benefits could accrue through energy production and agricultural development (Beringer et al., 2011; Becker et al., 2013). Modified temperatures and rainfall patterns, would affect the quality of life and livelihoods of local inhabitants - both social and economic issues. In fact, significant biogeophysical impacts such as changes in rainfall patterns, soil sealing or salinization could dictate whether schemes are technologically or agriculturally viable over a given time period. Gaining a deeper understanding of potential mesoscale climate feedbacks is a vital piece of the jigsaw puzzle, and such knowledge must be included within holistic assessments of agroforestry. Moreover, furthering our knowledge of potential climate interactions could benefit us beyond the provision of simple risk assessments. If climate impacts associated with specific agroforestry schemes can be predicted, there may be a potential to steer schemes towards positive climate outcomes and to minimize negative impacts. For instance, an ‘ideal’ case scenario would arise if we could predict locations where beneficial impacts, such as moist convection initiation are more likely (such impacts are posited by Wulfmeyer et al., 2014). At the present time, biomass plantations which are likely to have ‘geoengineering’ scale impacts, i.e. dimensions of many thousands, or tens of thousands of square kilometers, do not currently exist. Thus, the possibility to observe impacts at geoengineering scales is not yet possible.

So how can we investigate the likely impacts? Mesoscale impacts from very large agroforestry plantations, could be simulated within atmospheric/land surface models such as the WRF-NOAH model (Skamarock et al., 2005; Chen and Dudhia, 2001), using a down-scaling method. Such simulations can give us vital insights into the impacts/processes involved, and allow us to test the effect of altering variables such as region and plant/soil properties. If impacts are to be simulated correctly though, it is important that the model

⁵ Clean Development Mechanism

can represent both land surface and atmospheric processes in a realistic, and therefore useful way.

Firstly, the use of fine ‘convection permitting’ grid spacings ($\sim \leq 3\text{--}4$ km) within models renders a detailed resolution of landscape features such as orography, soil texture and land use type. Modelling at such scales can reduce biases and systematic errors in soil/cloud/precipitation feedbacks, often seen in coarser scale models where convection is usually parameterized (Rotach et al., 2009a, 2010b; Wulfmeyer et al., 2008, 2011; Weusthoff et al., 2010; Bauer et al., 2011).

Secondly, and of particular importance is how plant properties, irrigation, and energy balances are modelled within the land surface model. Simulation of evapotranspiration, for instance in arid regions has been shown to be very sensitive to plant parameters like stomatal resistance (R_{st}) and leaf area index [LAI] (Unland et al., 1996; Groner, 2013). One of the aims of this thesis is to simulate an agroforestry plantation as realistically as possible, with representative plant/soil properties, and irrigation. Simulating large fictitious plantations is one thing, but how does one test the realism of such a simulation? A typical approach to model testing/optimization is by validation/calibration using relevant observation data. However, in this case the problem is a lack of geoengineering scale plantations from which to obtain representative data for such an approach.

This thesis attempts to ‘bridge’ this gap, by first simulating a plantation at a more limited scale (10×10 km) and validating the model with data from an existing moderate-sized plantation (Chapter 2). In this way, simulated land surface quantities such as energy fluxes can be compared with those over an operational plantation, and if necessary the model parameters can be adjusted. For the main impact study in Chapter 3, the plantations are scaled up to a geoengineering scale (100×100 km) and inserted into two different arid locations in the Near/Middle East - Israel and Oman. By pre-validating the model simulation, we can be more confident that important processes are well represented at large scales. In Chapter 4, links between impacts and prevailing climate are investigated, and an assessment of potential regions is made.

The following introductory sections provide necessary context for the main experiments, specific objectives and work flow, and are ordered as follows: In Section 1.2, a general overview of desert biomes is given, and a description of the study area climates. In 1.3, the arid agroforestry concept is presented within the context of anthropogenic climate change and desertification. In 1.4, the primary land surface modifications from vegetation are outlined, before a discussion of how these drivers feedback to the mesoscale climate in 1.5. In 1.6 some important aspects of convection initiation, and necessary precursors are discussed, keeping the focus on relevance to arid regions, and to the scenario used here. Key knowledge gaps and the main research questions are given in Sections 1.7 and 1.7.3. Finally, the specific objectives and work flow are set out in Section 1.8.

1.2 Desert biomes and the climate of Israel and Oman

Arid agroforestry as a geoengineering solution implies very large scales of implementation because by definition, a global impact is required in terms of carbon sequestration. As such, any study on arid agroforestry should be set within the context of global desert biomes, and in particular, the main processes governing their formation and evolution. Much of the information for this overview is drawn from the comprehensive book by Warner (2006)⁶.

1.2.1 Deserts biomes and primary drivers of aridity

Arid and hyper-arid regions cover around 17% of the world's land area (UN, 2014) and are often conceived as barren wastelands, homogenous over vast distances. In fact, they can be extremely varied, with a given desert containing a myriad of complex microclimates, vegetation types and land surfaces. They also vary considerably in climate and governing processes, from one desert to the next. There are generally considered to be three types of desert; hot, cold, and foggy-coastal deserts (see Figure 1.1, left). Within these broad categories there can also be large variations in precipitation amounts and patterns, with some areas receiving their rainfall either in winter, in summer or in transitional periods (see Figure 1.1, right). Other regions such as the eastern Sahara, receive almost no rainfall at all (Warner, 2006).

No single classification system has yet been agreed upon, to delineate deserts from other biomes, or for defining degrees of aridity within desert regions. Instead there is a range of systems. As a general rule, it is thought to be a mistake to classify aridity, based purely on annual rainfall, mainly because of the considerable variation in precipitation patterns, temperature and specific climate feedbacks. A general indicator, or characteristic of arid regions is that the surface water loss due to evapotranspiration (ET) exceeds the gains from precipitation (Warner, 2006). There are systems which are based on annual statistics though. One is the Budyko (1986) index which uses the above rainfall/ET relation and is calculated as the ratio of the rainfall that can be evaporated annually by the total annual net radiation, divided by the depth of the annual precipitation [mm yr^{-1}]. Another, the UN (1977) system uses the ratio between precipitation to potential evaporation (P:PET) and characterizes areas as: hyperarid (P:PET < 3 : 100), arid (P:PET between 3:100 and 20:100) and semi-arid (P:PET between 20:100 and 50:100). Other widely used systems such as Meigs (1953) and Thornthwaite (1948) also account for seasonal variability of rainfall, and may be more useful in some applications. What is clear is that biome maps drawn based on these systems may appear markedly different from one another, and therefore an ideal choice of classification system may depend on the application. For

⁶ Desert Meteorology - Thomas Warner

instance, the Köppen (1931) system, which is based on Thornthwaite (1948), splits the land surface into zones based on prevailing vegetation type and abundance. This is a most interesting system, especially if one is concerned with a) regional vegetation climate feedbacks in general, and b) the suitability of a region for cultivating certain types of vegetation, e.g. arid agroforestry.

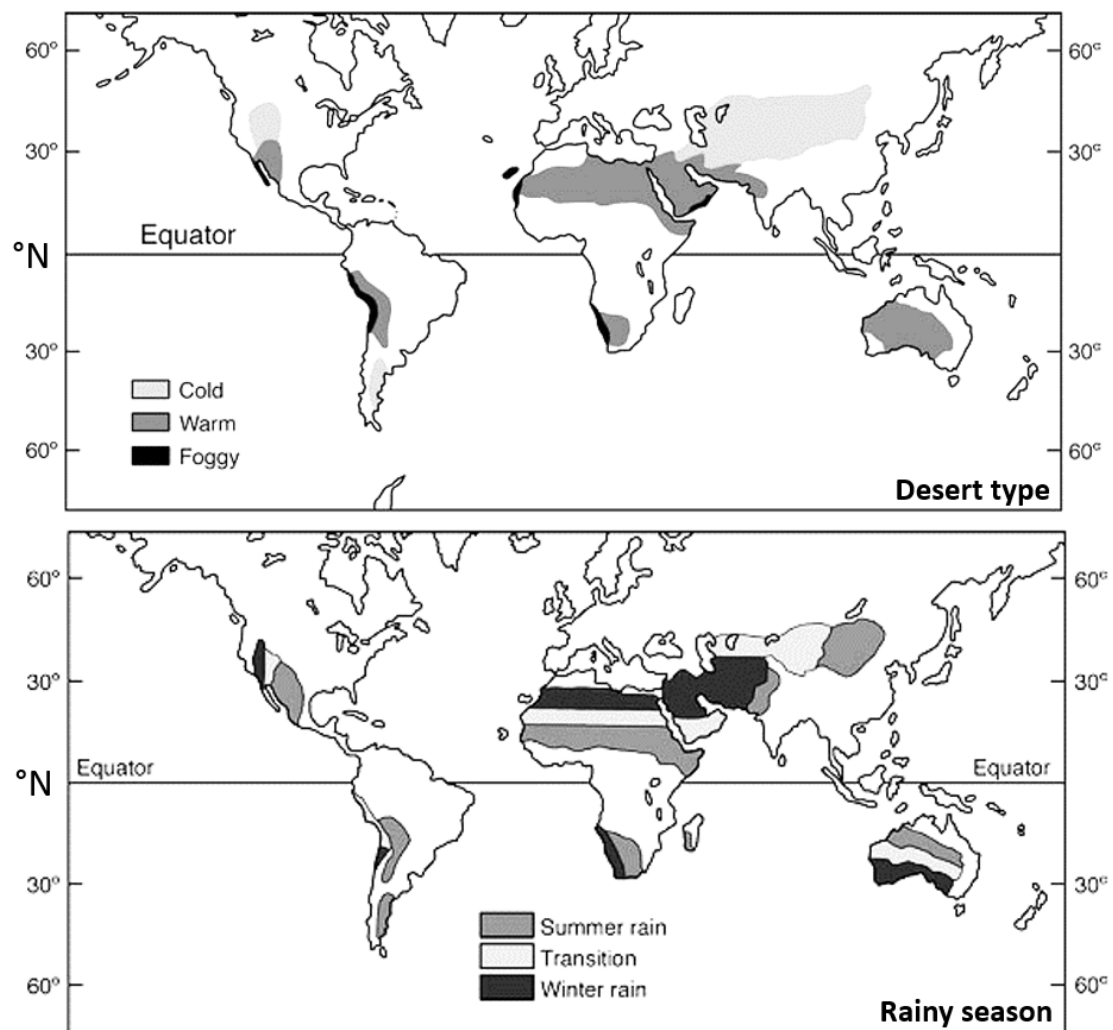


Figure 1.1: Global desert biomes and rainfall - Classification of desert biome determined by the main drivers of aridity and environment (left panel). The right panel indicates the time of year when rainfall occurs (if any). Israel, being influenced by the Mediterranean receives almost all of its rainfall during winter whereas Oman rainfall tends to come during transitional periods. Adapted from Warner (2006).

For deserts globally, the main driver of aridity is atmospheric subsidence which is caused by the Hadley circulation and occurs between the intertropical convergence zone (ITCZ) and the ascending air at mid-latitudes ($\sim 10^\circ$ to $30\text{-}40^\circ$ N and S). This subsidence suppresses precipitation, and accounts largely for the existence of deserts such as the Sahara, Arabian, Kalahari, Australian, Monte, Patagonian, and Thar, within these zonal bands.

These are classified generally as **subtropical** deserts. Hadley subsidence can be thought of as a first-order driver, but there are other important mechanisms too. In the Sahara for instance, high desert radiative losses (in comparison with the less arid surroundings) lead to subsidence-induced heating and drying, which then intensifies the Hadley subsidence already present (Charney, 1975). Other factors such as monsoonal impacts, can also lead to region-specific deviations from this generalization. Aridity can also be caused by remoteness from maritime moisture sources (**interior continental** deserts, e.g. Gobi), proximity to orography (**rain-shadow** deserts, e.g. Tibetan), and proximity to cold coastal currents (**cool coastal** deserts, e.g. Namib, Atacama).

Cool, coastal areas such as the Namib, are affected by a coastal upwelling mechanism. This is induced by a strong “geostrophic adjustment to the sea-land thermal gradient, associated with Coriolis deflection” (Parish, 2000), which deflects onshore winds towards a direction parallel to the coast. These parallel winds have two effects. One is to deflect surface water to the right (facing equatorward) via the Ekman spiral effect, which then draws cooler waters to the surface. The resulting cool air mass creates a strong capping inversion at the coast. The other effect is a land friction-induced deflection of coastal parallel winds towards the land based pressure-low, leading to divergence and subsidence over the coastline. These effects combine to produce a very stable PBL, whilst the resulting cool moist surface air mass can lead to dense mixing fogs (Warner, 2006), which are often the only source of moisture for vegetation, e.g. in the Atacama and the Namib.

The two desert study areas used for this thesis (Negev, Israel and the Ramlat al-Wihiba coast, Oman) are essentially extensions of the Sahara and Arabian deserts, respectively. They are good examples of subtropical and coastal deserts but each with some defining characteristics. Their climates are described in Section 1.2.2.

1.2.2 Climate description - Negev, Israel and Ramlat al-Wihiba, Oman

In central Israel, long hot summers, clear skies and high radiation are the most common conditions. Synoptically, a pressure trough to the north generally runs from Turkey down to the Persian Gulf, drawing north-north-westerly winds steadily in from the Mediterranean for most of the year. Until around October, the summer climate is dominated by Hadley subsidence which warms and dries the middle to lower troposphere, and strong inversions which inhibit moist convection (Perlin and Alpert, 2001). This subsidence tends to counteract the cooling advection from the Mediterranean (Saaroni et al., 2004). During the autumn, these inversions tend to weaken, after which time the Mediterranean and the passage of winter cyclones start to exert more influence to the north. Precipitation is usually convective when it occurs, either embedded in the passage of fronts or induced by local circulations (Perlin and Alpert, 2001). Israel can in general be split into two climate zones: a varied semi-arid climate in the northern half, which is to the north of our study

area, and an arid climate in the southern half - the Negev desert. The Negev forms an extension of the Sahara to the west (see Figure 1.1), and can be classified as a ‘warm subtropical’ desert with the main aridity mechanism being subsidence. The Negev region has a Budyko index of 10 which is not particularly arid, but reflects the influence of the Mediterranean and the arrival of rains during the winter. In the Köppen system, central Israel, or the northern fringe of the Negev, is classified as a ‘hot semi-arid’ climate, with hot summers and a short defined wet season, but not enough to be classified as ‘tropical savanna’. The main part of the Negev is a ‘hot desert’ climate, with insufficient rain to support any vegetation, apart from scrub. In general local maximum temperatures tend to peak in July at around 33°C , with almost no rainfall over the summer months (see Figure 1.2 for twenty-year climatology of Beer’sheva, northern Negev).

Oman has three quite distinct sub-climates. The south is a moist tropical region, strongly influenced by the monsoon in summer. The north coast tends towards hot summers with high rainfall. The study area lies on the Ramlat al-Wihiba central desert coast where maximum temperatures can reach up to 50°C inland but only around $30\text{-}40^{\circ}\text{C}$ at the coast. Little rainfall occurs inland, and only up to 10 to 20 mm month^{-1} falls on the coastline during the summertime (see Figure 1.2 for climate data on Masirah Island, Ramlat al-Wihiba coast). The inland area has a Budyko index of up to 50, which is hyper-arid and reflects the low rainfall all year round, and contrasting with the more Mediterranean Israel climate. In the Köppen (1931) system, the Ramlat al-Wihiba region is classified as a ‘hot desert’ climate, supporting little vegetation. Although the area is subject to Hadley subsidence (especially inland), the coastal zone here can be classed as a ‘cool coastal, or foggy desert’ similar to the Namib (Figure 1.1). The strong coast-parallel winds here (as previously described) form a low-level coastal jet (LLCJ) in Oman, which should be differentiated somewhat from the monsoonal winds which flow in parallel, but further out from the coast (Ranjha, 2013). LLCJs (and cool, coastal deserts generally) usually lie on continental west coasts, which are dominated by subsidence (Namib, Atacama, California, Western Sahara). Oman, being on the east coast is therefore unique in that respect. It also has the highest frequency of jets and the highest maximum wind speeds (Ranjha et al., 2013). LLCJs are characterized by a strong peak in the wind-speed profile within the lowest few kilometres; have a shallow vertical extent (up to a few hundred metres), but can extend horizontally for many tens or hundreds of kilometers. It has also been demonstrated that coastal irregularities such as capes or coves can produce unusual effects such as sharp accelerations and decelerations (e.g. Söderberg and Tjernström, 2001). For instance, where the coastline turns away from the semi-geostrophic coastal flow, the winds tend to thin, fan out and accelerate (Ranjha, 2013). Therefore we might expect phenomena such as sharp speed and directional shears close to the coastline (these effects become relevant in Chapter 3). Ranjha et al. (2013) studied the dependence of correct LLCJ representation, on the model grid spacing and concluded that LLCJ resolution was improved with finer

horizontal grid increments. Importantly they also found that a spacing of 9 km or less, was adequate enough to capture most features, which is highly relevant for our simulations within this region.

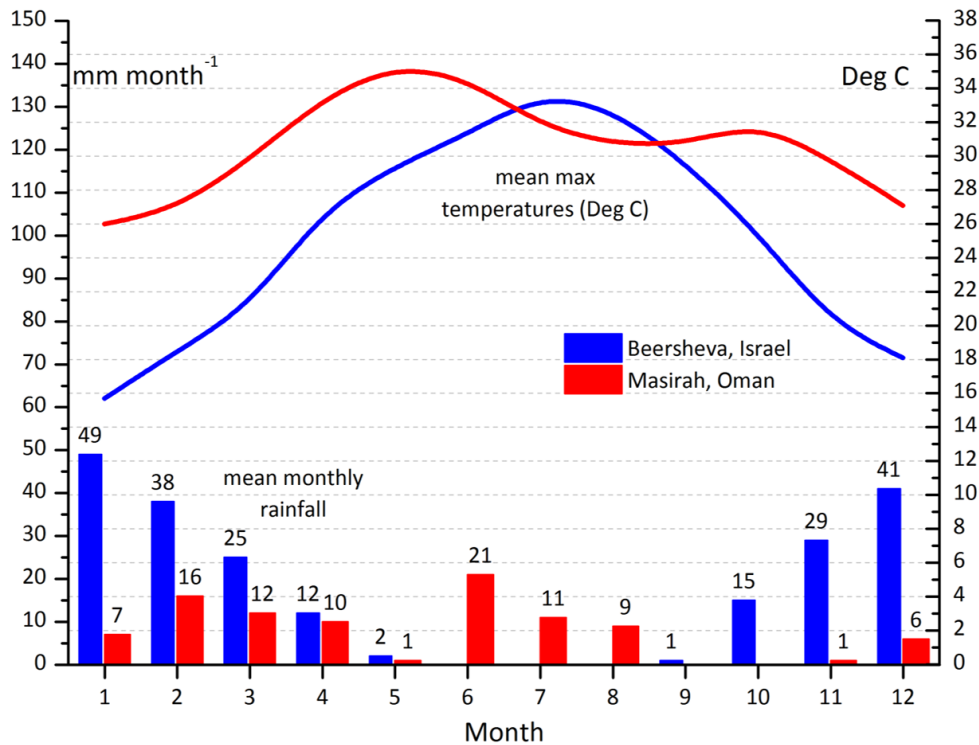


Figure 1.2: Climatology of Beer'sheva, Israel and Masirah Island, Oman which are weather stations in the vicinity of each plantation. The bars indicate mean rainfall (mm month^{-1}) and the curves are mean monthly maximum T_{2m} ($^{\circ}\text{C}$). Note that Masirah is an island and the air is likely to be cooler and more moist than further inland. Source - NOAA monthly summaries [1985-2005 - Beer'sheva] - [1992-2012 - Masirah].

1.3 Arid agroforestry

Mankind's interest in the cultivation of arid or semi-arid lands has existed as far back as cultivation itself. Although societies have rarely settled deep within very arid areas, many early civilizations developed around the fringes of deserts. In more recent times, populations in arid areas have risen, although not always through individual choice. In less developed regions, some of the largest rates of modern population growth are situated close to or within arid zones, e.g. in Western Sahara, Mali and Jordan (UN, 2012). In more developed countries, people have been attracted by warmer climates and more abundant land (Warner, 2006). Furthermore, marginal and semi-arid areas are often afflicted by the encroachment of aridity thus increasing populations within arid regions. Habitation in such areas has led to the development of agricultural techniques such as dryland farming, nomadic existences and other means of adapting to marginal soils and

drought (for instance, see Hargreaves, 1957; Rowland, 1993, for historic descriptions in the USA and Africa).

Living in proximity to arid or semi-arid regions is inevitably overshadowed by desertification and anthropogenic climate change. Desertification, using its most modern definition is described by the UNCCD (1994)⁷ as “land degradation in arid, semi-arid and dry subhumid areas, resulting from various factors, including climatic variations and human activities”. In earlier times, the meaning of desertification carried an emphasis more on the human drivers of desertification, such as land mis-management. In more recent times however, the definition has expanded, along with our understanding to include climatic effects and feedbacks relating to land use and climate change (D’Odorico et al., 2013). Desertification is felt not only on the fringes of very arid regions, such as the Sahel, but also in semi-arid Mediterranean climates, such as the Iberian peninsula (Puigdefábregas and Mendizabal, 1998; Kéfi et al., 2007) or California, USA (Lam et al., 2010). In fact it is estimated that globally, 1.9 billion ha of former cropland is now fully or partially degraded (Becker et al., 2013).

Restoration of vegetation remains an effective way to prevent or reduce desertification and prevent sand encroachment, but its implementation is often difficult due to lack of rainfall, poor substrates, and high cost (Gao et al., 2002). Nevertheless, new methods and paradigms relating to arid afforestation are being researched to tackle these issues. An example is in Israel, where Portnov and Safriel (2004) propose that one way of increasing the value of dryland cultivation would be to link such land use change with the urbanization of some regions of the Negev. Developing new economic and agricultural means of ‘greening the desert’ in this way could simultaneously help to combat desertification, sequester carbon and potentially modify the local/mesoscale climate.

The original idea for this thesis came about through a bioenergy ‘carbon farming’ concept proposed in a multidisciplinary study by Becker et al. (2013) and this concept was used further in a model impact study by Wulfmeyer et al. (2014). Carbon farming was based around a large *Jatropha curcas*⁸ plantation (100×100 km) with an integrated biomass power plant and desalination system. The idea is that from the total biomass grown, a part of it, in the form of, nuts, leaves, and trimmings, is burnt in the power plant, which then drives the desalination process for irrigation. A fundamental aspect of their proposal is its location by the coast, to take advantage of a) local seawater for desalination and b) moist advected marine air. The Becker et al. (2013) study covers economic costs, market issues, technological feasibility and likely feedbacks to the local/mesoscale climate.

In addition to *Jatropha curcas*, other species could potentially be cultivated in a similar way. Many species have evolved to survive in harsh, arid climates, with a myriad of built-

⁷ United Nations Convention to Combat Desertification

⁸ In addition to Becker et al. (2013), further information on *Jatropha* can be found in Openshaw (2000)

in survival strategies. Phreatophytes for instance, such as mesquite develop long tap roots to reach deep water tables. Xerophytes, such as euphorbias have developed characteristics which conserve water or reduce heat loading. Examples of such characteristics are leaves which have a waxy coat, maintain their edges to the sun, or have a high albedo. Halophytes, such as saltbush are resistant to saline soils (see Ogburn and Edwards, 2010, for an overview of plant types). *Jatropha* (halophyte) and *Jojoba* or *Simmondsia chinensis* (xerophyte) in particular, are valuable and extremely hardy crops, able to withstand both heat and drought, be irrigated with waste- or brackish water (Benzioni, 1995; Abou Kheira and Atta, 2009; Rajaona et al., 2012; Branch et al., 2014). These traits generally make them more viable than food crops in marginal areas.

In terms of sequestration, *Jatropha curcas* and similar sized trees are estimated to produce an aboveground biomass of 5 - 25 tonnes ha⁻¹ of dry mass per year (SEPASAL, 2010)⁹, equivalent to 2.4 - 12 tonnes C yr⁻¹ (Steen and Reed, 2004). Becker et al. (2013) calculated that *Jatropha* could sequester 17 - 25 tonnes of CO₂ ha⁻¹ yr⁻¹, over a 20 year period. A plantation scale of 100 × 100 km (1 million ha) would therefore equate to 17 - 25 million tonnes CO₂ ha⁻¹ yr⁻¹. As a point of reference, the total weighted greenhouse gas emissions of Estonia in 2010 (in equivalent tonnes of CO₂) was 20.5 million tonnes (Eurostat, 2014)¹⁰. This quantity of sequestration represents a measurable and therefore geoengineering scale drawdown. Becker et al. (2013) calculate sequestration costs of between 42 - 63 Euros per tonne of CO₂, which is competitive with methods like carbon capture and sequestration.

From a technological point of view, the realization of such schemes is becoming more feasible now. New water management pathways are being developed for arid/semi-arid regions, such as modern desalination methods (Fritzmman et al., 2007; Khawaji et al., 2008) and increased use of urban wastewater (Oron et al., 1999; Hamilton et al., 2007; Becker et al., 2013). In parallel, new agricultural methods are being developed to increase water use efficiency (WUE) of plants¹¹, such as deficit irrigation methods like partial root zone drying (PRD) (Spreer et al., 2007; Xie et al., 2012). Another example is the experimental use of chemical anti-transpirant films for arid/semi-arid species, with the intention of artificially closing stomata and limiting water use, whilst avoiding harm to the plants (Ludwig et al., 2010; Ansari et al., 2012; Shinohara and Leskovar, 2014).

The IPCC (2007) have seen the potential of bioenergy plantations to combine sequestration and fuel switching. Their new RCP¹² scenarios used in AR5¹³ include a “Bio-energy with Carbon Sequestration” scenario (BECS) in RCP2.6, as well as an “LSA” scenario in

⁹ Survey of Economic Plants for Arid and Semi-Arid Lands

¹⁰ Eurostat - Greenhouse gas emissions by country, 2000-2010

¹¹ See Sinclair et al. (1984) for definitions of WUE

¹² Representative Concentration Pathway, based on 2100 radiative forcing compared with pre-industrial levels [W m⁻²]

¹³ Fifth Assessment Report of the Intergovernmental Panel on Climate Change (2013)

RCP4.5 (Bellamy et al., 2012). Although bioenergy scenarios are possible, agroforestry schemes could conceivably contain any single, or combination of hardy species of significant biomass (Montagnini and Nair, 2004). It may well become apparent that the large-scale cultivation of current biofuels is non-viable, due to market distortion and land use competition (see de Gorter et al., 2013; Palmer, 2014). In that case, alternative systems could offer diverse alternatives, to monocultures and biofuels. Jojoba for instance, is a valuable oil crop which can be used for bio-diesel (Huzayyin et al., 2004), but is in fact more valuable when used for health and cosmetics (Benzioni, 1995). The spatial implementation of arid agroforestry schemes could also take many forms. Plantations could be concentrated all in one region, or spread out over many countries. Plantations could be large and contiguous, or be scattered smaller patches. Ultimately, it is likely that many geopolitical, socioeconomic, agricultural and climatic factors will determine the choice of large-scale solutions. For instance, implementation may depend on global emissions agreements such as CDM¹⁴, or be dependent on agricultural suitability as is the case in the IPCC BECS scenario (Vuuren et al., 2011). The purpose of this study aims to provide a ‘climate impact’ contribution to the science and as such, political, economic or agricultural criteria such as these are not specifically addressed here.

1.4 Vegetation impacts on the arid land surface

There are many ways in which vegetation modifies the arid land surface. Some examples of vegetation effects are modifications to: albedo, rainfall interception, soil permeability, transpiration, soil crusting/binding, mean and turbulent winds, and shading of substrate (Warner, 2006). Unfortunately, a full discussion of all aspects of vegetation impacts on the arid land surface is not possible here, and Bonan (2008) and Warner (2006) are recommended for further reading. Instead, only those drivers most important to CBL modification are addressed, which are changes in radiative balances, surface roughness and water availability. These phenomena determine the fluxes of momentum, heat, water vapor, and carbon dioxide (Pielke et al., 2011). This section, will give a brief description of the convective PBL, or CBL and how vegetated surfaces modify its main land surface drivers.

1.4.1 The arid convective boundary layer

Feedbacks between the land surface and atmosphere occur within the PBL, the lower part of the atmosphere affected by surface friction. In comparison to the night time stable PBL where shear or friction is usually the main driver of turbulence, the daytime CBL is dominated by buoyancy induced turbulence. This is especially true in arid CBLs where surface

¹⁴ UNFCCC Kyoto Clean Development Mechanism (CDM) allows a country with an emission-reduction or emission-limitation commitment under the Kyoto Protocol (Annex B Party) to implement an emission-reduction project in developing countries

heating is intense, whilst roughness tends to be low. The ratio of buoyant/mechanical contributions to total TKE can be expressed approximately by the Richardson number R_f [flux form] (Markowski and Richardson, 2010):

$$R_f = \frac{\left(\frac{g}{\theta} \overline{w'\theta'}\right)}{\left(\overline{u'w'} \frac{d\bar{u}}{dz} + \overline{v'w'} \frac{d\bar{v}}{dz}\right)} \quad (1.1)$$

where the nominator and denominator on the righthand side [RHS] represent turbulence contributions through buoyancy and wind shear, respectively. Here, the overbars represent mean values, and primes are perturbation values. g is gravitational acceleration [m s^{-2}], θ is potential temperature [K], w is vertical velocity [m s^{-1}], u and v are horizontal wind components [m s^{-1}]. $\overline{w'\theta'}$ is the vertical turbulent exchange of heat and $\overline{u'w'} \frac{d\bar{u}}{dz}$ and $\overline{v'w'} \frac{d\bar{v}}{dz}$ are the vertical momentum flux production terms.

The lowest 10% or so is the surface, or constant flux layer, characterised by strong vertical wind shear and temperature gradients. Above this lies the mixed layer. Strong daytime surface heating, leads to unstable stratification in the surface layer, and buoyant acceleration of parcels into the mixed layer. This leads to turbulent mixing, CBL growth, and weaker gradients of moisture and temperature throughout the mixed layer. A more neutral stratification weakens accelerations upon perturbation within this layer. At the top of the CBL lies the interfacial layer above which, negative humidity and positive temperature gradients normally occur, at the interface to the free troposphere. These gradients are often strengthened in arid regions due to the mean Hadley subsidence of warm, dry tropospheric air. Common heights for CBLs are 1-2 km but they can easily reach 4 km or more, particularly over deserts where dry surfaces, high radiation and strong surface heating lead to significant buoyancy-induced turbulence (Warner, 2006).

How the CBL evolves depends on a number of feedbacks occurring simultaneously between the land surface, mixed layer and entrainment zone (van Heerwaarden et al., 2009), all of which are influenced by the presence or non-presence of vegetation.

1.4.2 Surface radiative and energy balance modification

Chief among the drivers of CBL evolution, is partitioning of available energy into turbulent sensible (Q_H) and latent heat (Q_E) fluxes. However, the available energy for these two fluxes depends on the surface radiative balance such that (neglecting plant energy storage which is negligible on diurnal scales):

$$Q_H + Q_E + Q_G = SW \downarrow (1 - \alpha) + LW \downarrow - LW \uparrow \quad (1.2)$$

where Q_G is the ground heat flux, $SW \downarrow$ is the incident solar radiation, α is the surface albedo fraction (calculated as $SW \downarrow / SW \uparrow$). $LW \downarrow$ and $LW \uparrow$, are down- and upwelling

longwave radiation components and (all radiative and energy fluxes are in W m^{-2}). Positive energy fluxes represent fluxes away from the land surface and positive radiative fluxes are towards the surface. In arid regions, $\text{SW}\downarrow$ is generally high due to cloud free skies and low zenith angles at subtropical latitudes. However, high radiation can be offset somewhat by high α in deserts, where typical values are 0.25 to 0.40 for dry bare sand, but can reach up to 0.7 for dry, gypsum sand (Warner, 2006). Furthermore, atmospheric absorption of $\text{LW}\uparrow$, and re-radiance of $\text{LW}\downarrow$ is low due to a drier lower atmosphere which is why desert surfaces tend to cool rapidly at night.

As the CBL evolves over the day, Q_E generally moistens the CBL, while Q_H provides the energy for CBL growth. The land and atmosphere are tightly coupled however. Increased partitioning of energy into Q_H also increases entrainment of warmer, drier tropospheric air into the CBL, which in turn increases the atmospheric demand for water and evaporation. In the absence of larger scale advection, this feedback process tends to approach an equilibrium, where the evaporative fraction $\frac{Q_E}{Q_E + Q_H}$, moves towards a steady state (van Heerwaarden et al., 2009).

Plants modify radiative balances in complex ways, and the exact partitioning of radiant energy into reflected, scattered, transmitted or absorbed components depends on canopy, plant and leaf characteristics, such as structure, coverage and condition (McPherson, 2007). One canopy impact is the absorption of upwelling long wave radiation from the substrate. Another effect results from the canopy albedo, which is usually lower than bare desert soils. Figure 1.3 (left) shows measured summer diurnal albedos and standard deviations (σ) over Jojoba and Jatropha, compared with bare Loess sandy loam soil in the Negev, Israel. The vegetation has a significantly lower albedo than the desert soils (up to 0.18 difference at noon for Jojoba) which results in more available energy for turbulent fluxes. Furthermore, Jojoba has a lower albedo than Jatropha (by up to 0.05), which highlights that species choice may significantly affect climate modification.

There are vegetation impacts directly on the energy balance. For one thing, transpiration is controlled by the aperture of the plant stomata. In general when plants are stressed through drought, extreme temperatures or salinity, the stomata close and partitioning into Q_H increases. In fact, the Bowen ratio (Q_H/Q_E) has even been used as a metric for surface stress and vegetation condition (McPherson, 2007). Species characteristics may invalidate this assumption though, and desert species, such as Jojoba and Jatropha can more frequently close their stomata, e.g. during the hottest part of the day, without experiencing undue stress. This is due to their high water use efficiency, their ability to re-distribute water at night and other survival properties (Benzioni and Dunstone, 1988; Abou Kheira and Atta, 2009; Silva et al., 2010). Another impact on the energy balance is that solar energy absorbed by leaves and stems is converted more efficiently into sensible heat than from substrate, because leaves and stems have less storage mass

for heat. (Warner, 2006). Together with biophysical controls on evapotranspiration (ET), this could have profound impacts on how energy balances change, diurnally. Figure 1.3 (right) shows measured air temperatures at 2m (T_{2m}) over Jojoba, Jatropha and desert land surfaces [$^{\circ}\text{C}$].¹⁵ Daytime temperatures are 3 $^{\circ}\text{C}$ higher over Jojoba than the desert, and 5 $^{\circ}\text{C}$ higher over Jatropha. This plantation heating could be due to surplus R_N over the canopies, or it could be due to more efficient transfer of Q_H from leaves. The desert soils also appear to have a damping effect on peak T_{2m} . This effect is perhaps not surprising, given the greater daytime Q_G observed in the desert soils, compared to Q_G in soils under the canopies (Branch et al., 2014). Accordingly, the greater night time T_{2m} in the desert is likely to be partially due to the slow release of stored heat from the desert soils. Regarding the counterintuitive albedo/ T_{2m} reversal between Jojoba and Jatropha, an explanation may be a difference in diurnal stomatal behaviour of Jojoba/Jatropha, but this is not yet completely clear.

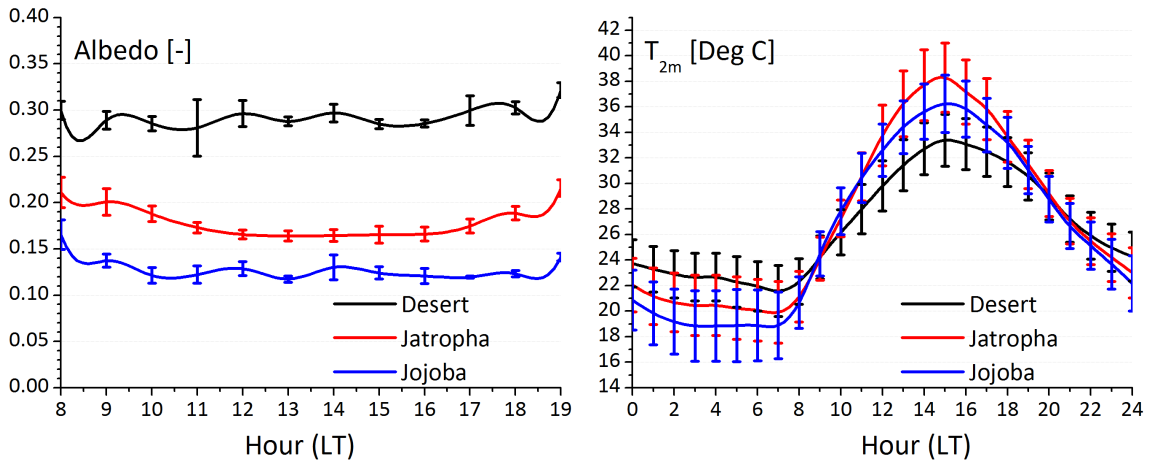


Figure 1.3: Albedo and T_{2m} measurements over *Simmondsia chinensis* (Jojoba), *Jatropha curcas* and desert Loess soils - Hatzetim, Israel (hourly mean and standard deviation - JJA 2012). Measured using a Hukseflux NR-01 4-way radiometer and Vaisala HMP155A thermometer (2 m above surfaces). Only daytime albedo values are shown (08.00 - 19.00).

1.4.3 Roughness length modification

The roughness length (Z_{0m}), or the height above ground level [m] where the mean wind flow theoretically becomes zero, increases with the height of objects. Z_{0m} is generally thought to be around 10% of the mean height of, e.g. plants or buildings. Typical values are 0.001-0.01 m for soils, 0.04-0.20 m for crops and 1.0-6.0 m for forests. The increased roughness length of vegetation, in contrast with bare soil tends to weaken mean surface

¹⁵ This field data was collected specifically for this study

flows such that:

$$\bar{u}(z) = \frac{u_*}{k} \ln \frac{Z - d}{Z_{0m}} \quad (1.3)$$

where $\bar{u}(z)$ is the mean wind velocity at a reference height [m s⁻¹], u_* is the friction velocity [m s⁻¹], k is the von Karman constant (~ 0.4), Z is the reference height, d is a displacement height [m] with $d \sim 0$ for soils and $d > 0$ for vegetation]. d is required when the wind flow above e.g. a forest canopy, effectively becomes uncoupled from the sub-canopy flow such that the aerodynamic surface is effectively displaced upwards. This profile description is valid for neutral surface layers, and for heights above $Z_{0m} + d$, the apparent sink of momentum (Bonan, 2008). Thus the mean wind above the canopy will be slowed in inverse proportion to Z_{0m} . See Appendix 6.1 (Figure 6.5) for statistics of how \bar{U} is slowed and deflected by Jojoba and Jatropha canopies, in comparison to the neighbouring desert surface.

In addition to slowing the mean wind flow, increased roughness also increases mechanical turbulence. We know from Equation 1.1, that an increase in low-level wind shear (second term) increases turbulence kinetic energy. Furthermore, the near-surface wind shear is proportional to the roughness length, for a given wind speed, as implied by Equation 1.2. These descriptions are broad illustrations, and the actual micro-meteorological state over a given canopy is likely to be highly heterogenous with edge, wake and fetch effects in respect to mean wind flow. In that regard, factors like CBL stability and canopy homogeneity, fetch and structure of leaves/stems all come into play (see Raupach and Finnigan, 1996; Pal Arya, 2001, for information on fine scale structures). From a mesoscale modelling point of view some fine details are simply not resolved at typical grid spacings (2-4 km). However, it is not clear how significant such fine-scale effects would be for mesoscale feedbacks, especially for very large canopies.

1.4.4 Moisture availability modification

Soil moisture (η) (and irrigation) play a profound role in the partitioning of Q_H and Q_E , via direct evaporation from bare soils or wet leaves, or plant transpiration. Figure 1.4 indicates potential feedbacks between soil moisture, evaporation and precipitation. A decrease in η (left) means that less available water for Q_E leading to higher Q_H partitioning, for a given R_N . This tends to raise CBL temperatures and evaporative demand and lead to drier soils again. Conversely an increase in η increases Q_E which can eventually dry the soil again if there are no more moisture additions. One uncertainty though is whether an increase in η and Q_E would necessarily lead to increased precipitation (Seneviratne et al., 2010). Even though we might assume a moistening CBL through increased Q_E , a reduced Q_H leads to a suppression of CBL growth and therefore less potential for moist convection. If rainfall does increase, then this should lead to increased η . However, severe runoff and soil cracking could reduce this tendency especially in dry regions (Warner, 2006). Soils

can store water for long periods especially at depth, and η anomalies are associated with ‘climate memory’ effects, even inter-seasonally (Wu and Dickinson, 2004; Seneviratne and Koster, 2012). Furthermore, the time it takes for soils to reach an equilibrium within the hydrological cycle, especially after a rainfall perturbation, can be considerable, and increases with depth (Du et al., 2006). Lim et al. (2012) proposed that arid soils may require particularly long periods, even years to reach equilibrium when compared with a monsoonal climate. The effect of this is that a rainfall perturbation can become self-perpetuating. This mechanism ties in firmly with the causes of desertification and the idea of potentially bi-stable ecosystems (D’Odorico et al., 2013), whereby land cover perturbations (or shifts in climate) cause a positive or negative η perturbation as just mentioned, which then leads to climate persistence.

For the Jojoba scenario, a major consideration in respect to η and by extension the energy balance, will be irrigation/soil plant water relations and how these are represented within the simulation.

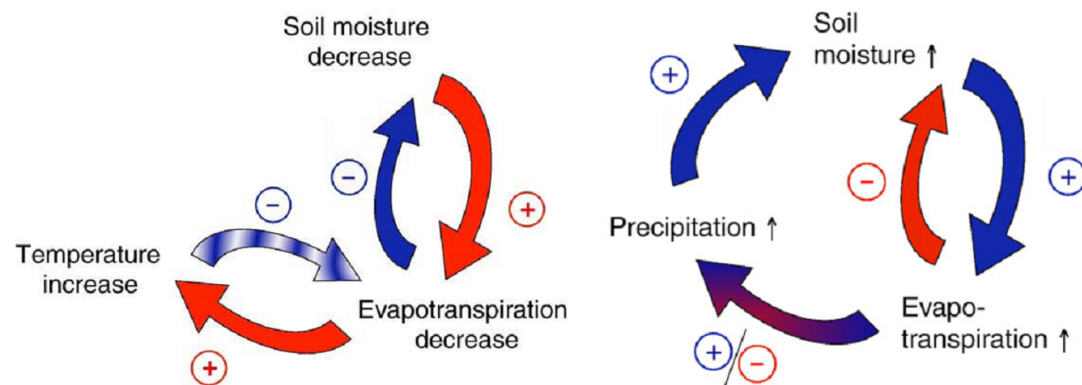


Figure 1.4: Soil moisture (η) feedbacks to the atmosphere from a negative η perturbation (left), and positive on the right. The red arrows denote a drying or warming tendency and blue arrows, moistening or cooling. The striped blue arrow (left) indicates the tendency for increased temperature to lead to higher evaporative demand and the blue/red arrow (right) indicates an uncertain tendency. Adapted from Seneviratne et al. (2010).

1.5 Vegetation feedbacks to arid mesoscale climate

This section will address how the aforementioned mechanisms, which link the land surface to the CBL, can interact with mesoscale phenomena and climate within arid regions.

Interactions between landscape/vegetation/soils and the climate have been discussed for many years, and as a result there is a broad range of theoretical, modelling and/or observational studies, covering tropical to boreal climates. When considering research based in diverse climate zones, it may be that some feedbacks are applicable in all climates. Oth-

ers may be markedly dependent on prevailing conditions. Temperate region ecosystems for instance tend to be radiation rather than η limited, and the climate is dominated by steady ascent - the opposite of many arid regions. Subsidence, or ascent plays a large role in determining stability and entrainment processes (Trier, 2003), and so consequently, identical land surface perturbations may not produce the same impact. Care needs be taken therefore when drawing inferences from findings based on other climates. Because of this, information and examples are selected where possible, according to relevance to: a) arid regions, b) expected impacts, and c) the Jojoba scenario itself, i.e. a contiguous plantation of meso- β dimensions.

1.5.1 The Mesoscale

Before discussing feedbacks to mesoscale climate, it is useful to define the synoptic and the various mesoscales, and the attendant phenomena associated with them, especially because links between meso- and larger scales are discussed later.

Motions in the atmosphere take place over a continuum of spatial scales - from the molecular, to the planetary. Time scales of such motions, range from < 1 second for turbulent motions, up to weeks for Rossby waves. These time scales tend to increase with the spatial dimension of phenomena, and the ratio of horizontal spatial scale to time scale, is generally on the order of 10 m s^{-1} (Markowski and Richardson, 2010). The mesoscale is often defined in terms of its upper boundary, the synoptic scale, which is similar in dimension to mid-latitude pressure systems, i.e. several hundred to several thousand kilometers. As such, mesoscale generally refers to phenomena which are not well represented on historical synoptic weather charts, and associated observation network. Below the synoptic, mesoscales are split into sub-mesoscales in various ways (e.g. Orlanski, 1975; Fujita, 1981). For consistency the Orlanski system is used here. Sub-divisions are defined broadly by the spatial dimensions of specific phenomena. Thunderstorms and urban effects, having dimensions approximately between 2 and 20 km, correspond with Orlanski's meso- γ scale. Lake and mountain disturbances and convective systems with dimensions of 20 to 200 km correspond with the meso- β scale (Markowski and Richardson, 2010). Therefore if we consider plantations with length scales (L_S) of 100 km, and that phenomena such as convective cells and/or circulations could occur in our study area as suggested by Wulfmeyer et al. (2014), then we are potentially dealing with both meso- γ and β scales, depending on the specific phenomena observed.

For synoptic scale phenomena, the assumption of a hydrostatic atmosphere is generally made, where in the vertical equation of momentum, gravitation (g) and the pressure gradient force (PGF), or $-\frac{1}{\rho} \frac{\partial P}{\partial Z}$, both scale approximately to $\sim 10 \text{ m s}^{-1}$ - neglecting viscous and vertical Coriolis forces (Wallace and Hobbs, 2006). Here, ρ is the air density [kg m^{-3}], dP is equal to change in air pressure [Pa] and dZ is equal to the change in height

[m]. Thus vertical accelerations are generally negligible at the synoptic scale and therefore $\frac{\partial w}{\partial t} = -\frac{1}{\rho} \frac{\partial P}{\partial Z} - g$ then becomes $\frac{\partial P}{\partial Z} = -\rho g$ - or the hydrostatic approximation. In general, phenomena where this assumption is valid have aspect scales of $\frac{D}{L} \ll 1$, where D and L are characteristic depth and horizontal length scales [km]. For instance, cyclonic systems may have a $\frac{D}{L}$ of 10/1000 km. However when $\frac{D}{L} \sim 1$ such as in the updraft of a thunderstorm (10 km/10 km), $\frac{\partial w}{\partial t}$ is then similar in magnitude to the vertical pressure gradient force and the phenomena is regarded as non-hydrostatic (Markowski and Richardson, 2010). Small scale phenomena, such as tornadoes and thermals, can have aspect ratios of $\frac{D}{L} \gg 1$, whereas isolated thunderstorms and convective systems can have a $\frac{D}{L} \sim 1$. The aspect ratios of circulations depends on how they are manifested, i.e. a local land/lake breeze or a large coastal front. The hydrostatic or non-hydrostatic nature of phenomena has particular implications for model representation. Meso- γ and β phenomena such as thunderstorms, squall lines and convective systems deviate enough from the hydrostatic balance that they must be treated with full three dimensional equations of motion, used in non-hydrostatic models (Xu et al., 1995), such as WRF, COSMO-CLM¹⁶ and HIRLAM¹⁷.

Whilst the classification and subdivisions of scales is certainly useful, atmospheric motions should still be thought of as part of a broader continuum. Mesoscale phenomena such as convective clouds have lengths, times and velocities which can scale well below the lower bounds of the mesoscale. Conversely, such phenomena can be constrained and initiated by mechanisms scaling well into the synoptic range (Trapp, 2013).

1.5.2 Impact on differential heating and solenoidal circulations

We have discussed how horizontal heterogeneity of η , R_N and Z_{0m} , can induce flux gradients, and modify mean and turbulent wind flows. A known phenomenon associated with horizontal flux gradients, or differential heating, is solenoidal circulations. This term covers any thermally direct flows which are forced by large horizontal temperature gradients (baroclinicity). Such phenomena range from the synoptic and larger, down to length scales of just 1-10 km where the circulation may be restricted to the PBL (Trier, 2003).

At the mesoscale, examples of solenoidal circulations are sea/lake/land breezes and mountain circulations and these may differ in scale, strength, mechanism and persistence (Segal and Arritt, 1992). As these circulations imply, the mechanisms involved in triggering and maintaining circulations differ slightly. In **sea breezes**, contrasts in specific heat and albedo between water and land lead to substantial horizontal diurnal Q_H gradients, where typical values over water are $\leq 50 \text{ W m}^{-2}$ compared to $\geq 450 \text{ W m}^{-2}$ over subtropical coasts (Segal and Arritt, 1992). **Land-only** breezes can be caused by soil moisture gradients and

¹⁶ <http://www.cosmo-model.org/>

¹⁷ <http://www.hirlam.org/index.php/hirlam-programme-53>

at meso- β scales, such circulations are often associated with spatial heterogeneity in rainfall perturbations (Segal and Arritt, 1992). In extreme cases of surface soil saturation, resulting circulations have approached the strength of sea breezes, in similar atmospheric environments (Ookouchi et al., 1984). Directly related are **vegetation breezes** resulting from differential heating between vegetation/soils (e.g. Mahrt et al., 1994; Hong, 1995; Lee and Kimura, 2001), or even between different type of vegetation (Hong, 1995; Pielke et al., 1991). Vegetation breezes are therefore most relevant to arid agroforestry, since it is envisaged that plantations will be implemented on predominantly bare soils.

Horizontal length scale (L_S) is significant for circulations, not only in terms of ‘necessary’ patch size, but also for organizational tendencies of circulations. In order that meso- α and β scale phenomena such as circulations are triggered, it is likely that patches must be of a sufficient density and extent to modify turbulence, and radiative/energy balances over a comparable area (McPherson, 2007). Dalu et al. (1996) suggest that flux gradient scales on the order of 1-10 km, are sufficient to induce significant changes. Letzel and Raasch (2003) estimate scales of around 5 km from LES simulations. Avissar and Schmidt (1998) also suggest that landscape patchiness starts to have a significant impact at length scales of 5-10 km or more. Given that the Jojoba scenario used is a 100×100 km plantation, we may assume that circulations are likely, given strong enough flux gradients. Certainly Wulfmeyer et al. (2014) simulated strong soil/vegetation Q_H gradients using a plantation of the same L_S , and the resulting baroclinicity caused low-level convergence lines and occasionally, CI. There is also evidence to suggest that land circulations tend to organize around a certain L_S . Dixon et al. (2013) found direct correlations between surface measurements of soil moisture and airborne measurements in the Sahel, and indicated strong circulations with length scales on the order of ~ 25 km. Baidya Roy (2003) found that circulations tend to be confined within an L_S range of 10-20 km in Amazonia and the central United States. Significantly in Baidya Roy (2003), the organization doesn’t necessarily match with the dominant patch L_S . He posited that although eddy scales covered a very wide range, land surface interactions acted as a bandpass filter to constrain circulations to an intermediate-range.

The persistence of circulations may depend on background wind speeds. Dixon et al. (2013) state that observed circulations were maintained only at low wind speeds ($\lesssim 5$ m s $^{-1}$). Avissar and Schmidt (1998) found that in a dry atmosphere, a 2.5 m s $^{-1}$ wind flow can severely decrease the impact of circulations on the CBL and that a 5 m s $^{-1}$ flow would eliminate any circulatory effect from ‘realistic’ landscape heterogeneity. Intuitively, this raises the possibility that the strength of gradient, patch size and possibly orientation/configuration, may be a factor in overcoming a given background flow.

Overall, vegetation breezes may produce mesoscale fluxes which are greater than the associated turbulent fluxes alone, and in concentrated areas, or bands of down to a few hundred meters (Mahrt et al., 1994; Lynn et al., 1995). As a result, these circulations may

significantly aid the transport of moisture and heat throughout the PBL (McPherson, 2007). Because of this, land breezes are known precursors for CI, in addition to forced ascent, and turbulent boundary layer motions (e.g. Mahfouf et al., 1987; Hong, 1995).

1.5.3 Impacts from irrigation

If increased η tends to increase Q_E , we could assume that irrigation would cause an increase in CBL humidity, surface evaporative cooling and a suppression of CBL growth. In the absence of large-scale advection, substantial evapotranspiration may increase convective available potential energy (CAPE) driven by increased moisture, but perhaps also a high convection inhibition (CIN) through surface cooling. We could then expect corresponding changes in temperatures, precipitation and cloud cover. Various studies have tried to estimate feedbacks from large irrigated areas, using varying methods and spatial scales. At coarser scales, some studies have run GCMs or RCM¹⁸ simulations of large areas of crops and irrigated areas. Some have used unmodified land use data, to compare the atmospheric state over agricultural landscapes with e.g. more barren land. Others have run ‘control’, and irrigation ‘impact’ scenarios and then compared modelled/observed variables such as fluxes, temperatures and precipitation/cloud cover. Few studies have focussed on arid, non-vegetated regions however.

Most commonly, high evaporative cooling over irrigated canopies is simulated or observed (e.g. Lobell et al., 2009; Cook et al., 2010; Ozdogan and Rodell, 2010). Ozdogan and Rodell cited a change in flux partitioning over irrigated areas favoring Q_E , increased η , reduced R_N , reduced Q_G , and increased runoff. Lobell et al. (2009) found a significant irrigation cooling effect, as did Lobell et al. (2009). Lobell et al. (2009) found large regional differences in this effect and attributed this to the extent of irrigated areas, differences in baseline soil moisture regimes and cloud response.

There are mesoscale modelling studies from arid regions, with similar aims. Alpert and Mandel (1986) observed a reduction in amplitude and variance of U and T_{2m} in Israel over 3 decades. These changes correlated with an increase in irrigation use since the 1960s, and were attributed to lower Q_H and changes in albedo and Z_{0m} . Ridder and Gallée (1998) concurred with these trends. Increases in October rainfall were also found (Otterman et al. (1990); Ben-Gai et al. (1998, 1994, 1993)). Transitional autumn climatic conditions (favoring convection), together with the land surface perturbations were thought to be the cause. Alpert and Mandel (1986) conclude that altered weather patterns were caused by lower Q_H over irrigated crops, whereas Otterman et al. (1990) discuss increased Q_H from non-irrigated shrubs. In Otterman et al. (1990), higher Q_H and lower Q_E magnitudes would result from non-irrigated canopies. In an earlier paper, Otterman (1989) also found that increased dry Saharan fringe-vegetation increased the CBL growth and CI. Sridhar

¹⁸ Regional Climate Models

(2013) simulated an irrigation system in a non-arid region (Pacific NW, USA), in WRF-NOAH and found increased Q_E over the irrigated areas and decreased θ , wind speeds, and PBL height. Qian et al. (2013) also simulated vegetation with an irrigation scheme within WRF-NOAH in the Great Plains Valley, USA and found distinctly higher Q_E partitioning. Wulfmeyer et al. (2014) on the other hand simulated irrigated vegetation in Oman and Mexico in WRF-NOAH, but simulated strong Q_H over the plantation, as well as increases in summer convective precipitation, when compared with a desert surface. There is some observational evidence from arid regions to back up the Wulfmeyer et al. (2014) findings. For instance, we already know from Figure 1.3, that temperatures can be higher over Jojoba and Jatropha canopies than over a desert surface. Another Israel study found a distinct warming effect over a green Kibbutz in the Negev at noon and night time compared to the surrounding desert (Saaroni et al., 2004). They did however notice a slight oasis (cooling) effect during the morning and afternoon. This noontime anomaly could potentially be caused by stomatal closure according to Saaroni et al. (2004) But why do some studies find a warming but some find a cooling effect? The answer is likely to depend significantly on irrigation requirements and methods. For instance, drip irrigation was found to produce $\sim 30\%$ less ET, and requires $\sim 60\%$ less water than flood irrigation methods (Evans and Zaitchik, 2008). Water requirements depend heavily on specific crops and their properties as well as the prevailing climate, where potential evaporation is often used to calculate water requirements (see Allen et al., 1998). Assumptions made about irrigation, and how such assumptions are implemented as parameters can influence modelling results substantially. Wulfmeyer et al. (2014) for instance, used a η target level just above wilting point, whereas Sridhar (2013) set a η target to half way between field capacity and wilting point. Given the direct effect of Q_E/Q_H partitioning on CBL evolution, the importance of correct parameterization of irrigation and plant properties cannot be overstated, if fluxes are to be well reproduced.

1.6 Precursors for convection initiation

This section introduces some important aspects of instability and CI, with a focus on a) processes occurring through the introduction of large desert plantations and b) how larger-scale conditions might govern mesoscale phenomena, if they occur.

In contrast to synoptic scales where phenomena are triggered primarily by baroclinic instability, mesoscale motions can be caused by various types of instability often acting simultaneously - static, inertial, centrifugal, symmetric and shear instabilities (Markowski and Richardson, 2010). The primary trigger for CI discussed by Wulfmeyer et al. (2014) is differential heating, and a consequent pressure perturbation and convergence, occurring within a moist, but otherwise stable environment. It is therefore likely that static instability is the dominant type of instability occurring, although dynamic mechanisms such

as vertical shear may play a role.

Moist convection initiation or CI, occurs when air parcels are lifted until they saturate, achieve positive buoyancy and then accelerate upwards, sometimes to great heights in the case of deep moist convection (DMC). The height at which positive buoyancy occurs is the level of free convection (LFC), essentially where the parcel becomes warmer than the environment. Above this is the equilibrium level (EL), where the parcel temperature becomes equal to the environmental temperature and becomes neutrally buoyant. Static instability and buoyancy can be assessed using parcel theory by comparing thermodynamic properties of a hypothetical parcel with its environment. Parcel theory implicitly assumes that a parcel 1) does not mix with the environment, and retains its identity, and 2) does not produce compensating motions in the environment upon displacement. A simplified vertical equation of motion can then be written as:

$$\frac{dw}{dt} = \frac{d^2z}{dt^2} = -\frac{1}{\rho} \frac{dP}{dz} - g \quad (1.4)$$

where $\frac{dw}{dt}$ is the vertical velocity tendency. In this expression, the viscosity, vertical component of the Coriolis force and effects of moisture on buoyancy, are all neglected. Through some further approximations, it can be shown (from Trapp, 2013, pp 123) that:

$$\Delta z(t) = z_0 \exp \left(-i \left[\frac{g}{\bar{T}_0} (\gamma_p - \Gamma) \right]^{\frac{1}{2}} t \right) \quad (1.5)$$

where Δz is vertical displacement at some future point in time (t), z_0 is the height from which the parcel was displaced [m], Γ is the environmental lapse rate $-d\bar{T}/dz$ [K m^{-1}], γ_p is the dry adiabatic parcel lapse rate ($-dT/dz$), and \bar{T}_0 is the environmental temperature [K]. From this expression, we can say that if $\gamma_p > \Gamma$, then the displacement is **stable** and the parcel oscillates around z_0 at a frequency $\pm \sqrt{(\gamma_p - \Gamma)g/\bar{T}_0}$. If $\gamma_p = \Gamma$ then the displacement is **neutral** and does not change with respect to time. If $\gamma_p < \Gamma$, then the original displacement increases with time and so is **unstable**. Until saturation occurs, a parcel cools at a dry adiabatic rate $\gamma_p = \Gamma_d = g/C_p$ where C_p is the specific heat of air at constant pressure [$\text{J K}^{-1} \text{kg}^{-1}$]. Upon saturation at the LCL, or lifting condensation level the parcel then cools at the saturated adiabatic lapse rate [Γ_s], from Trapp (2013):

$$\Gamma_s = \frac{g}{C_p} \left(\frac{1 + \frac{L_v q_{v,s}}{R_d T}}{1 + \frac{\epsilon L_v^2 q_{v,s}}{C_p R_d T^2}} \right) \quad (1.6)$$

where L_v is the latent heat of vaporization [J kg^{-1}], R_d is the gas constant for dry air [$\text{J K}^{-1} \text{kg}^{-1}$], $q_{v,s}$ is the vapor mixing ratio at saturation [kg kg^{-1}], ϵ is R_d/R_v (where R_v is the gas constant for vapor [$\text{J K}^{-1} \text{kg}^{-1}$]). Then stabilities then become:

$$\Gamma < \Gamma_s \text{ [absolutely stable]}$$

$\Gamma = \Gamma_s$ [saturated neutral]

$\Gamma_s < \Gamma < \Gamma_d$ [conditionally unstable]

$\Gamma = \Gamma_d$ [dry neutral]

$\Gamma > \Gamma_d$ [absolutely unstable]

The above definitions imply infinitesimal displacements and rely upon the comparison of local lapse rates and moist/dry adiabats. Often though, it is more applicable to consider finite displacements, because parcels often need to cover some distance to reach their LFC. Furthermore, an accelerating parcel may gain enough momentum to pass through layers of neutral or stable Γ (Markowski and Richardson, 2010).

On a thermodynamic diagram (area=energy), the area between the LFC and the EL which is bounded by the super-adiabatic parcel path and the moist adiabat, is equivalent to the convective available potential energy (CAPE), thus:

$$CAPE = \int_{LFC}^{EL} B dz \approx g \int_{LFC}^{EL} \frac{T'_v}{\bar{T}_v} dz \quad (1.7)$$

where B is equivalent to buoyancy, expressed as the perturbation virtual temperature (T'_v) relative to the environmental virtual temperature (\bar{T}_v) [K]. The virtual temperature of the parcel is then $T_v = T'_v + \bar{T}_v$. CAPE is equivalent to the kinetic energy, available to the parcel as buoyancy [$J kg^{-1}$], should it reach the LFC. Thus the presence of CAPE is generally a necessary, but not sufficient condition for CI. Analogous to CAPE is convection inhibition (CIN), or the area bounded by the path of a negatively buoyant parcel and the environmental temperature, usually between the surface and LFC, calculated as:

$$CIN = - \int_0^{LFC} B dz \approx -g \int_{SFC}^{LFC} \frac{T'_v}{\bar{T}_v} dz \quad (1.8)$$

CIN represents the work required, for a parcel of air to pass through the stratification and reach its LFC (Trier, 2003). CAPE values of $< 1000 J kg^{-1}$ are considered small, and $> 2500 J kg^{-1}$ are large. Values of CIN $< 10 J kg^{-1}$ are considered small, and $> 50 J kg^{-1}$ are large. In general CIN may be a more useful metric for the likelihood of CI, with a greater CIN requiring more lifting/destabilization for CAPE to be released. CAPE and CIN are both sensitive to low level moisture which evolves such that:

$$\frac{dq_v}{dt} = (-\vec{v} \cdot \nabla_h q) - w \frac{dq_v}{dz} - \nabla_h(\overline{u'q'}) - \frac{d}{dz}(\overline{w'q'}) \quad (1.9)$$

where the first two terms on the RHS are mean horizontal and vertical advection terms, respectively and the last two are horizontal and vertical convergences of the eddy components, respectively. If sufficient low-level moisture is present for CAPE to exist, then CAPE and CIN are also sensitive to temperature lapse rate (Γ), which evolves as:

$$\frac{d\Gamma}{dt} \equiv \frac{d}{dt} \left(-\frac{dT}{dz} \right) = -\frac{1}{C_P} \frac{dQ}{dz} - \frac{d}{dz}(-\vec{v} \cdot \nabla_h T) + \frac{d}{dz}[w(\Gamma_d - \Gamma)] \quad (1.10)$$

where the three terms on the right hand side are equivalent to the differential diabatic heating rate, differential temperature advection and adiabatic temperature change due to vertical motion, respectively. Q is equal to the heating rate [W m^{-2}] and $\vec{v} \cdot \nabla_h(\zeta)$ is the horizontal advection of a variable (ζ) in the u and v directions.

Forecasting of stability is difficult because the above processes may work in concert to create strong reinforcing or cancelling effects. Generally, changes either in q_v and Γ can come about through turbulent fluxes of heat and moisture, horizontal advection and persistent vertical motions. (Trier, 2003).

Turbulent fluxes - The CBL is strongly influenced by heating but the actual evolution of the temperature structure is a complex process. As diurnal heating increases, a corresponding decrease in low-level static instability occurs through differential diabatic heating (1st term on RHS in Equation 1.10). As this heating increases, eddies mix with air of increasing θ at ever greater heights, but CBL growth and destabilization ($d\Gamma/dt > 0$) is strongly dependent on the strength of turbulent motions and the stability of the troposphere above the CBL. Conversely, q_v decreases with height and turbulence causes $\overline{w'q'}$ to be > 0 . However the evolution of CIN and CAPE, as influenced by q_v depends heavily on relative evaporation and entrainment rates. Additionally, a process which decreases CIN, such as a warming, drying CBL can also decrease CAPE simultaneously. Such a situation can occur when entrainment exceeds the evaporation rate into a CBL volume (Trier, 2003).

Horizontal advection - Differential temperature advection (2nd term on RHS in Equation 1.10), leading to more rapid cooling at higher levels, will then lead to a destabilized Γ . If lower level warm advection occurs alongside increased horizontal moisture advection (1st term on RHS in Equation 1.9), this can increase CAPE and also reduce CIN simultaneously (Trier, 2003). At synoptic scales, differential advection of temperature is likely the most significant driver of $d\Gamma/dt$ with scales up to an order of magnitude greater than other determining processes. At mesoscales, the other terms can become much more significant (Markowski and Richardson, 2010).

Vertical motions - Although CIN can be reduced by the two mechanisms above, some low-level ascent is still likely to be required, to initiate convection and to maintain it for longer than \sim one hour, or the lifetime of a single cumulus cloud. This implies that turbulence alone may not be enough to trigger significant and persistent convection, such as that observed by Wulfmeyer et al. (2014). This is especially likely in the presence of large-scale tropospheric subsidence, which increases CIN. Having said that, in the presence of low CIN, turbulence may actually determine the location where convection is first initiated (Trier, 2003).

There are several mechanisms leading to mesoscale ascent, such as orography, drylines, solenoidal circulations and convectively forced mechanisms (Trapp, 2013). Wulfmeyer

et al. (2014) observed convergence as the lifting mechanism, but the fact that CI did not occur daily makes it likely that suitable priming of the atmosphere (CIN and CAPE) by turbulent transport and advection must occur, before such a circulation can induce CI. It is possible also, that the strength and nature of the convergence itself is a factor, as well as the presence of CAPE and CIN.

1.7 Summary of key knowledge gaps

1.7.1 Simulation of irrigated plantations - Chapter 2

Becker et al. (2013) provided a good basis for simulating arid agroforestry scenarios, (Jatropha) but some questions and gaps remain for the simulation of Jojoba:

1. A detailed simulation of irrigation is still missing from simulations of agroforestry even though the sensitivity of energy flux partitioning to irrigation (η) assumptions is clear from Section 1.5.3. Any irrigation simulation should reflect climate, soil and species characteristics in order to maintain a basis in reality (e.g. see Allen et al., 1998), and preferably should be based on actual plantation methods.
2. Energy fluxes are sensitive to plant properties like R_{st} (Groner, 2013), LAI, Z_{0m} , and canopy cover. Jojoba R_{st} can change with local conditions such as soil salinity and stress (Rao et al., 2000; Hussain et al., 2011). However detailed information on Jojoba and local soils needs to be researched and incorporated into simulations.
3. It is not certain how a) fluxes would be partitioned over a realistic irrigated plantation, nor b) how strong the plantation/desert gradients would actually be, and c) even what sign the gradient would be. This highlights the need to obtain realistic fluxes for plantation and desert surfaces. Furthermore, validation of plantation/desert fluxes (and other standard quantities) is required, to assess flux magnitude and gradient representation.

1.7.2 Climate impacts and precursors - Chapter 3

Wulfmeyer et al. (2014) provided a good foundation for understanding the mechanisms of arid agroforestry-induced CI under certain conditions, but some questions remain:

1. Impact studies are needed to substantiate the results of Wulfmeyer et al. (2014) and to see if similar impacts occur using a validated model configuration, including new irrigation scheme.
2. A deeper look at processes is required, particularly with regard to the overcoming of stability, vertical transport of moisture and organisation of circulations.

3. It is not clear how significantly the prevailing climate can influence plantation impacts. This could be tested by comparing impacts in different regions, and over different time periods, e.g. dry/moist days.
4. It is not known why CI occurs only sporadically in Wulfmeyer et al. (2014), given the regular clear skies and the constant land surface perturbation. Underlying reasons for convection initiation/failure and strength need to be examined.
5. Assuming that CI can be triggered, but only under certain climatic conditions, then the location may determine the probability and manner of impacts. Controlling impacts by selective placement requires an a priori identification of:
 - a) specific mechanisms leading to climate modification.
 - b) conditions or thresholds determining those impacts.
 - c) locations where such conditions are common.

1.7.3 Resulting questions

In order to crystalize the aims of the thesis and provide a reference for later discussion and conclusions, some questions are formulated:

1. *Can desert and Jojoba land surfaces be simulated in a reasonable way by WRF-NOAH, so that mean diurnal fluxes and other quantities correspond well with field observations?*
2. *How do 100×100 km Jojoba plantations modify the summer mesoscale climate in Israel and Oman, particularly regarding CBL processes and CI?*
3. *What are the primary mechanisms and precursors for these impacts?*
4. *Is there a potential for regional selection whereby impacts are more likely?*

1.8 Objectives

To address the above questions systematically, the experiment is structured according to the work flow in Figure 1.5, followed by the specific objectives for each section.

Setting up and validating the model: simulating a Jojoba plantation (Ch.2)

1. Collect surface meteorological data from 3 stations in Israel - JJA 2012
 - Irrigated Jojoba plantation
 - Irrigated Jatropha plantation
 - Desert surface

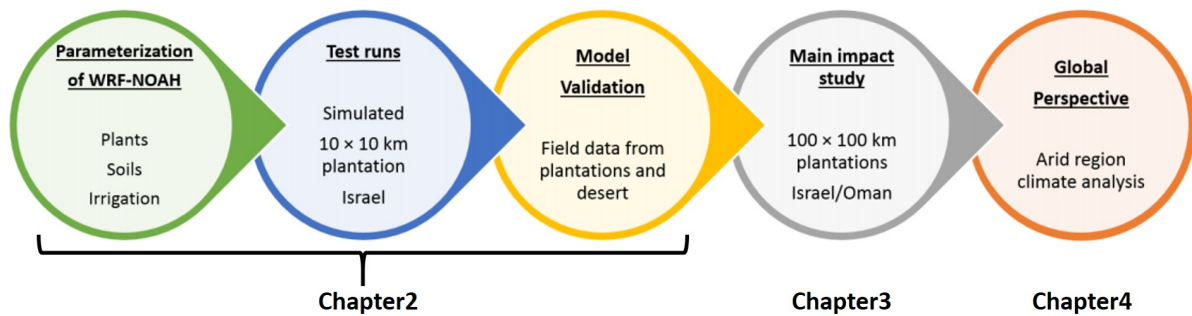


Figure 1.5: Schematic of thesis work flow.

2. Optimize soil and vegetation parameter sets for Jojoba and desert land surfaces Parameters: albedo, Z_{0m} , LAI, minimum stomatal resistance ($R_{st,min}$), and vegetation fraction
Source: literature, local knowledge and observations
3. Design and code a controllable irrigation scheme for NOAH. The simulation should mimic the sub-surface system used at the observation Jojoba plantation
4. Run two validation scenarios in Israel - Summer 2012 (12 weeks + spin up)
CONTROL (unmodified land surface - predominantly desert soils)
IMPACT (artificial 10 × 10 km plantation inserted)
The simulated plantations are geolocated within WRF-NOAH, to match the observation sites
5. Validate diurnal quantities from CONTROL with *Desert* observations, and IMPACT with *Jojoba* observations (means and variance)

Applying the model: impact study of arid plantations (Ch. 3)

5. Scale up plantations to 100 × 100 km and run CONTROL and IMPACT again, but this time comparing two regions - Israel and Oman
Summer 2012 (4 weeks + spin up)
6. Analyze and compare CONTROL and IMPACT for both regions - especially precipitation, sea level pressure, u and v , vertical motions w , and T and q_v profiles
7. Assess common factors, precursors and thresholds for impacts

Global Perspectives (Ch. 4)

8. If applicable, apply knowledge of processes and precursors, to a global scale climate analysis

Chapter 2

Setting up and validating the model: simulating irrigated plantations

This chapter presents a synopsis of methods and results from the published article by:

Branch, O., Warrach-Sagi, K., Wulfmeyer, V., Cohen, S., 2014. Simulation of semi-arid biomass plantations and irrigation using the WRF-NOAH model - a comparison with observations from Israel. *Hydrology and Earth System Sciences*, 18(5), pp.17611783. Available at: <http://www.hydrol-earth-syst-sci.net/18/1761/2014/>.

2.1 Introduction

The goal of this chapter is to simulate a moderate sized irrigated plantation in the desert and validate the model with relevant observation data from Israel. In doing so, we assess the ability of WRF-NOAH to reproduce surface quantities over both plantation and desert land surfaces. We have discussed that flux partitioning determines diurnal CBL evolution, and that differential heating can set up circulatory motions. Strong sensible heating and roughness drive turbulence and the mixing of scalars throughout the CBL. Convergent circulations can provide a strong lifting mechanism and a reduction of CIN, perhaps enough to trigger moist convection. We have also established that CI is a non-linear, or ‘threshold’ phenomenon, not least because parcels must usually undergo finite displacements to reach their LFC. It is therefore important that absolute magnitudes of surface quantities over *both* desert and Jojoba surfaces are well simulated. Absolute magnitudes are important, because \bar{U} drives shear turbulence, and Q_H drives buoyancy-induced turbulence, both of which are important components of CBL evolution and CI. Representing the desert surface is also important because the spatial contrast between surfaces determines horizontal flux gradients.

Although the scenario used here is based loosely on Becker et al. (2013) and Wulfmeyer et al. (2014), there are some important differences. Instead of *Jatropha*, the remarkable Jojoba plant is used as a basis for parameterization. One of the reasons for switching from *Jatropha*, is because an impressive 400 ha Jojoba plantation at Kibbutz Hatzerim, Israel¹ was made available for collecting meteorological observations and irrigation/soil data (31.24° N, 34.72° E). The second addition to the scenario is a coded sub-surface irrigation designed to mimic that used at Hatzerim.² Given the strong influence of plant/soil properties and moisture availability on model/actual fluxes, it is important to optimize parameters with respect to species and environmental factors such as climate, soil moisture and salinity. Locally obtained knowledge provided a useful source of data for irrigation quantities and soil data³.

Once parameterized, the plantation was physically simulated by insertion of the required area into the MODIS land surface data, with prescribed soil and vegetation parameters and irrigation. For validation, surface observations were collected from the center of the 400 ha Jojoba plantation (station name - *Jojoba*), and from a nearby desert surface (*Desert*) over the corresponding period⁴. Energy balances for *Jojoba* were calculated using two Penman-Monteith evapotranspiration models (Penman, 1948; Monteith, 1965). For simulation, two model case studies, IMPACT and CONTROL were run for comparison and to test flux magnitudes over desert and vegetated surface types. CONTROL utilizes unmodified land surface data (predominantly bare desert soils), and IMPACT contains the inserted plantation. CONTROL was validated with *Desert* observations and IMPACT with *Jojoba* data.

A synopsis of the WRF and NOAA models, configuration, forcing data, domains and execution now follows in Section 2.2. The most salient parts of the plant/irrigation parameterization are summarized in Section 2.3. The field campaign and validation methodology are in Section 2.4. Validation results are presented in Section 2.5, and the experiment is summarized in Section 2.6 (see Branch et al., 2014, for a deeper description of the experiment). Please refer to section 1.2.2 for relevant climate information for central Israel.

¹ See Benzioni (1995) for a historical overview of Jojoba cultivation in Israel

² NETAFIM, a world leader in drip irrigation systems, was founded at Kibbutz Hatzerim, and oversees the management of the Jojoba plantations

³ NETAFIM agronomists [for irrigation data], and Gilat Agricultural Research Center (ARO - Volcani) [for soil data]

⁴ Observations were taken from a nearby 2 ha *Jatropha* plantation (*Jatropha*) for comparison with Jojoba (e.g. Figure 1.3), but this was not used explicitly for validation

2.2 Methodology - Model configuration, duration & spin-up

2.2.1 The WRF-NOAH coupled atmosphere-land surface model

All simulations were run using the WRF⁵ atmospheric model with ARW⁵ core (version 3.4.1), coupled to the NOAH community land surface model or LSM. Here follows a brief description of each:

WRF-ARW - The ARW solver uses a set of fully compressible, Eulerian non-hydrostatic primitive equations. Prognostic variables are u and v in Cartesian coordinates, vertical velocity w , perturbation (potential temperature, geopotential, and surface pressure of dry air. The vertical coordinate (σ_v) is terrain-following, dry hydrostatic-pressure with the top of the model defined as a constant pressure surface. Time-split integration (with variable time capability), follows a 2nd- or 3rd-order Runge-Kutta scheme with sub-time steps for acoustic and gravity-wave modes. Spatial discretization is 2nd- to 6th-order advection in horizontal and vertical. The model comes packaged with a range of physics schemes for microphysics, cumulus, multi-layer land surface models, surface layer, PBL, and atmospheric radiation. See Skamarock et al. (2005) for a detailed technical description.

NOAH LSM - This LSM is based on the coupling of the Penman potential-evaporation approach of Mahrt and Ek (1984), the multi-layer soil model of Mahrt and Pan (1984), and the canopy model of Pan and Mahrt (1987). It now includes the more complex canopy resistance, added by Chen et al. (1996) to include the approaches of Noilhan and Planton (1989) and Jacquemin and Noilhan (1990). NOAH uses a single canopy layer and calculates prognostic variables: soil temperature and moisture in the soil layers, canopy water storage, and ground snow storage. To simulate soil moisture, four soil layers are used with thicknesses of 0.1, 0.3, 0.6, and 1.0 m, starting from the surface layer to the deepest, representing a total depth of 2 m (see Equation 2.2 for soil water transport). The root zone is in the upper 1 m of soil, and the lower 1 m soil layer forms a reservoir with gravity drainage at the bottom. Rooting depth (layers) can be specified as a function of vegetation type. See Chen and Dudhia (2001) for further description.

2.2.2 Modelling methodology

The concurrent CONTROL and IMPACT simulations were set up in WRF-NOAH using a 444×444 cell gridded domain, 92 vertical levels and a 2 km horizontal grid increment. A single downscaled domain was chosen to incorporate significant large scale features, such as the steady influx of sea air from the north-east, whilst at the same time avoiding orography and other significant features at the boundaries (See Fig. 2.1, overleaf).

⁵ Advanced Research WRF (Weather Research and Forecasting) model

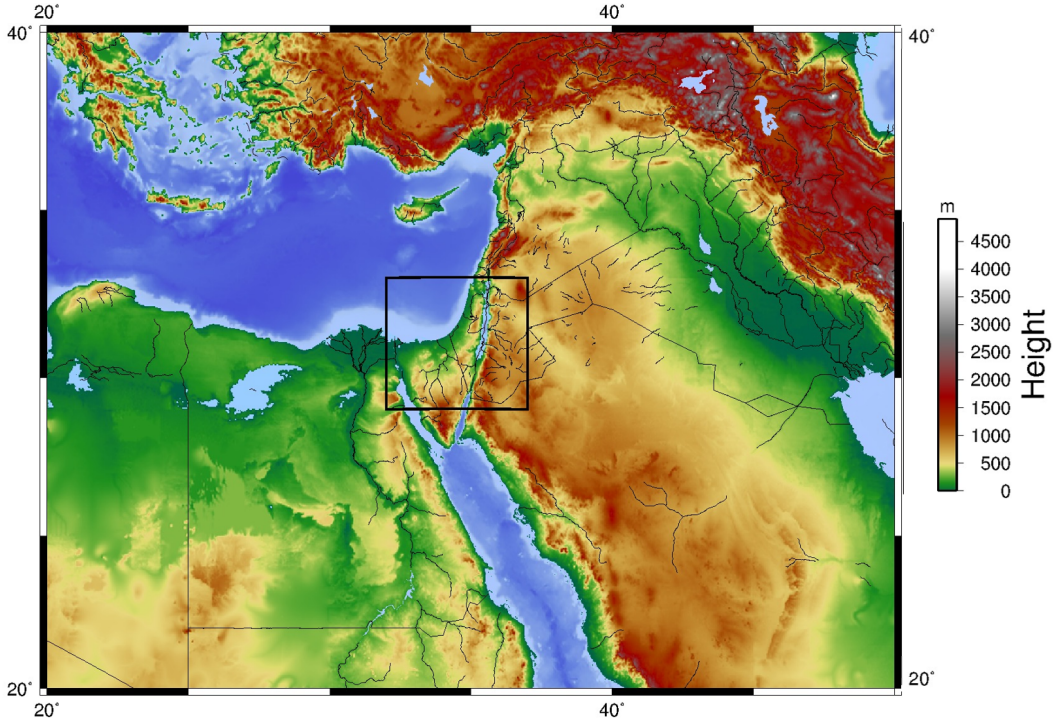


Figure 2.1: Topographic map of the eastern Mediterranean [m]. The model domain (approx. 888×888 km) is marked in the centre with a black line.

The model physics schemes used (Table 2.1) were chosen with consideration to:

- literature studies, relevance to arid regions and suitability for convective PBL
- experience and sensitivity tests within the working group and WRF community
- schemes that are designed to be paired, e.g. short/longwave RRTMG schemes and Yonsei PBL (YSU)/MM5 surface layer schemes.

Table 2.1: Physics schemes used in WRF-NOAH and appropriate references

Physics	Scheme	References
Boundary layer	YSU (Yonsei University)	(Hong et al., 2006)
Surface layer	MM5 Monin-Obhukov	(Dyer and Hicks, 1970; Paulson, 1970)
Microphysics	Morrison 2-moment	(Morrison and Gettelman, 2008)
Shortwave radiation	RRTMG	(Iacono et al., 2008)
Longwave radiation	RRTMG	(Mlawer et al., 1997)

The YSU turbulence scheme used, has already been used for various publications relating to arid regions (Becker et al., 2013; Wulfmeyer et al., 2014), and is generally thought to perform well in unstable convective conditions (Hu et al., 2010; Shin and Hong, 2011), which is most relevant for CBL fluxes. It is a non-local scheme and explicitly handles entrainment. The MM5 surface layer scheme, which computes surface exchange coefficients of heat, moisture and momentum using Monin Obhukov stability functions, is to be

paired with the YSU scheme. The Morrison 2-moment microphysics predicts total number concentration of ice species and may improve the representation of ice crystal aggregation and ice cloud radiation representation (Morrison and Gettelman, 2008). One study which used Morrison with WRF (Molthan and Colle, 2012), cited that it gave the minimum difference between simulated and accumulated precipitation during a convective storm when compared to 5 other schemes.

The model was forced at the boundaries by 6-hourly ECMWF analysis data⁶ with a 0.125° grid increment and 6-hourly updated sea surface temperatures (SSTs). The model was run, with an 18 second integration timestep, from May 1st until August 31st 2012 (May was used as model spin-up time and disregarded for analysis). During 2012, no El Niño or La Niña events occurred, which is significant due to known correlations between such events and impacts on the Indian Monsoon, and the Middle East climate (e.g. see Kumar et al., 2006).

2.3 Methodology - Parameterization of irrigated Jojoba

It was intended to mimic conditions at the *Jojoba* plantation, particular relating to: location, vegetation/soil parameters and sub-surface irrigation. A 10×10 km plantation was inserted at the center of the domain, in the northern Negev (see Figure 2.2) with the center grid cell geo-located (within WRF) to match the locations of the *Desert* and *Jojoba* stations (which are ~ 1 km apart). The idea is to allow for direct comparison of surface quantities, whilst assuming similar atmospheric conditions (as forced by ECMWF analysis data).

Land surface modification The selected grid cells for the plantation were first re-classified from “Desert scrub” to “Evergreen Broadleaf” classification as a starting point (in the MODIS⁷ land surface data). Then, parameters for canopy height, minimum resistance ($R_{st,min}$), roughness length (Z_{0m}), and LAI were modified further based on sensitivity tests and site surveys (see Table 2.2) and also literature: for Jojoba (Benzioni and Dunstone, 1988; Benzioni, 1995) and *Jatropha* (Niu et al., 2012; Rajaona et al., 2012, 2013; Wulfmeyer et al., 2014).

⁶ Data used in this study/project have been obtained from the ECMWF Data Server (European Centre for Medium Range Weather Forecasting) - Format: Analysis data with

⁷ IGBP Moderate Resolution Imaging Spectroradiometer (MODIS) modified land surface data (Justice et al., 2002)

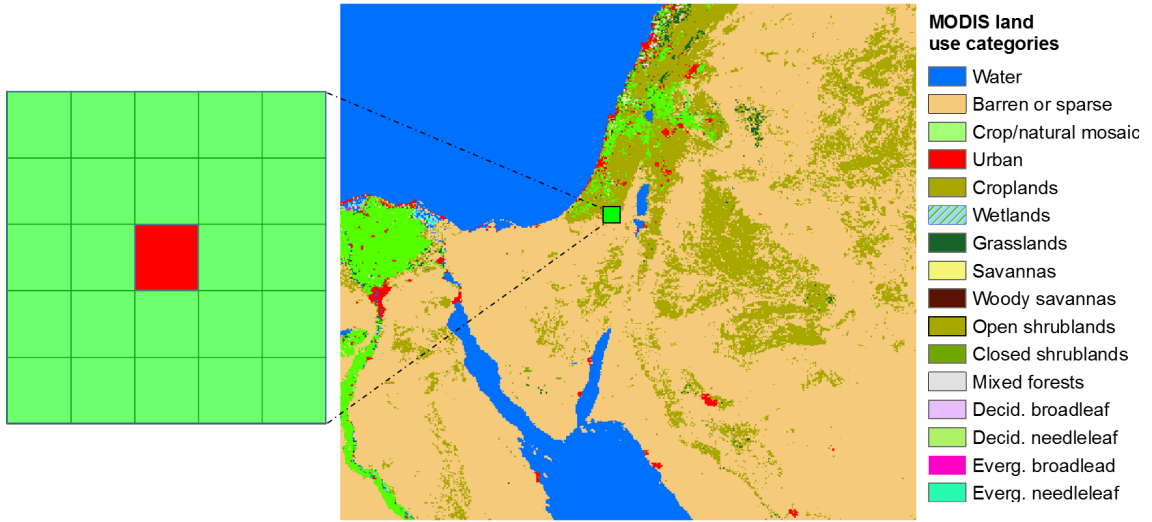


Figure 2.2: Model domain extent for IMPACT and CONTROL centred over Israel at the eastern end of the Mediterranean (right). The gridded map (center) represents the MODIS land surface categorical data used within NOAH with the categories listed on the right. The simulated plantation is represented by 5×5 (2km) grid cells (left) and shown in the center of the domain (not to scale). The center red grid cell of the 5×5 box corresponds geographically to the actual *Desert* and *Jojoba* observation sites in order to ensure the optimal match between real weather conditions and that from the forcing data. The simulated plantation is located mainly on dry barren/sparse soils but with some croplands upwind to the north.

Table 2.2: Vegetation parameters prescribed for the simulation of the Jojoba plantation based on literature, site surveys and local knowledge.

Variable	Default	Prescribed	Source
Roughness - Z_{0m} [m]	0.5	0.3	Literature, measured canopy height
Albedo [-]	0.12	0.12	Observations
Veg. Fraction [%]	95	70	Local knowledge, aerial imagery
$R_{st,min}$ [$s\ m^{-1}$]	120	250	Literature, Verification adjustment
LAI [$m^2\ m^{-2}$]	5	3.2	Literature

Irrigation The irrigation simulation is based on a soil moisture (η) target level and was to be coded as a sub-routine within NOAH. The irrigation at Hatzerim is an automated sub-surface deficit irrigation system, monitored by moisture sensors and has dripper arrays at ~ 30 cm depth. The method is designed to minimize losses to the surface and to percolation.

To calculate an appropriate irrigation input, based on η , a method from Choudhury and DiGirolamo (1998) was used. They collated critical values of fractional root zone available water (F_{AW}) for various species, from various publications. If η falls below F_{AW} then the plant is deemed to be water stressed. F_{AW} is given as:

$$F_{AW} = \frac{\eta - \eta_{wp}}{\eta_{fc} - \eta_{wp}} \quad (2.1)$$

where η_{wp} is the soil wilting point and η_{fc} the field capacity. Estimated F_{AW} values have

not been estimated specifically for Jojoba, but values for plants of a similar biomass do not vary greatly in any case - mostly between 0.3 and 0.4. A value for Sorghum was chosen (0.36), because like Jojoba it thrives in semi-arid regions. Rearranging for η and using sandy loam as a soil texture, this yields a η value of $0.18 \text{ m}^3 \text{ m}^{-3}$ and is assumed to be the minimum permissible η level for the plant. This was set for the irrigation target level.

A discretized Richards equation is used by NOAH (Chen and Dudhia, 2001) for vertical transport of η through its four soil layers. These layers have thicknesses of: 10, 30, 60 and 100 cm from the surface layer downwards and a free drainage scheme was used at the lower boundary. The discretized Richards equation is given as:

$$\begin{aligned}
 d_{z1} \frac{\partial \eta_1}{\partial t} &= -D \left(\frac{\partial \eta}{\partial z} \right)_{z1} - K_{z1} + P_D - R - E_{dir} - E_{t1} \\
 d_{z2} \frac{\partial \eta_2}{\partial t} &= D \left(\frac{\partial \eta}{\partial z} \right)_{z1} - D \left(\frac{\partial \eta}{\partial z} \right)_{z2} - K_{z1} - K_{z2} - E_{t2} + \mathbf{I}_2 \\
 d_{z3} \frac{\partial \eta_3}{\partial t} &= D \left(\frac{\partial \eta}{\partial z} \right)_{z2} - D \left(\frac{\partial \eta}{\partial z} \right)_{z3} - K_{z2} - K_{z3} - E_{t3} + \mathbf{I}_3 \\
 d_{z4} \frac{\partial \eta_4}{\partial t} &= D \left(\frac{\partial \eta}{\partial z} \right)_{z3} - D \left(\frac{\partial \eta}{\partial z} \right)_{z4} - K_{z3} - K_{z4} - E_{t4}
 \end{aligned} \tag{2.2}$$

where D is hydraulic diffusivity [$\text{m}^2 \text{ s}^{-1}$], K is the soil hydraulic conductivity [m s^{-1}], P_D is precipitation [mm s^{-1}], R is surface runoff [mm s^{-1}], E_{dir} is direct evaporation from the surface [mm s^{-1}], E_{ti} is the layer root uptake [mm s^{-1}] and subscript z_n denotes the n th soil layer. The soil was irrigated by adding an extra irrigation term \mathbf{I}_2 and \mathbf{I}_3 [mm s^{-1}] to the second and third layer, corresponding approximately with the *Jojoba* irrigation depth of 30 cm. To add the water, the following logical statement was executed every seven days: "IF $\eta < 0.18$ THEN add water at $0.0004 \text{ mm/timestep}$, but IF $\eta \geq 0.18$ THEN do not add water". The irrigation rate was set to a slow rate to avoid matrix water balance errors. Due to the homogeneous watering in the model, drainage is very slow and little significant change in η was observed over the seven day intervals. For all intents and purposes, we can more or less assume the η level to be a constant for these two soil layers within the plantation.

2.4 Methodology - Validation

For validation, the following measurements were collected: air temperature (T_{2m}), relative humidity (RH) [%], 4-way radiation components (SW \downarrow , SW \uparrow , LW \downarrow , LW \uparrow), ground heat flux (Q_G), 5cm soil temperatures (ST $_{5cm}$), wind speed (U) and direction U_{dir} were recorded at the *Desert* and *Jojoba* stations every 5 minutes. See Table 2.3 for details of measurement

and estimated error. See Figure 2.3 for photos of the measurement sites and Appendix 6.1 for details of station locations and measurement statistics for the summer of 2012.



Figure 2.3: Measurements taken over the 400 Ha *Jojoba* plantation (left) and at the dry *Desert* station (right), using 6m towers both located at Kibbutz Hatzetim near Beer'sheva, Israel.

Table 2.3: Measured variables at *Desert* and *Jojoba* including error estimation.

Quantity	Sensor	Estimated error
2m air temperature (T_{2m})	Vaisala HMP155A	$\pm 0.055 + 0.0057 \cdot T$ @20 °C
2m relative humidity (RH)	Vaisala HMP155A	$\pm(1.0 + 0.008 \cdot RH)$ @-20 ° +40 °C
4m 4-way radiation (SW/LW)	Hukseflux NR01	$\pm 10\%$ for 12 hour totals
6m wind speed (U and U_{dir})	Gill 2D Windsonic	$U \pm 2\%$ and $U_{dir} \pm 2 - 3^\circ$
2m barometric surface pressure (P)	Vaisala CS106	0.6 hPa @ 0 to +40 °C
Soil temperatures at 5cm (ST_{5cm})	CS 108 Thermopile	$\pm 0.3^\circ\text{C}$ @ -3 to 90 °C
8cm soil heat flux (Q_G , two plates)	Hukseflux HFP01	-15% to +5% for 12 hour totals

From the radiation components, net surface radiation (R_N) was calculated as $SW_{\downarrow} - SW_{\uparrow} + LW_{\downarrow} - LW_{\uparrow}$. Vapor pressure deficit (VPD) was derived as: $e_s - e_a$ where e_s is the saturated water vapor pressure and e_a is the actual vapor pressure (hPa). For calculation of latent heat flux (Q_E) over the plantation⁸, ET was calculated using two Penman-Monteith methods (Penman, 1948; Monteith, 1965):

- combination Penman-Monteith equation (known as Penman R_a/R_s)
- modified Penman Monteith ASCE method (Penman 56 FAO)

Penman R_a/R_s is based on the so-called combination Penman-Monteith equation (Monteith, 1965), which includes explicit surface and aerodynamic resistances.

Penman 56 FAO (Allen et al., 1998) is a standard analytic/empirical method, developed by the Food and Agriculture Organisation (FAO), and useful when stomatal resistance data are not available. It describes a potential, or reference ET (ET_0) of a well-watered

⁸ ET over *Desert* is assumed to be virtually zero, barring some dew formation

vegetated grass surface (canopy height of 0.12 m, a constant R_s of 70 s m^{-1} and an albedo of 0.23). This ET_0 value is then modified with a crop coefficient K_c , associated with particular plant types. See Appendix 6.2 for descriptions of both methods. Finally the sensible heat flux was calculated as the residual of the energy balance: $Q_H = R_N - Q_G - Q_E$.

For validation, model output values are based on calculated spatial average of the plantation footprint, the 25 cell grid box (from Figure 2.2). In Figure 2.4 and 2.5, the seasonal hourly mean and standard deviations (σ_{dev}) of the directly measured variables (T_{2m} , VPD, U, R_N , Q_G , and ST_{5cm}) are compared - CONTROL against *Desert* observations - IMPACT against *Jojoba*. Table 2.4 then summarizes the maximum model deviations for these variables. Finally Q_E and Q_H fluxes are compared in Figure 2.6.

2.5 Results - Validation

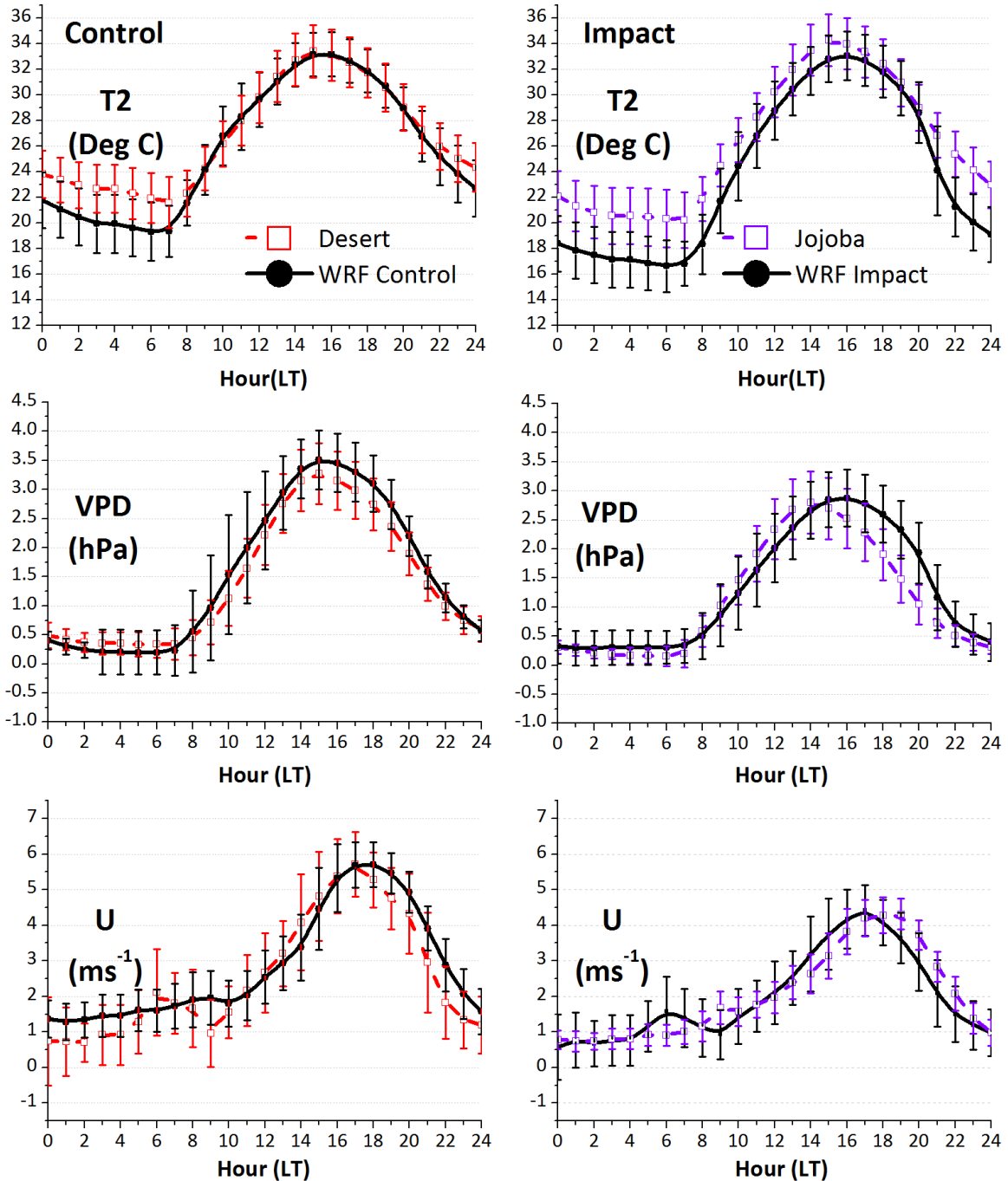


Figure 2.4: Comparison of mean summer diurnal cycles of 2m temperature (T_{2m}), 2m vapour pressure deficit (VPD), wind speed (U) - for CONTROL and IMPACT. Dotted lines are observations and solid lines are model output. WRF variables were averaged over a 25 grid cell box. Note that U observations have been extrapolated from the measurement height of 6 m to 10 m for equivalence with U_{10m} in WRF

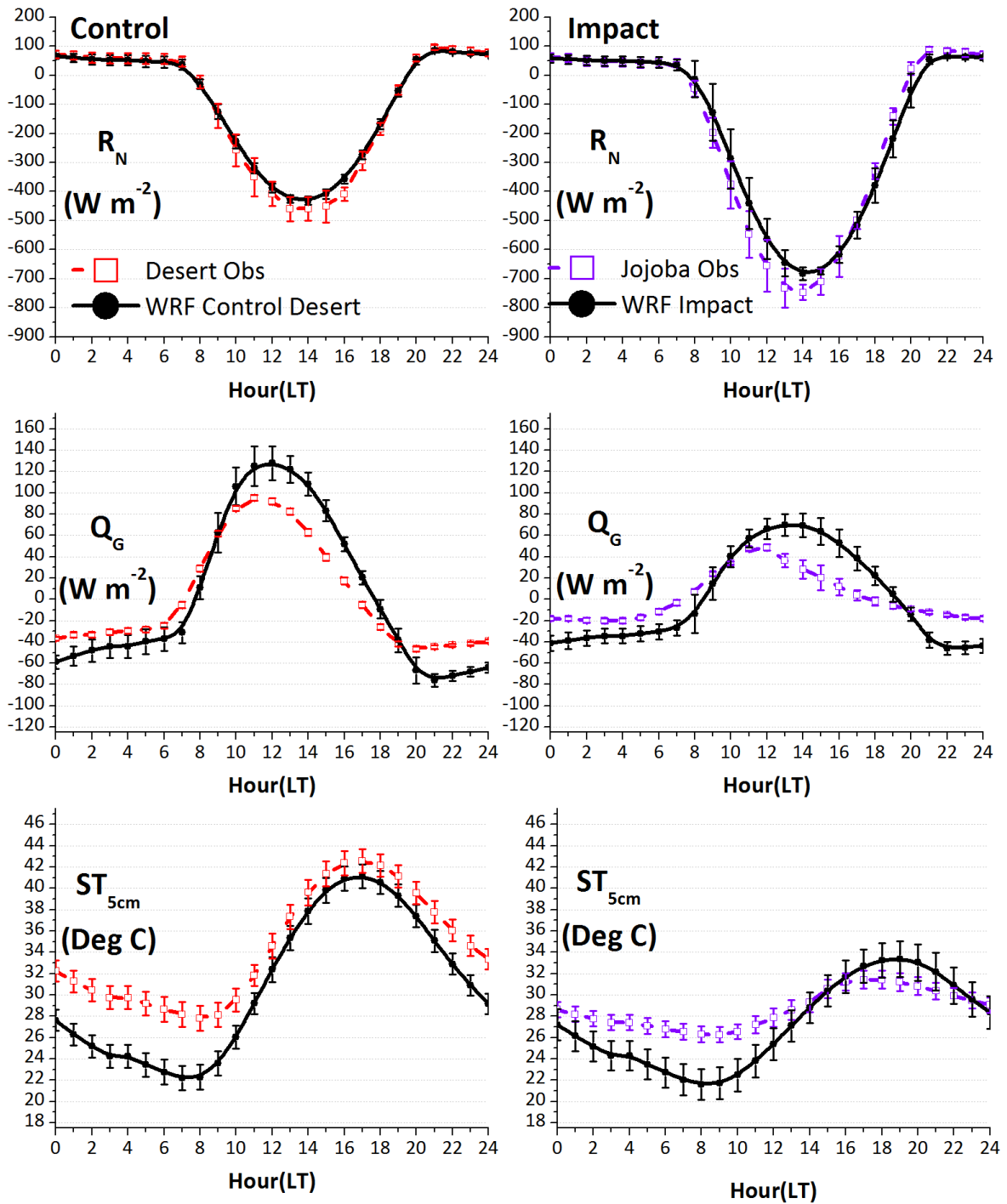


Figure 2.5: Comparison of mean summer diurnal cycles of net surface radiation (R_N), ground flux (Q_G) and 5cm soil temperatures (ST_{5cm}) - for CONTROL and IMPACT. Dotted lines are observations and solid lines are model output. WRF variables were averaged over a 25 grid cell box.

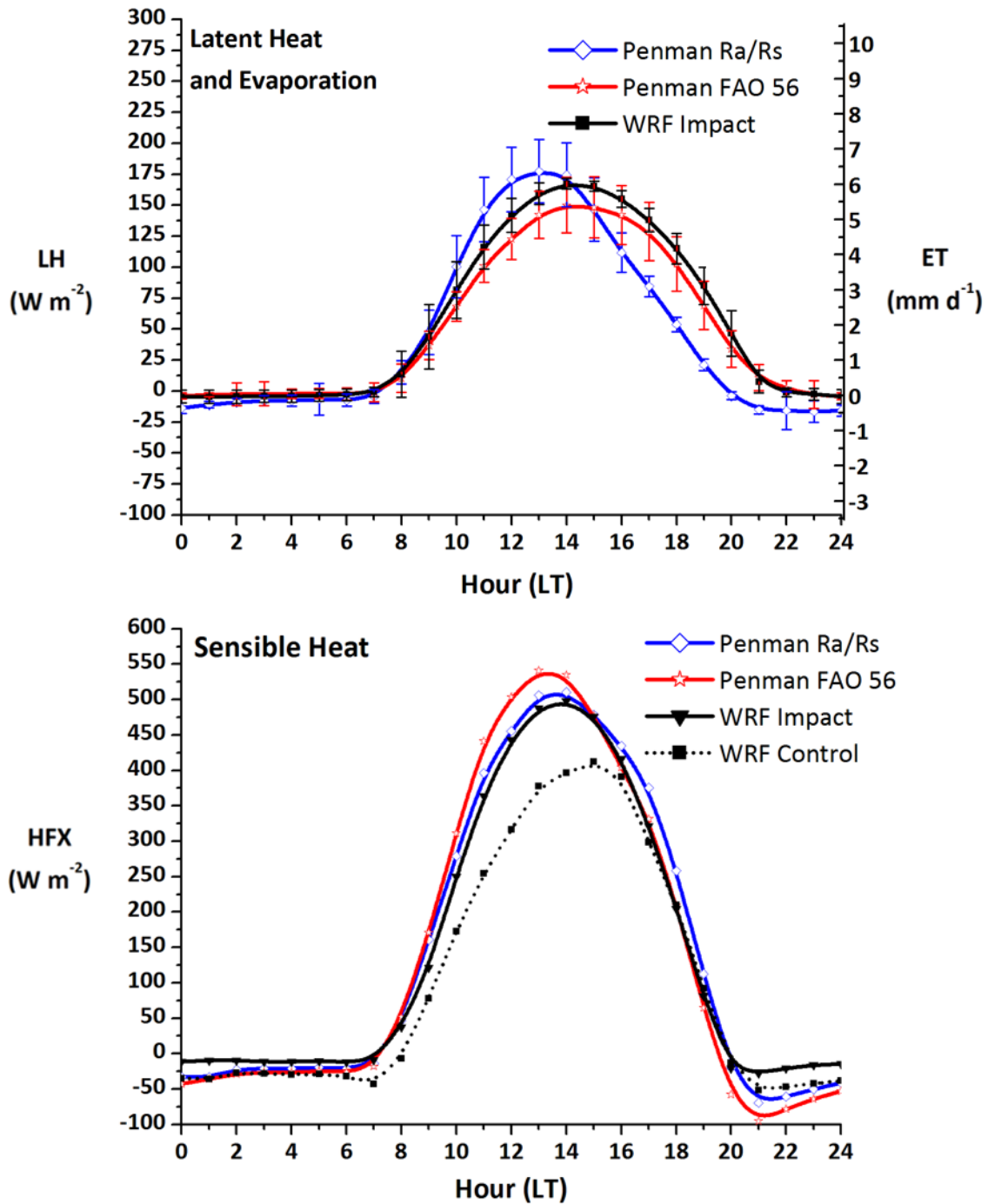


Figure 2.6: Mean summer diurnal cycles of observed and modelled Q_E (left) from IMPACT (black) and from PM Ra/Rs and PM FAO 56 (colored) and standard deviations. ET is expressed in both $W m^{-2}$ (left Y axis) and $mm d^{-1}$ (right axis). The right hand plot shows the Q_H fluxes from IMPACT and also Q_H based on the Penman estimates, calculated as : $Q_H = R_n (obs) - Q_G (obs) - Q_E (calculated)$. Q_H from CONTROL is plotted to show the difference in Q_H between desert and plantation.

Table 2.4: Summary of maximum WRF-NOAH deviations from mean observations in directly measured variables (daytime only - 08.00 - 19.00 LT).

Simulation	T_{2m} ($^{\circ}\text{C}$)	VPD (hPa)	U (m s^{-1})	R_N (W m^{-2})	Q_G (W m^{-2})	ST_{5cm} ($^{\circ}\text{C}$)
CONTROL	0.2	0.25	0.5	25	30	1.5
IMPACT	1.5	0.5	0.5	50	20	2.0

T_{2m} - IMPACT has a slight cold bias during morning and midday in contrast to CONTROL (Figure 2.4, top panels) but the reasons for this are not clear. Measurement error is likely to be negligible (see Table 2.3). Perhaps the IMPACT night time cold bias is carried over somewhat into the CBL. Another possible cause is the IMPACT R_N time lag during this period. Other possibilities are advection effects due to the disparity in simulated and real plantation sizes. The night time T_{2m} cold bias is large and this is reflected in ST_{5cm} (bottom right) and a correspondingly low upwelling long wave flux. This could be due to poor simulation of the stable boundary layer and PBL transitions.

VPD (Figure 2.4, middle) is simulated quite well in CONTROL and IMPACT (0.25 and 0.5 hPa), implying a good simulation of evaporative demand. How this actually relates to diurnal stomatal resistances and evapotranspiration is not clear though. Under constant light and VPD, the stomatal aperture of Jojoba is controlled by the xylem water potential of the plant. This response is heavily dependent on soil and air temperatures and is therefore highly non-linear (Benzioni and Dunstone, 1988).

U - is well simulated in both simulations (Figure 2.4, bottom), but variability is overestimated by IMPACT and underestimated by CONTROL. A possible source of variance bias could be due to local complexities in the turbulent wind field due to the semi-open canopy.

R_N - is well modelled by CONTROL and IMPACT over the day (Figure 2.5, top), which is significant for modelling the available energy, but does not necessarily account for compensatory biases in specific radiation components. There is a slight underestimation for both cases around peak time (14.00 LT) of 30 - 50 W m^{-2} . This can be explained by a simulated atmosphere which is too dry, with reduced down welling long wave. This was investigated and a long wave deficit exists, which accounts for nearly all of the R_N bias. This represents only a small fraction of the R_N magnitude though, so it should not compromise energy balance estimates significantly.

Q_G - is overestimated by around 30 W m^{-2} in CONTROL, but not by IMPACT (Figure 2.5, middle). In both cases the morning upward slope is too sharp in the model, especially in CONTROL. This could indicate: a) a too large temperature gradient between skin and soil, b) mis-parameterized thermal conductivity, dependent on η (Chen and Dudhia, 2001), or c) misclassified soil texture/characteristics. Measurement of Q_G is always difficult because of surface heterogeneity and sharp gradients, but the high correlation between the

two flux plates used (0.99) more or less rules out any error due to spatial heterogeneity between the plates.

ST_{5cm} - values reflect the night time T_{2m} cold bias (Figure 2.5, bottom). However, the bias is strongest in CONTROL. This can be partially explained by the greater upward Q_G in CONTROL (20 W m^{-2}) than in the plantation ($10 - 12 \text{ W m}^{-2}$). During the daytime the model converges again with the observations. This can be explained by the steeper model slope which allows the model to reduce the deficit somewhat.

Q_E - the model matches closely with the observations, and lies within 20 W m^{-2} of both curves at peak time (Figure 2.6, left). Both the shape and the magnitude of IMPACT lies in the middle of Penman Ra/Rs and Penman 56 FAO, but the shape is more similar to the latter.

Extrapolating IMPACT Q_E to Q_H , yields a peak surplus of around $120 - 130 \text{ W m}^{-2}$ (Figure 2.6, right) over IMPACT compared to CONTROL.

2.6 Summary of results

The principle aim of this experiment, was to parameterize WRF-NOAH, so as to reproduce realistic fluxes, and other quantities over desert and plantation surfaces.

For all directly measured quantities the model simulates both surfaces well, in terms of magnitude and variability (Figure 2.4 and 2.5). The vegetated surface tends to exhibit slightly higher deviations than the desert surface though, but these do not appear so significant as to invalidate further impact studies. For the calculated fluxes, WRF simulates Q_E to a maximum deviation of around 12 W m^{-2} at the peak (PM FAO 56 curve), and closer during other hours of the day (Figure 2.6, left). The diurnal evolution of Q_E is also well simulated, shape of the curve. Estimates of Q_H (right), based on the energy balance residual, are closely matched (to within a 10% deviation) at the time of max Q_H . IMPACT T_{2m} is $\sim 1.5^\circ\text{C}$ too cool which may have some significance for CBL heating, however it is not completely clear why this is so.

Weaknesses in the model are a large night time T_{2m} cold bias and an over-estimation of Q_G , especially in desert. Not unexpectedly, this cold T_{2m} bias is reflected by a corresponding night time ST_{5cm} cold bias. Over the desert and vegetation, the night time T_{2m} cold bias gap is very quickly closed after the morning transition to a CBL although more quickly over the desert. Ultimately, our focus remains on daytime CBL processes, and the night time cold biases do not seem to significantly bias the CBL so the night time bias will not be dwelled upon too heavily here. For the Q_G bias, parameterization of soil thermal transport needs to be improved, especially in bare soils. The contribution to the peak energy balance is not large in the plantation (5 - 6 % of R_N), but it is more significant in the desert (20% of R_N).

Assuming an insignificant desert Q_E (confirmed by observations), and that the Q_G measurement error is not high, the implication is that WRF underestimates the desert Q_H by around 30 W m^{-2} at peak time. It seems that the soil thermal conductivity/diffusivity parameters may need further adjustment in NOAH, for local soils.

Generally, Q_E seems to be well simulated, when compared to Penman Monteith estimates and the peak value of 160 W m^{-2} is therefore a reasonable estimate. In terms of Q_H , we can assume a positive gradient, from the desert to plantation. Gradients of $120 - 130 \text{ W m}^{-2}$ can be expected but this can be reduced to $90 - 100 \text{ W m}^{-2}$, if we assume a 30 W m^{-2} desert Q_G overestimation.

Chapter 3

Applying the model: impact study of arid plantations - Oman and Israel

3.1 Introduction

The goal of this section is to assess the impact of geoengineering scale plantations on PBL evolution and convection, in two regions - Oman and Israel. The plantation was scaled up from the validation experiment, to a 100×100 km square and inserted into the two arid coastal regions of Israel and Oman (Figure 3.1). One reason for keeping a similar plantation shape and size as used in Wulfmeyer et al. (2014) is to maintain an element of comparison, but with the new validated model configuration and new irrigation scheme. Additionally, a dual analysis of the arid regions, Oman and Israel is useful to investigate the effect of prevailing conditions on observed phenomena. In this chapter a description of the model domains and execution is presented along with details of the inserted plantations (Section 3.2). In Sections 3.3.1 to 3.3.3 the results of all analyses are presented, followed by a summary of results.

3.2 Methodology - Model domains, duration and spin-up

For the impact study, the model configuration was kept consistent with Chapter 2, including plant parameters and physics schemes. In Wulfmeyer et al. (2014), Oman and the Sonoran Desert, Mexico were simulated and compared. Here, a new arid region was considered (Israel, instead of Mexico), whilst at the same time keeping one common region to enable an element of comparison (Oman). Two model domains were chosen for the impact study keeping the number and arrangement of vertical levels the same as the validation runs (92), and the horizontal grid increment (2 km). However, the dimensions of the domains were reduced from 444×444 grid cells to 200×200 . Informal comparisons yielded only very minor differences in pressure, T_{2m} and q_v fields, between these domain

configurations, so this is a reasonable compromise. In addition to greatly reducing resource use, this also means that the lateral boundary forcings are shifted closer to the plantation whilst still allowing a reasonable spatial margin for WRF to develop its own weather systems (~ 50 km from boundaries to plantation).

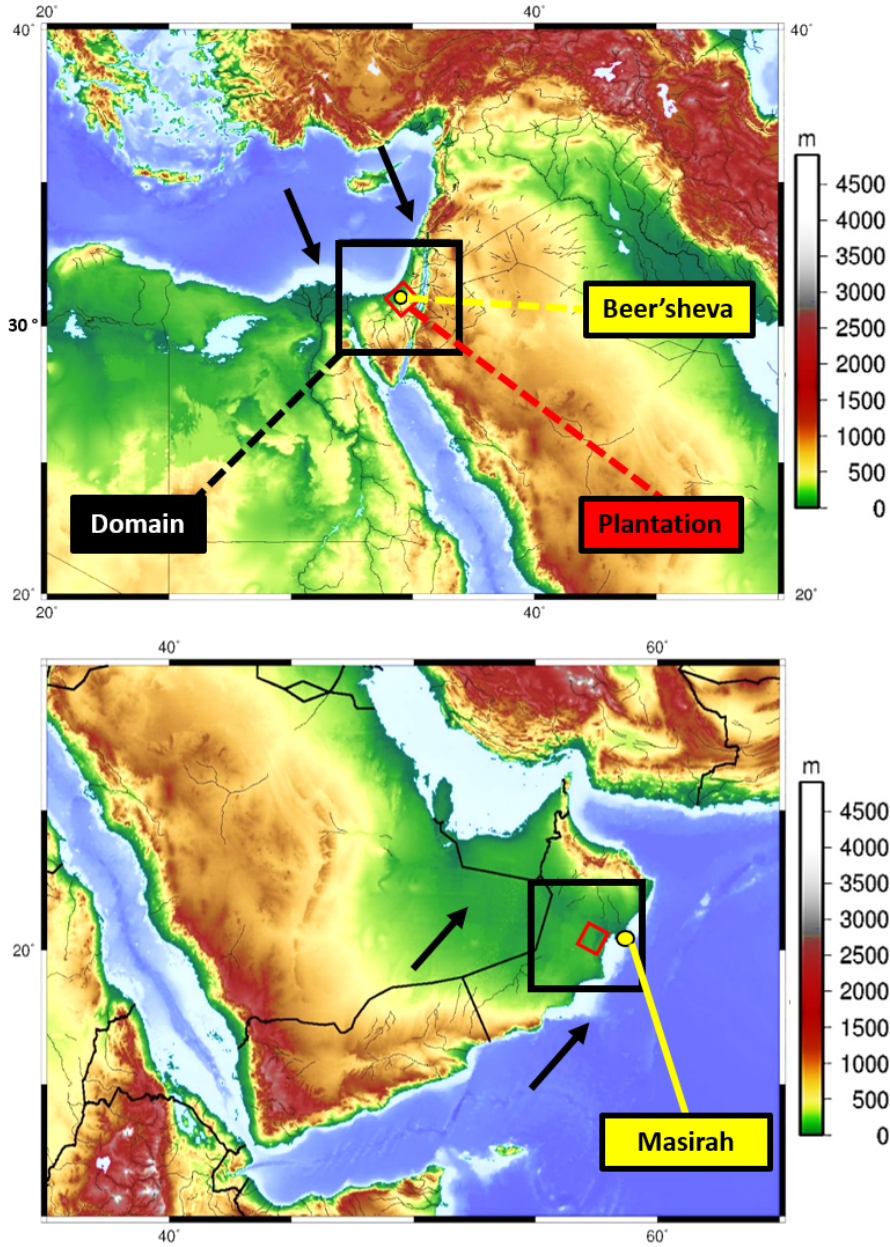


Figure 3.1: Model domains marked on topographic maps of eastern Mediterranean and Arabian peninsula regions. Model domain extents are marked with a black polygon and the 100×100 km plantations are marked as red polygons. Mean summer wind flow is marked with black arrows. The Oman domain is centered at 20.30° N, 57.58° E and Israel at 31.25° N, 34.50° E. The Oman domain is located 3.2° below the Tropic of Cancer ($23^\circ.50$ N), whilst Israel lies 7.75° above it. Both domains are 200×200 km in dimension with 2 km horizontal grid spacing. The yellow dots represent the city of Beer'sheva, Israel (top) and Masirah Island in Oman (bottom).

The Israel domain (Figure 3.1) is centered at the eastern end of the Mediterranean at 31.25°N, 34.50°E, reaching up to the Lebanon in the north, down to the lower Sinai peninsula in the south, most of Jordan in the east and over to mainland Egypt in the west. The Oman domain on the Arabian peninsula is centred at 20.30°N, 57.58°E and reaches from close to the north coast of Oman at the top end to middle-Oman in the south, and from Masirah Island in the east over to Saudi Arabia in the west. The Oman domain centre is therefore located within the tropics, 3.2° below the Tropic of Cancer (23°.50N), whilst Israel lies 7.75° above it, within the subtropics. For each region two scenarios were executed as before - CONTROL and IMPACT. The upscaled plantations were rotated so that two of the sides were parallel to the large-scale mean surface wind flow (approximately NNW for Israel and SSW for Oman). This orientation also brings one side close to, and approximately parallel with the coastline. It is not yet clear what influence this orientation may have on resulting land surface/atmosphere feedbacks, but it should maximize the flow of humid marine air over the plantation. In Oman the orography is mostly of low relief (below 200 m), so limited orographic effects are expected. In Israel there is some difference between the windward and leeside of the plantation, with the terrain rising from 0-100 m in Gaza to 500 m at the plantation leeside (visible in Figure 3.1 and also 2.1).

The model was run with ECMWF analysis data as before, from the 10.06 to 31.07 (2012) with a spin-up period of 14 days (10.06 to 23.06), which was then disregarded for analysis. The 38 day period of 24.06.2012 to 31.07.2012 remains for the analyses.

3.3 Results and discussion - Impacts, processes, precursors

3.3.1 Precipitation

Since one of the main goals is to investigate impacts on moist convection, the convective precipitation fields were examined first. The total accumulated precipitation differences (IMPACT minus CONTROL) are plotted in Figure 3.2 (for the 38 day period of 24.06 to 31.07). The first notable observation is that there is a precipitation impact - significant in Oman, but slight in Israel. In Israel, the spatially averaged domain increase (IMPACT minus CONTROL) is only 0.019 mm (3.13 Pg total mass [$\text{Pg}=1 \times 10^{12}$ kg]). In Oman, the increase is 0.37 mm (59.94 Pg). If we consider only the footprint of the plantations these same differences are - Israel, 0.13 mm (1.34 Pg) and Oman 4.29 mm (42.95 Pg). In Israel, there are no patches over the plantation with values >1.5 mm and are on the verge of being considered insignificant. Since we want to highlight only clear convective impacts, a lower threshold of 1 mm was imposed, as used by Frei (2003) and also Peterson et al. (2001), to delineate whether significant precipitation occurred within a grid cell or not. Such a method removes spurious values due to random (model drizzle) or systematic error but can significantly affect the appearance of spatial plots.

Downstream from the Israel plantation there is a small but significant impact of 3.5 - 4 mm, which could indicate a small wake or leeside effect. This could also be caused by the 500 m rise in orography. However, the plantation is still the defining difference between IMPACT and CONTROL. Figure 1.2 indicates that virtually zero precipitation falls in June/July in Beer'sheva, so even 4 mm may be considered a significant amount.

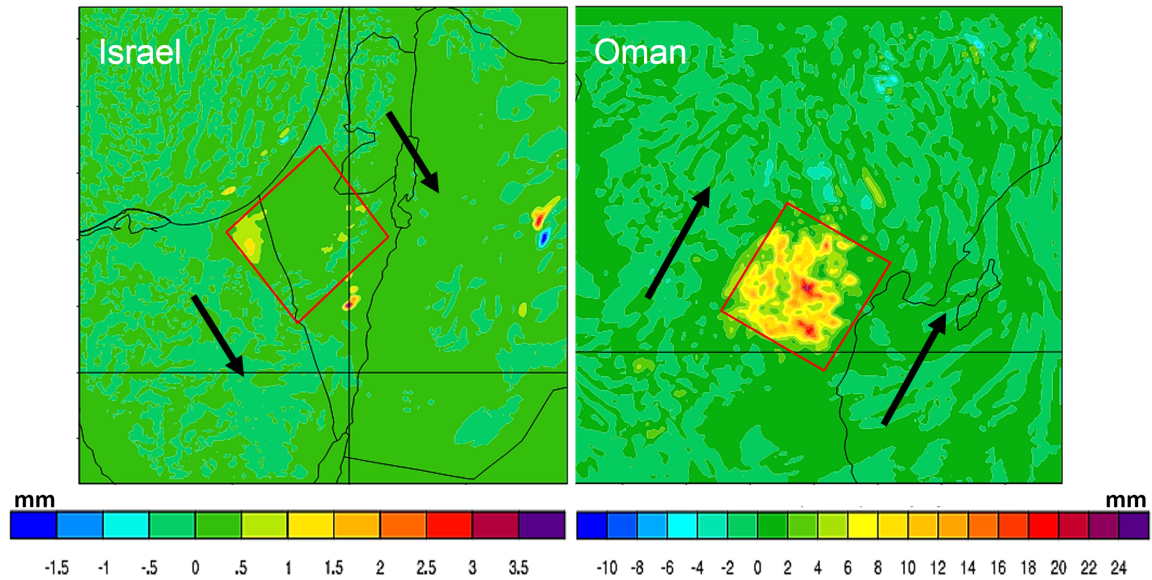


Figure 3.2: Total accumulated precipitation difference over Israel and Oman (24.06 to 31.07 2012) - IMPACT minus CONTROL. The red frame denotes the plantation boundary in IMPACT. Note the difference in scales due to the large differences in regional impacts. Also marked are arrows approximating the summer mean surface wind flow.

In Oman, nearly all of the increase in rain occurs over the plantation footprint indicating a very clear impact, with some areas close to the center with a 24 mm surplus. From Figure 1.2 in Chapter 1, we know that in Masirah a mean of 21 mm month⁻¹ falls in June and 11 mm month⁻¹ in July, so 24 mm represents a significant amount over 38 days especially in drier inland locations.

Next, the daily precipitation quantities are plotted for both regions and both scenarios, in Figures 3.3 and 3.4, considering two spatial averaging zones: 1) the plantation footprint (left panels) and 2) the whole domain (right panels). Two statistics are shown - the maximum or max rain rate [mm d⁻¹] (top panels) and the areal mass [Pg d⁻¹] (bottom panels). Note that the scales do not match for Oman and Israel, but need to be plotted this way to maintain visual clarity for Israel. In Oman, CI occurs almost exclusively between 09.00 and 11.00 UTC (LT=UTC+4) and in Israel 13.00 and 15.00 UTC (LT=UTC+2).

One reason for considering both zones is because impacts, related to the plantation may occur outside its boundaries, as seen in Israel (Figure 3.2). Another is related to the significance of background atmospheric conditions. In Oman, two clear 'wet' periods are apparent, where moist convection tends to occur (in CONTROL or IMPACT, or both), and

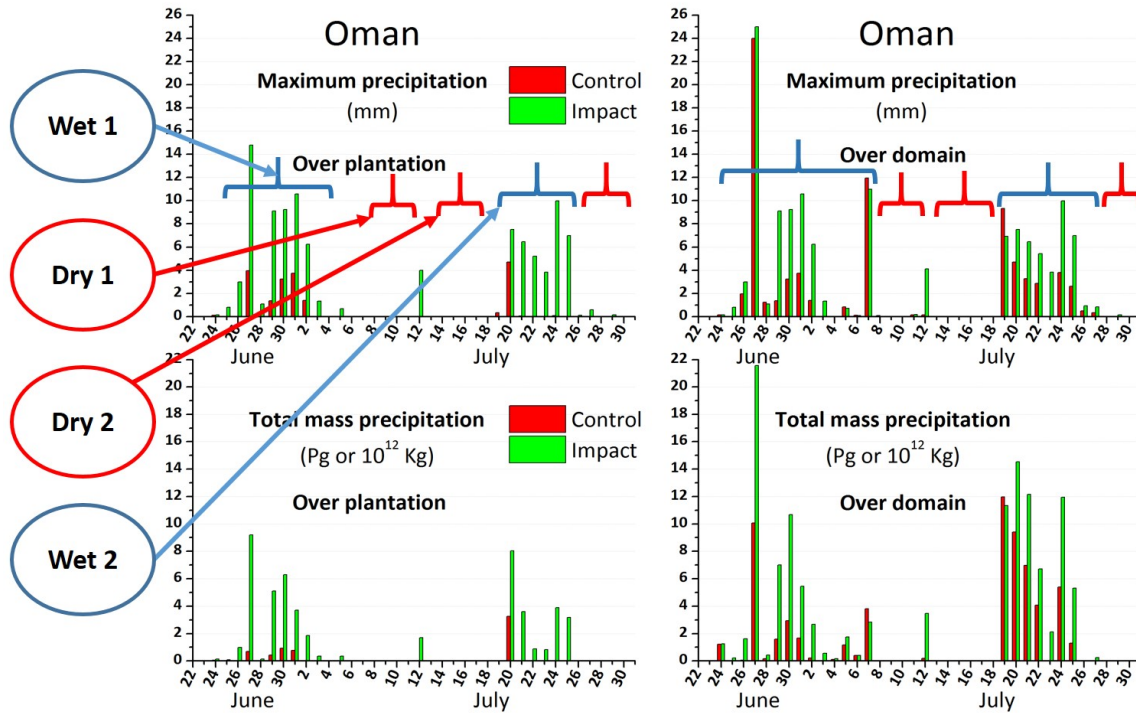


Figure 3.3: Oman - daily precipitation over plantation (left) and domain (right) for 24-06 to 31.07 2012, with daily maximum (top) in mm d^{-1} , and daily precipitated mass (bottom), in Pg (10^{12} kg) Also indicated are wet and dry periods when ‘no rain’ or ‘rain’ occurs over both areas (far left).

three short ‘dry’ periods, where almost no rainfall occurred in CONTROL or IMPACT. In Israel, almost the whole period is dry over both zones (below 1 mm), apart from a few days at the end of July where extremely limited convection occurred. Investigating the influence of atmospheric conditions on impacts could be very instructive in process understanding, and so the whole period was split into distinct ‘wet’ and ‘dry’ periods. In this way, common factors or features can be examined (later in Section 3.3.3.- Precursors). Care needs to be taken whilst grouping the days together, to avoid misclassification. For instance, selection of wet/dry periods depends heavily on which zone is considered, as indicated by the red and blue brackets in Figure 3.3 (top panels). To avoid any such problems, days are only considered ‘wet’ if an event is apparent for both domain and plantation zones (and vice versa for ‘dry’). This means that certain days are disregarded, where the status is not really clear. Additionally if CI occurred only very remotely from the plantation, its significance was disregarded. This selection process was more difficult for Israel because the tiny amount of rainfall that did occur, fell outside the plantation anyway. Wet/dry periods for Oman and Israel are shown in Table 3.1. Note that the very last dry period for Oman (Figure 3.3) was disregarded as surplus to requirements.

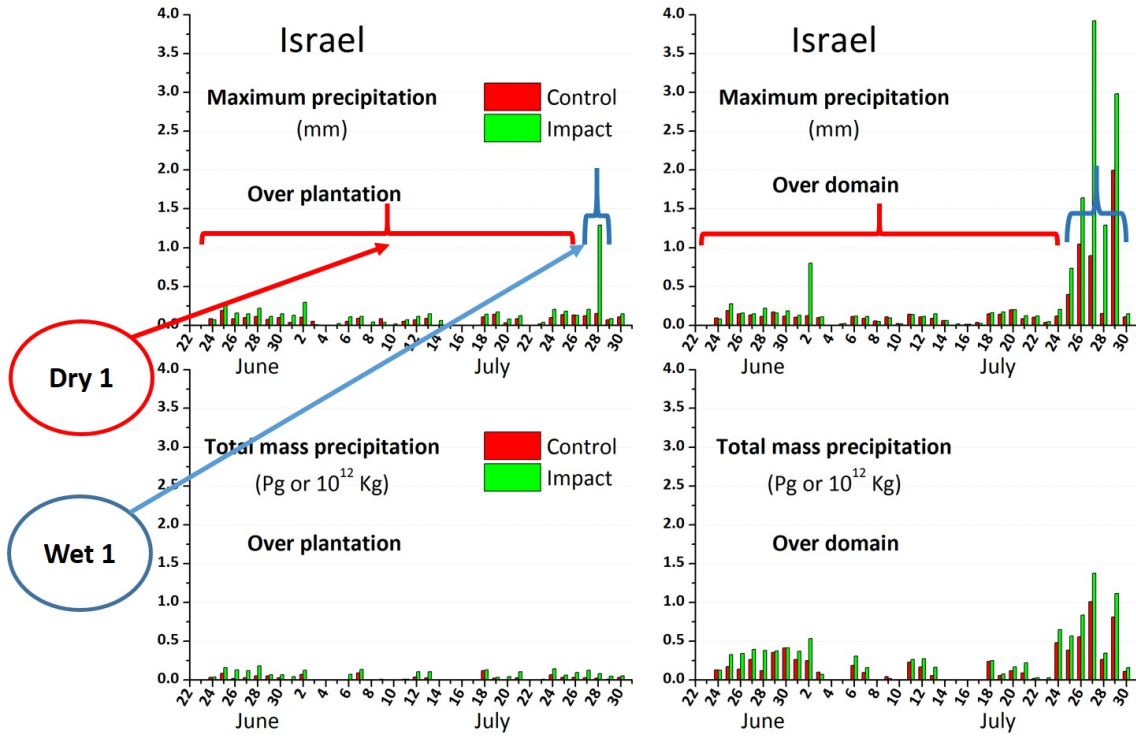


Figure 3.4: Israel - daily precipitation over plantation (left) and domain (right) for 24-06 to 31.07 2012, with daily maximum (top) in mm d^{-1} , and daily precipitated mass (bottom), in Pg (10^{12} kg) Also indicated are wet and dry periods when ‘no rain’ or ‘rain’ occurs over both areas (far left). Note the reduced scale for the Y-axes.

Table 3.1: Classified wet and dry periods, in chronological order, based on location of rainfall, and a 1 mm minimum threshold.

Region	Period	Dates
Oman	Wet 1	26.06 - 2.07
	Dry 1	08.07 - 11.07
	Dry 2	13.07 - 18.07
	Wet 2	20.07 - 25.07
Israel	Dry 1	24.06 - 26.07
	Wet 1	27.07 - 29.07

Following that, all events (and non-events) in Oman were classified based on the nature and strength of the event using the following classifications: ‘enhanced’, ‘induced’, ‘not induced’, or ‘reduced’ (Figure 3.7). The reason for doing so is to allow for the analysis of the prevailing conditions, in CONTROL, for these event types. This could well give us some interesting insights into potential thresholds/pre-requisites for CI (see also Section 3.3.3). As an example of these event types, see Figure 3.5. On some days in Oman, detectable rainfall occurred in CONTROL, but this amount was ‘enhanced’ (left and center panels) to some degree by IMPACT over the plantation. On other days, no precipitation occurred in

CONTROL, but was ‘induced’ by IMPACT (right panels). Occasionally rainfall amounts in CONTROL were ‘reduced’ in IMPACT (or perhaps displaced). During the remaining ‘not induced’ days, no convection of any kind occurred either in CONTROL or IMPACT. In Figure 3.5, the main rainfall impacts are located in different positions around the plantation but noticeably closer to the windward side and also the coast on the ‘enhanced days’ and the ‘induced’ rain falls in the northern corner which is on the leeside of the plantation.

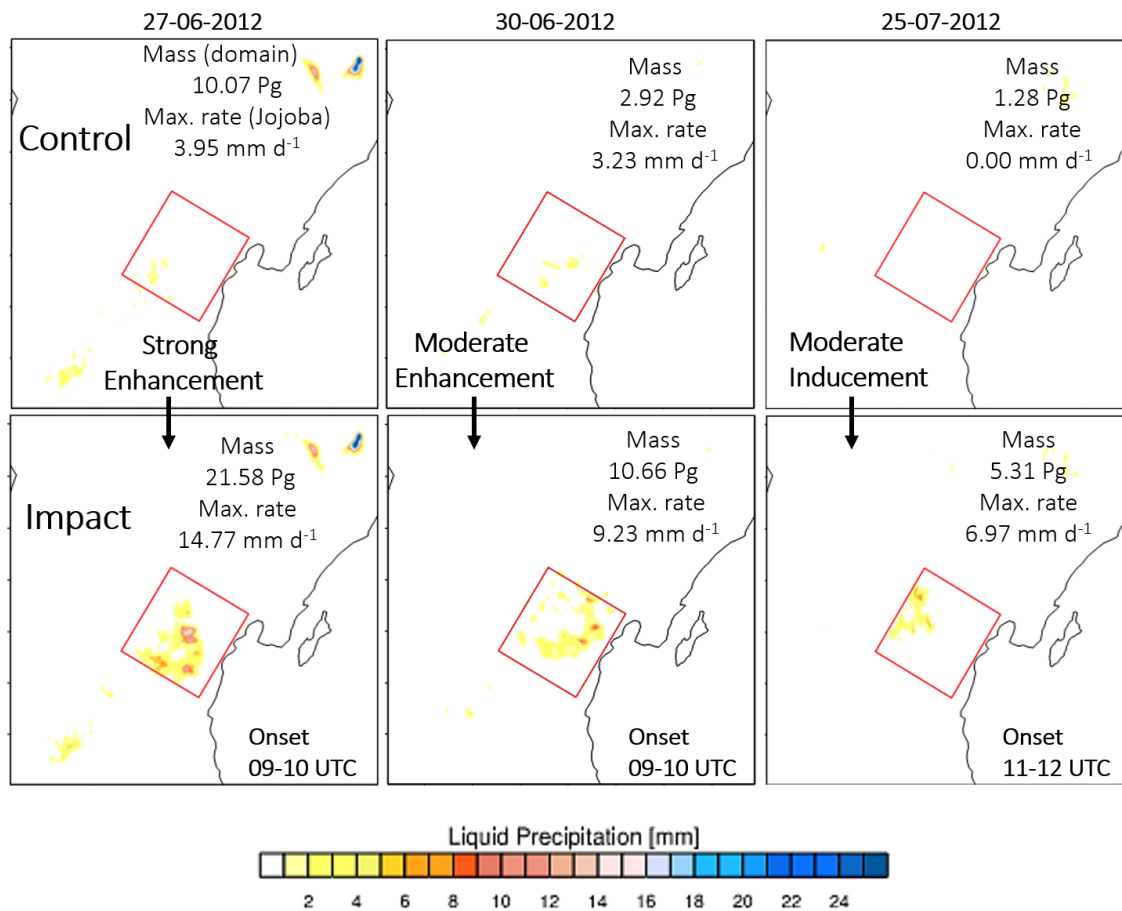


Figure 3.5: Oman - classification of impacts, showing domain precipitation mass (Pg [10^{12} kg]) and daily maximum (top) in mm d^{-1} for CONTROL (top) and IMPACT (bottom). Onset times are also indicated. Enhancement signifies some rainfall in CONTROL, but significantly enhanced in IMPACT. Inducement means no rain in CONTROL but occurs in IMPACT.

In Israel, two consecutive days exist (26.07 and 27.07) where a very small amount of rain was ‘induced’ to the south of the plantation (Figure 3.6) and the rest of the days are ‘Not induced’.

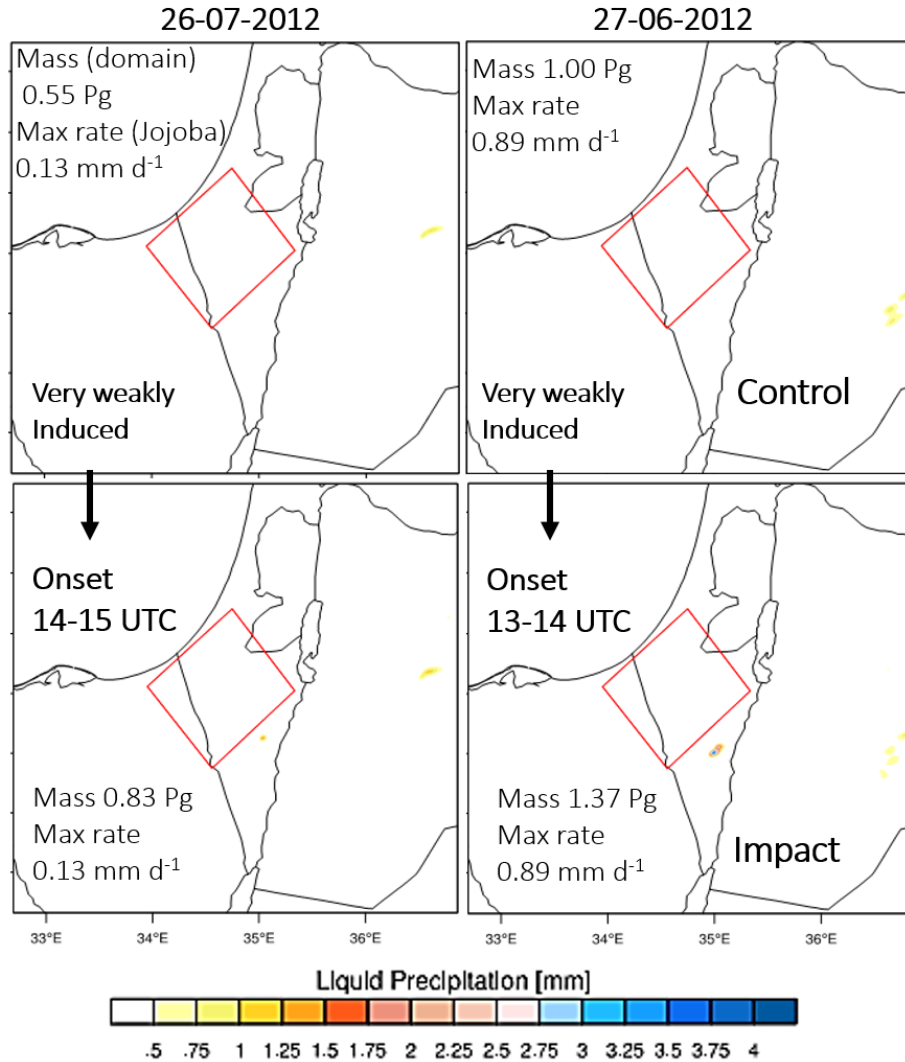


Figure 3.6: Israel - classification of impacts, showing domain precipitation mass (Pg [10^{12} kg]) and daily maximum (top) in mm d^{-1} for CONTROL (top) and IMPACT (bottom). Onset times are also indicated. Note the reduced scale from Fig. 3.5.

A count of the event types is shown in Figure 3.7 for Oman (Israel is not considered due to the lack of significant events). If we consider only the plantation zone in Oman, there are 11 induced days and 2 enhanced days, indicating a clear impact over the plantation and an ability to increase rainfall when conditions for CI are favorable. If we consider the whole domain, the situation is reversed with 11 enhanced days and 4 induced days. This reflects that rainfall events did occur in CONTROL on some days but these amounts were significantly increased over the plantation.

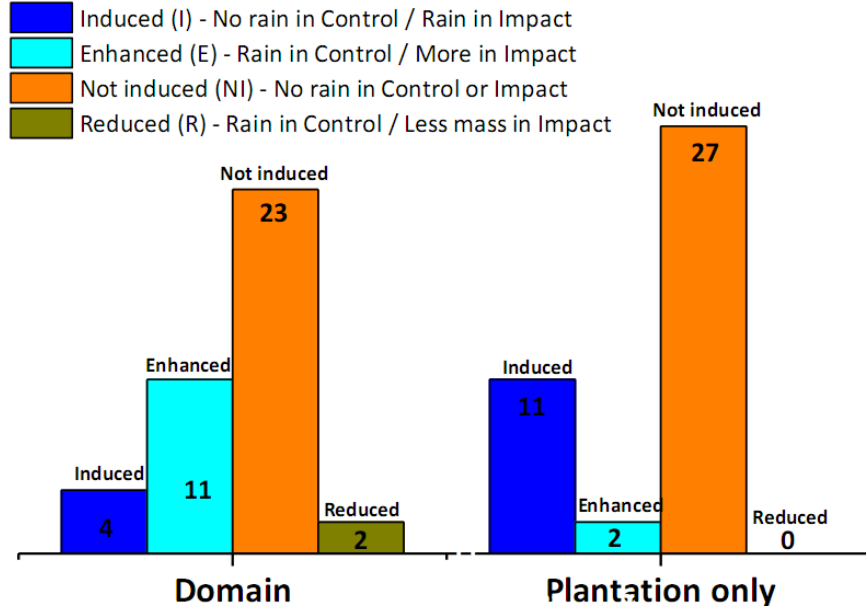


Figure 3.7: Oman - impact frequency. Number of days where precipitation is induced, enhanced, not induced, or reduced within domain or over plantation only [24.06 to 31.08].

3.3.2 Processes in convection initiation

This section focuses on the processes occurring during a convective event on the 30.06, Oman (Israel is not considered due to the lack of significant events). On this day, CBL impacts led to a strong precipitation enhancement effect (from Figure 3.5). Before looking at the observed processes, it is instructive to examine expectations of impacts within the context of a differential heating perturbation.

Buoyancy generation

Over the plantation, Q_E is constrained by the irrigation level (η) (via NOAH’s stability-adjusted Penman-Monteith method (Chen and Dudhia, 2001)). The Q_H surplus of 120 - 130 $W m^{-2}$ (see Chapter 2) leads to a differential CBL heating (See Appendix 6.3 Figure 6.6 for spatial plots of Q_H and Q_E based on Chapter 2). This heating perturbation increases the buoyancy contribution ($\frac{g}{\theta} \overline{w'\theta'}$) to TKE (Equation 1.1) and can potentially lead to mean convergent ascent through a pressure perturbation.

Pressure perturbation and convergence - 30.06

From column heating expansion, we expect a surface-low to develop corresponding with a high pressure perturbation aloft. Segal and Arritt (1992) describe a pressure perturbation (Π') scale function, to estimate the pressure perturbation (P') for a given temperature perturbation (T'), $\Pi' \times$ ambient pressure. An initial surface θ stratification $\Phi_0 = \partial\theta_0/\partial z$

is assumed to develop over an area, which fades into a mixed layer of height h where $\Phi = \partial\theta/\partial z = 0$. Using the Exner function $\Pi = C_p T/\theta$ (Pielke, 2002) the surrounding pressure can then be scaled by:

$$\Pi' = - \int_0^h g \frac{\theta'}{\theta_0^2} dz = \frac{-g\Phi_0 h^2}{2\theta_0^2} \quad (3.1)$$

where h is the mixed layer height [m] and the negative sign on the right indicates the negative pressure perturbation, due to positive heating.

The effect of a T' can be seen in Figure 3.8, by examination of sea level pressures (SLP) and T_{2m} for CONTROL and IMPACT at 09.00 UTC (13.00 LT), just prior to CI. In CONTROL (left) the land/sea low/high pressure differential is apparent, as are the rapid LLCJ winds over the coast. In IMPACT (right) perturbations are apparent in the U,

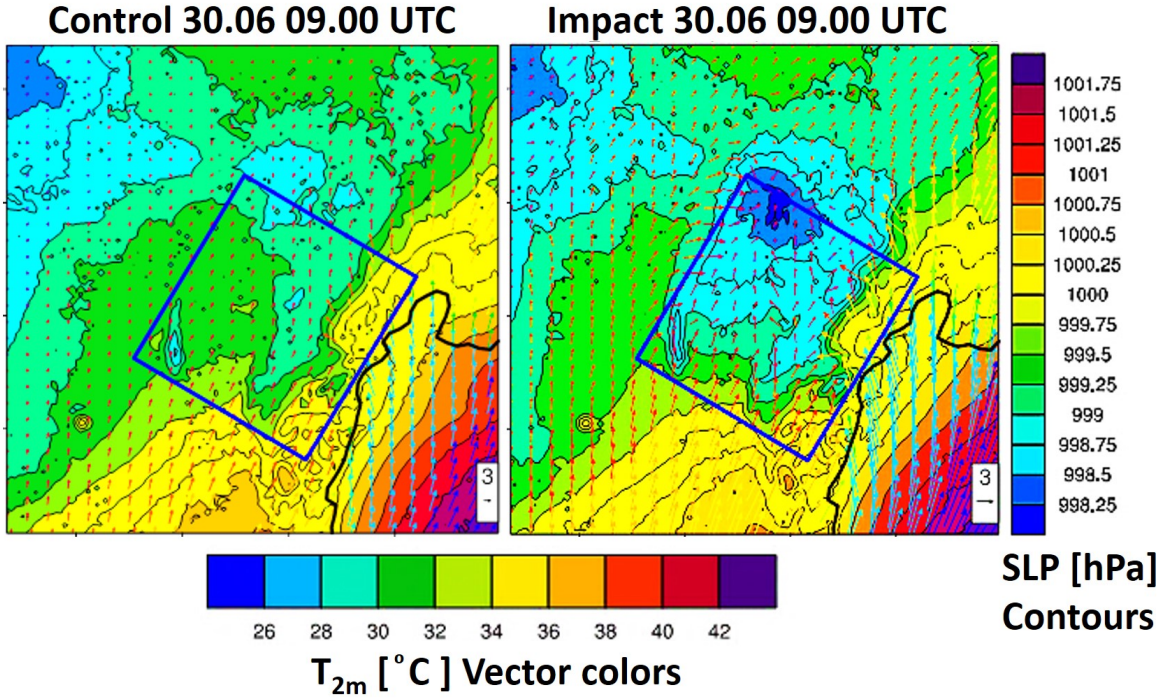


Figure 3.8: Oman - sea level pressures (SLP) over CONTROL (left) and IMPACT (right) for 30.06 at 09.00 UTC just before convection initiation. Filled contours represent SLP [hPa] and U vectors are colored for T_{2m} [$^{\circ}\text{C}$]. Although there is no plantation in CONTROL, the outline is presented to compare with IMPACT.

SLP and T_{2m} fields. A negative P' has developed over the leeward corner which is ~ 0.5 to 1 hPa deeper than CONTROL. T_{2m} values are 1 - 2 $^{\circ}\text{C}$ higher over this area than in CONTROL. Additionally the winds are deflecting towards the pressure low. The winds have also slowed over the plantation as we would expect given the increased roughness. We know that:

$$\frac{d\vec{V}}{dt} = -\frac{1}{\rho}\vec{\nabla}P - f\vec{K} \times \vec{V} - \Psi C_D \left| \vec{V} \right| \vec{V} \quad (3.2)$$

where \vec{V} is the horizontal wind vector, $|\vec{V}|$ is the wind speed, $-\frac{1}{\rho}\nabla P$ is the horizontal pressure gradient force (PGF), ρ is air density [kg m^{-3}], and $-f\vec{K} \times \vec{V}$ is the Coriolis force (becomes negligible at $L \sim \ll 10^4$ m). The last term $-\Psi C_D |\vec{V}| \vec{V}$ is a turbulent drag force term from Taylor (1916), where Ψ is a constant, and C_D is a dimensionless surface drag coefficient, and $|\vec{V}|$ is the wind speed magnitude [m s^{-1}]. In a steady state, these forces are balanced and $\frac{d\vec{V}}{dt} = 0$ can be assumed valid for infinitesimal periods. The angular deviation of the gradient wind (\vec{V}_g) from the geostrophic wind (\vec{V}_G) towards the low pressure is determined by the necessity that the forward component of PGF in the direction of \vec{V}_g , has to be equal to the drag force magnitude. A stronger drag force creates a larger angle, and increasingly sub-geostrophic velocities (Wallace and Hobbs, 2006). Additionally slower wind speeds may increase the strength and maintenance of circulations, as found by Dixon et al. (2013) and Avissar and Schmidt (1998). Horizontal divergence ($\vec{\psi}$) is a time rate change of area [s^{-1}], and is calculated as:

$$\vec{\psi} = \left(\frac{du}{dx} + \frac{dv}{dy} \right) \quad (3.3)$$

and the P tendency (between two heights) is related approximately to $\vec{\psi}$, such that:

$$\frac{dP}{dt} \approx - \int_{p_1}^{p_2} (\vec{\psi}) dP \quad (3.4)$$

Impacts on CBL evolution - 30.06

For the same date (30.06), profiles of potential temperature (θ) and water vapor mixing ratio (q_v) were examined for the three hours leading up to CI: 07.00, 08.00 and 09.00 UTC, and plotted as slices over T_{2m} [K] and 10m wind vectors (\vec{U}_{10m}) (Figure 3.9).

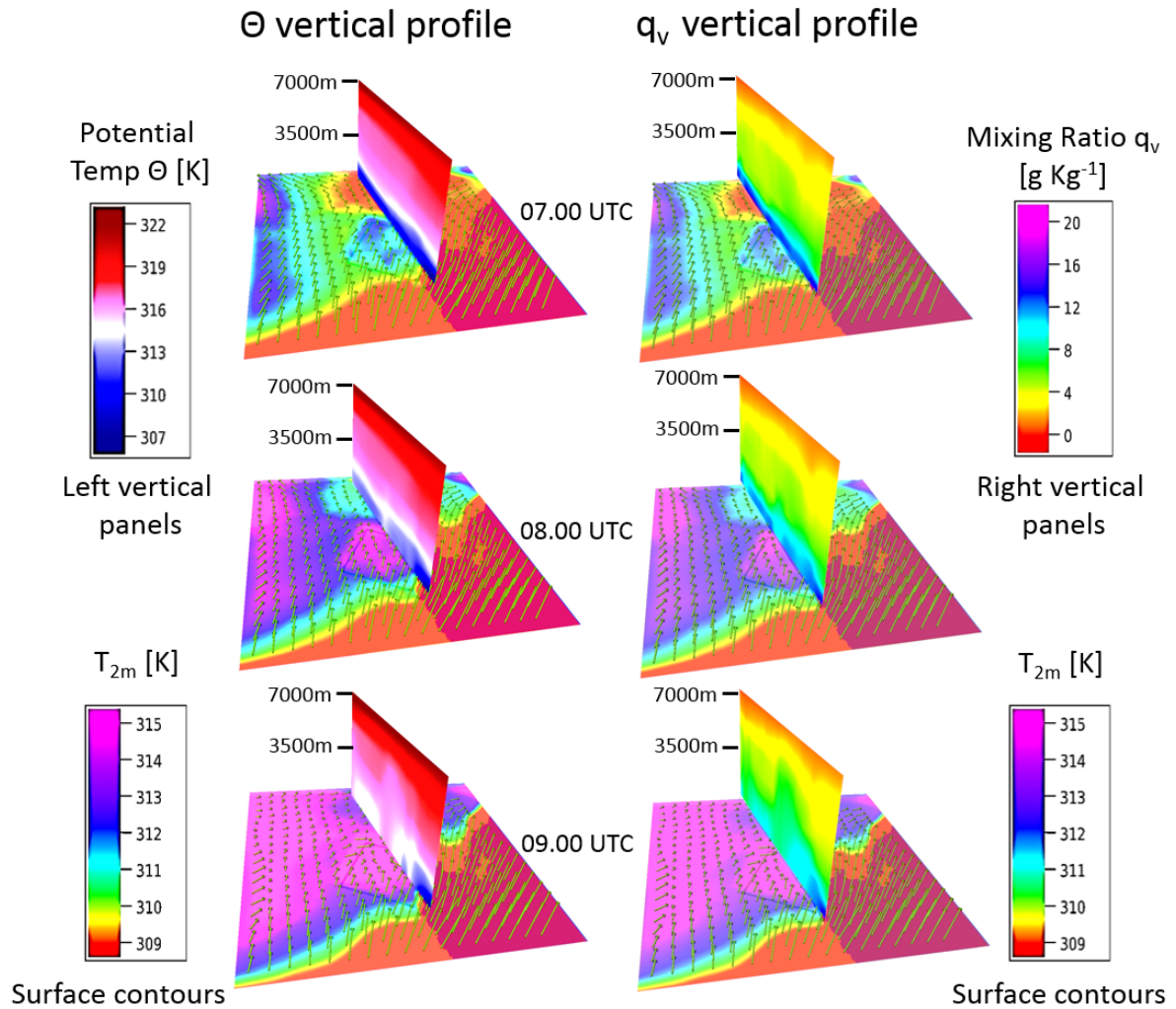


Figure 3.9: Oman - evolution of Θ and q_v profiles (left and right, respectively) in the hours leading up to CI - 7-9 UTC on 30.06. These slices are plotted over horizontal T_{2m} contours and \vec{U}_{10m} horizontal wind vectors (not to scale). The slices, run approximately through the centre of the plantation from north to south.

07.00 UTC - the θ profile is stably stratified over the plantation and there is little mixing, even though T_{2m} is already visibly higher than the surroundings. Decreasing U_{10m} is apparent as it flows from the windward to the leeside, but there are no significant directional changes.

08.00 UTC - increased heating leads and mixing of θ and q_v is evident: $\overline{w'\theta'}$ and $\overline{w'q'_v}$ $>$ 0. This manifests in a de-stratification of the PBL up to \sim 1000 m, and

the forming of an internal boundary layer (IBL). Limited convergence is already visible at the leeside corner where the pressure perturbation is strongest (from Figure 3.8).

09.00 UTC - substantial mixing occurs for θ and q_v up to and beyond 3500 m and the convergence has strengthened.

Vertical motion - 30.06

To examine motions and convective organization further, the vertical wind field w [cm s^{-1}] was plotted for 30.06 at 09.00, 10.00 and 11.00 UTC, in both and horizontal slices (Figure 3.10, overleaf) - 09.00 is just before CI and then 10.00 and 11.00, during. The plots show horizontal cross sections of w at around 1500 m¹ (left panels). A transect was drawn, where strong convective motions were visible. slices were then plotted along the length of this transect (right panels). On the left in Figure 3.10, two distinct effects are marked by (1) and (2) in the top left panel: 1 is the thermally direct pressure perturbation and convergence, and 2 is where cooler, moist coastal winds veer onshore almost daily (See also Figure 3.8). At 2, the coastal winds fan out as they veer onshore, with associated acceleration (as described in Section 1.2.2), but which then decelerate over the plantation. This convergence leads to limited vertical motion along this deceleration line, but behind it the cooler air suppresses buoyancy-induced PBL growth. This effect is particularly apparent at the north-east corner close to the sea, where the cool air incursions are strongest. Suppression is clearly visible in the distribution of accumulated rainfall (Figure 3.2), where there is almost zero in this corner. Coastal jet effects may induce or suppress CI, and are highly relevant to coastal plantations if they are located where LLCJs, orography and irregular coastlines are present. The focus of this study is on the thermal effect occurring at (a), away from the coastline. For more on coastal jets, see e.g. Söderberg and Tjernström (2001); Ranjha et al. (2013) and Parish (2000).

¹ Model level 15 (model level 0 is lowest level)

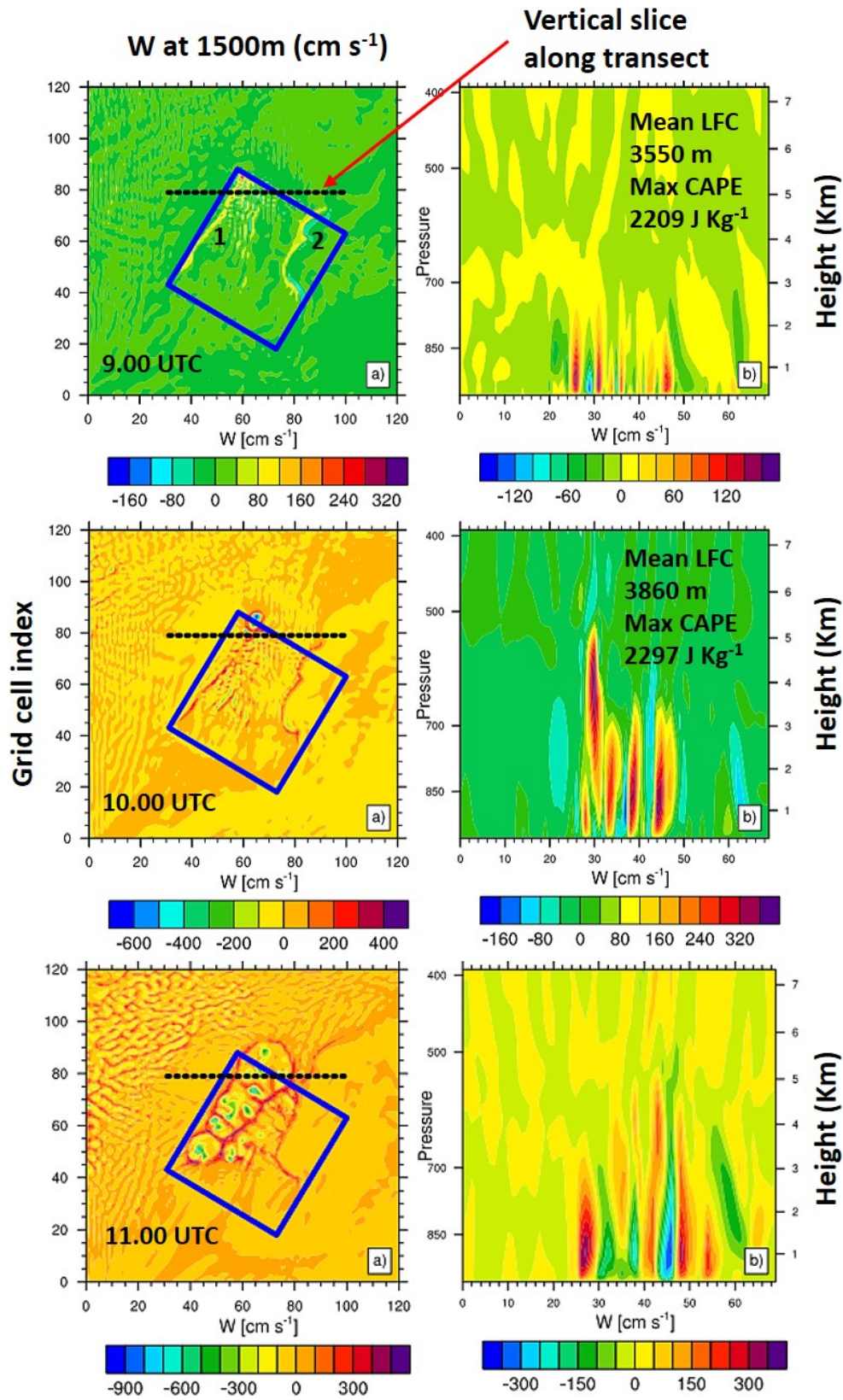


Figure 3.10: Oman - evolution of vertical velocity (w) from before to after CI (9-11 UTC) on 30.06. Left panels (a) show a horizontal slice at roughly 1500m (model level 15) with a transect drawn through an area of convection. The x and y axes denote grid cell indices only. Right panels (b) show slices along this transect with pressure (left y axis) and altitude coordinates (right y axis). The x axis shows grid cell indices only. Note the different contour scales, where the scale extent indicates the maximum up- and downdrafts in each plot.

09.00 UTC - some strong motion begins at the northern corner of the plantation (top left) with updrafts of up to 300 cm s^{-1} . Some organisation is apparent with w forming into horizontal convective rolls or HCRs, spaced on the order of 5 km apart. On the right, a maximum transect CAPE of 2200 J kg^{-1} is present and updrafts with velocities of 140 cm s^{-1} form as far up as 2 - 2.5 km. At this point, these updrafts remain below the transect mean LFC of 3550 m. Limited downdrafts of similar velocity start to appear.

10.00 UTC - just after cloud formation and precipitation have started, we see increasing updraft and downdraft velocities (400 cm s^{-1} and 600 cm s^{-1} , respectively). There is further organisation, with the lateral size of the bands becoming larger, and a small cell has developed in the north corner. On the right, strong motions have now reached the mean LFC of 3860 m. Max downdrafts are still only half the speed of updrafts but are becoming more pronounced and extending to higher altitudes.

11.00 UTC - organisation has increased further with elongated hexagonal shaped mesoscale convective cells (MCC) being formed, aligned with the mean wind flow. These MCCs are on L_s scales of between 20 and 40 km. Within each, strong narrow downdrafts reaching up to 900 cm s^{-1} are surrounded by a closed ring of well defined updrafts reaching $500 - 600 \text{ cm s}^{-1}$. On the right we can already see the updrafts beginning to spread out and lose strength from cold pooling in the centre of the cell.

Local constraints on CI

We know that surface heating is the primary mechanism for generating the heat-low (P') which then leads to horizontal convergence, $-\vec{\psi}$. Over the 38 days, there is only limited variance in max perturbation strength (P') either in Oman ($1.14 \text{ hPa} \pm 0.15$) or Israel ($1.12 \text{ hPa} \pm 0.16$). Nevertheless, when P' does deviate strongly from the mean there seems to be at least a first-order effect on CI (Figure 3.11, overleaf).

The first (and strongest) wet period in Oman (period Wet 1 from Table 3.1) has P' values well above the mean (up to 0.5 hPa more on 28.06). Conversely, periods Dry 1 and Dry 2 have P' values, generally below the mean. This linkage is not quite so clear in Wet 2. On some days P' is above the mean, and none are far below it. Less of a link is apparent for Israel, but then, no significant rain events occurred there in any case.

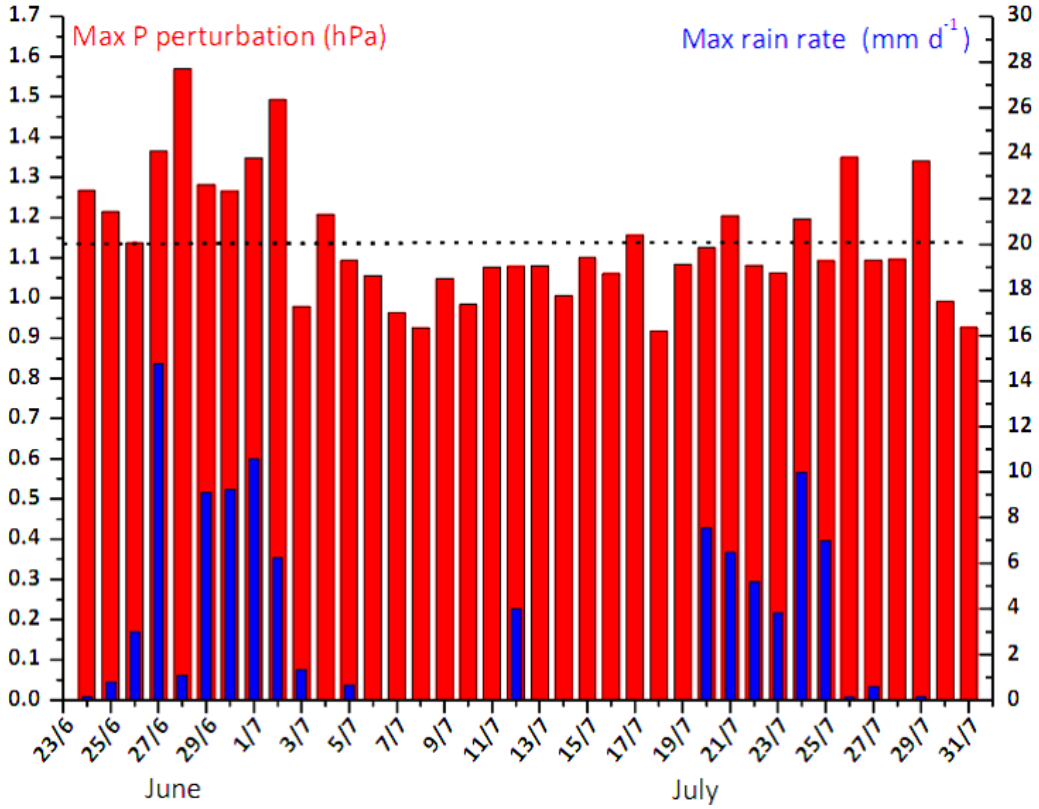


Figure 3.11: Oman - Maximum pressure perturbation P' [hPa] in Impact at 09.00 UTC (red bars, left y-axis), alongside the corresponding maximum plantation rain rate [mm d^{-1}] (blue bars, right y-axis). Also marked is the mean maximum P' for the 38 days (1.14 hPa).

To further examine the association between P' and other important variables such as $\vec{\psi}$, $SW\downarrow$, U and T' , some Pearson correlations (r) were generated over the 38 days in Oman - all at 09.00 UTC (see Figure 3.12, overleaf). There are some significant correlations (at 0.95 confidence). P' is somewhat positively correlated with max $SW\downarrow$ ($r=0.57$), which is as expected given the direct dependence of Q_H on R_N . The variability of the max daily $SW\downarrow$ radiation is low however, both for Oman ($1040.48 \text{ W m}^{-2} \pm 14.46$). Even so, this small variability still has an influence on P' . Furthermore, P' is positively correlated with max IMPACT convergence ($r=0.59$), which is also expected given the relationship in Equation 3.4. P' is positively correlated with T' ($r=0.60$), which relates back to the P scaling function (Π') in Equation 3.1. A very interesting link is the negative correlation between plantation \bar{U} and T' . We expect that increased U generates greater shear turbulence (from Equation 1.1), increasing the mixing of heat throughout the CBL, and reducing T gradients close to the surface. At the same time, this reduction will reduce buoyant generation of turbulence. We can see from Equation 3.1, that P' is proportional both to the initial temperature stratification Φ_0 , and to CBL height, but is inversely proportional to the square of $\bar{\theta}$ over the whole CBL. A lower $\bar{\theta}$ in the mixed layer above the perturbation therefore strengthens P' for a given T' . If the surface stratification is reduced by mixing,

then P' also reduces.

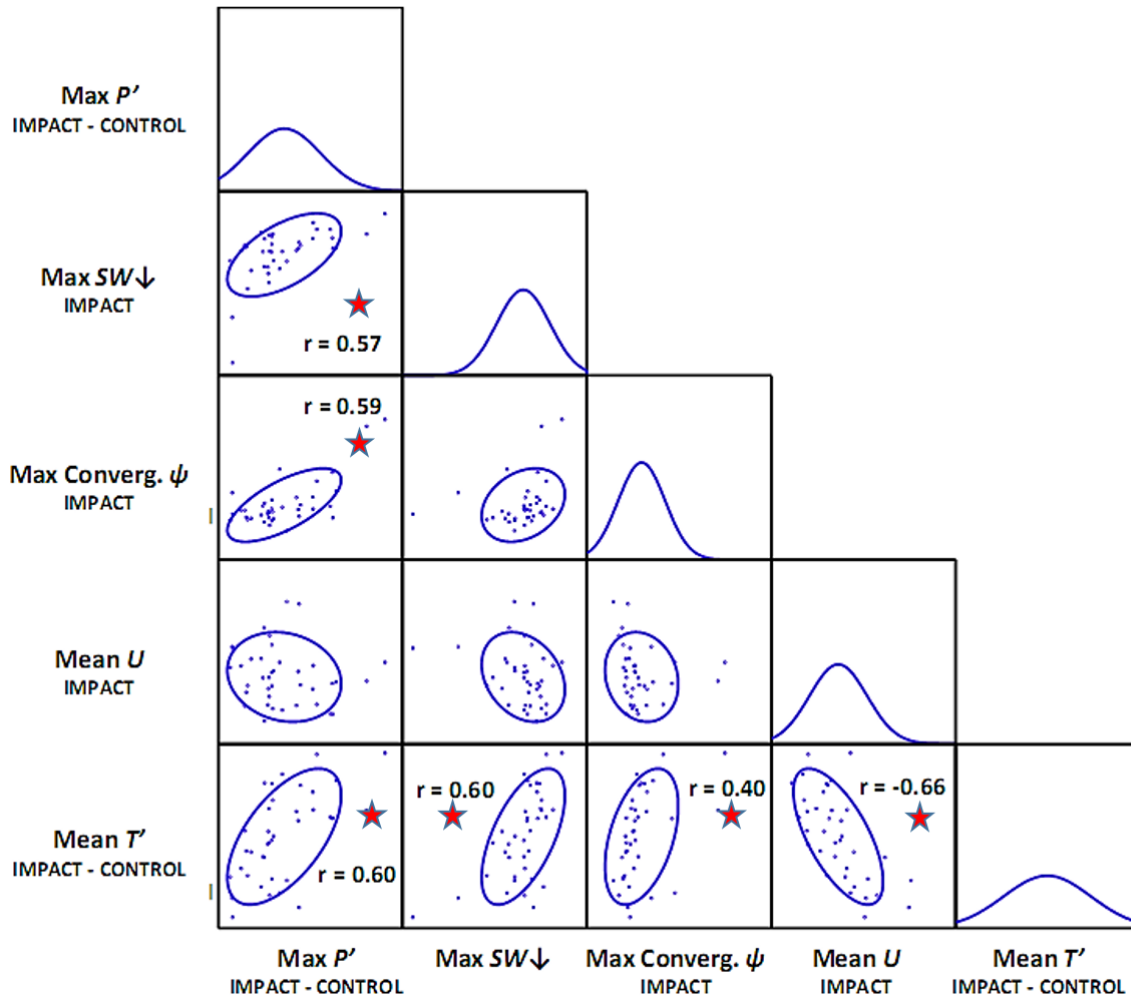


Figure 3.12: Oman (09.00 UTC) - 38 day scatter plots of P' (IMP minus CON), mean surface $SW\downarrow$ (IMP), max convergence ($\bar{\psi}$) at 1st model level (IMP), Mean U (IMP), and T'_{2m} (IMP minus CON). Significant Pearson correlations (r), at the 0.95 confidence level, are marked with a red star along with the correlation strength. All values are taken from within the plantation footprint. Variables U and T' are spatially averaged.

It has been mentioned already in Section 1.5.2, that increased \bar{U} is observed to be detrimental to mean circulations. In fact, if we compare the scatter plot for U and P' , one can discern a slightly negative correlation, but these are not statistically significant for these data. This could be due to a too small sample size ($n=38$) but also due to slightly non-normal distributions.

CBL evolution therefore, as well as the mean wind field may influence the strength of P' . If we compare Israel and Oman, we find that plantation winds are actually weaker in Israel ($5.66 \text{ m s}^{-1} \pm 0.58$) than in Oman ($6.49 \text{ m s}^{-1} \pm 0.72$). Furthermore, typical max $SW\downarrow$ in Israel ($1047.36 \text{ W m}^{-2} \pm 13.42$) is even a little higher than Oman ($1040.48 \text{ W m}^{-2} \pm 14.46$), and we already know that daily P' is very similar in both regions. These facts

do not seem to reflect the aforementioned correlations. We might surmise therefore, that P' can vary day to day through changes in U , $SW\downarrow$ and CBL evolution, and these daily shifts in P' strength directly affect $\vec{\psi}$, to a certain extent ($r=0.59$). If all other factors are equal, a general link between P' and CI seems likely (Figure 3.11). However, we clearly see that in Israel, a similar P' does not have the same impact as in Oman even when other conditions appear similar. It is likely that a certain P' (perhaps $\sim \gtrsim 1$ hPa) is a necessary, but not a sufficient condition for CI to occur. Therefore, there are other constraining factors co-determining the occurrence and strength of thermally-induced CI events. These factors will be addressed in the next section.

3.3.3 Precursors

Here, the background thermodynamic environment, CONTROL, is examined to assess prevailing conditions during wet/dry periods, and on specific days when events occurred. Profiles were examined just prior to usual CI occurrence (09.00 UTC), to see if common factors or characteristics can be associated with specific events. Firstly, Israel and Oman are compared generally in terms of their mean environments. Then common factors separating the 'wet' and 'dry' periods are examined in Oman, where clear differences exist. Finally, some specific days such as 'induced' and 'enhanced' CI events are examined - for Oman and Israel.

Mean background profiles - Oman and Israel

Mean (38 day) thermodynamic profiles of Oman and Israel were plotted on a Skew-T Log-P diagram (Figure 3.13, overleaf) - at 1 hour before typical CI. Variables were averaged over the the plantation footprint (even though it does not exist in CONTROL) to obtain a good representation of the area of interest. Note: the fine detail of a specific sounding, e.g. small inversions may be lost by spatial averaging. Soundings (or rather, single column values) are used later for the specific events.

Significant differences in the virtual (T_v) and dewpoint² (T_d) temperature profiles are immediately apparent. Israel has a similar mean q_v to Oman (10 - 11 g kg⁻¹), but is radically drier above 800 - 850 hPa, with extreme differences around 600 hPa (>4 g kg⁻¹ drier). Israel surface T_v values are cooler than Oman (7 - 8 °C) and lapse rates (Γ) between 850 and 500 hPa are generally much lower than Oman. CAPE is thus minimized in Israel, at this time of year. A relatively low LCL in Israel can be inferred using parcel theory because of higher surface relative humidity (compared to Oman). However, the more stable lapse rate ensures that, if an LFC exists, it is almost unreachable. Besides, this

² T_d is synonymous with q_v depending on the isopleth considered

neglects the fact that an initially buoyant parcel ascending from the surface through a very dry layer will be subject to entrainment of dry air, reducing its buoyancy.

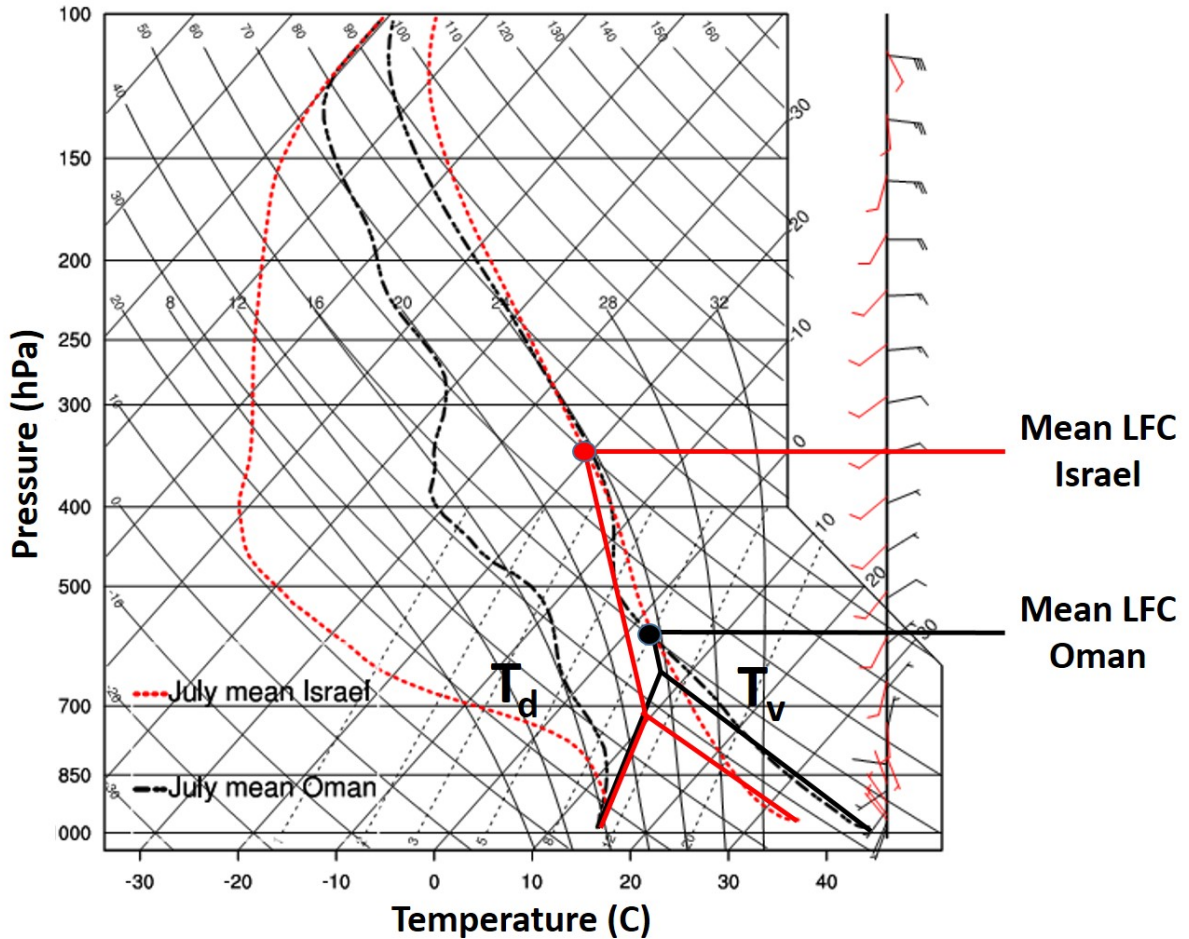


Figure 3.13: Oman and Israel- mean daily profiles of T_v and T_d at 8 UTC-Oman (Black) and 12 UTC-Israel (Red) for 25.06 to 31.07 2012, pre-CI. Values are spatial averages over the plantation footprints. The right dotted curves are virtual temperature (T_v) and the left, dewpoint (T_d). Straight left to right upward sloping dotted lines are constant q_v [g kg^{-1}]. Straight left to right solid lines are constant T [$^{\circ}\text{C}$]. Right to left sloping solid lines are dry adiabats and the almost solid lines are moist adiabats. The thick red and black solid lines are visually estimated LFC heights for each region. Also shown are mean wind barbs with standard velocity scales.

This highlights a limitation of parcel theory and is one reason why w_{max} estimates, calculated as $\sqrt{2CAPE}$, are often gross over-estimations³ (Trapp, 2013). It may be more appropriate when estimating CIN to ‘raise’ a parcel based on the mean q_v of a thicker layer (even the whole PBL), rather than on surface q_v values (Markowski and Richardson, 2010).

Oman in contrast has a more evenly distributed humidity profile from the surface up to 500 hPa where a minimum of around 3 g kg^{-1} is found (Israel $<0.5 \text{ g kg}^{-1}$). Surface

³ Neglect of displacement/perturbation pressure effects is another omission

temperatures are higher and Γ is closer to the dry lapse rate Γ_d ($\sim 9.8 \text{ K km}^{-1}$).⁴ Therefore CAPE is generally optimized in Oman at this time. Winds are similar, except Israel has more directional shear between 850 and 700 hPa. In general, these differences appear consistent with the respective summer climates, Oman remains arid, but with humid air in July, whilst southern Israel is very dry and has virtually no rainfall.

Grouped ‘wet’ and ‘dry’ periods - Oman

Next, all days within wet and dry periods for Oman were grouped together and plotted alongside the 38 day mean (Figure 3.14) [footprint average].

⁴ For brevity, negative lapse rates are not marked with a negative sign. Positive lapse rates are marked with a +

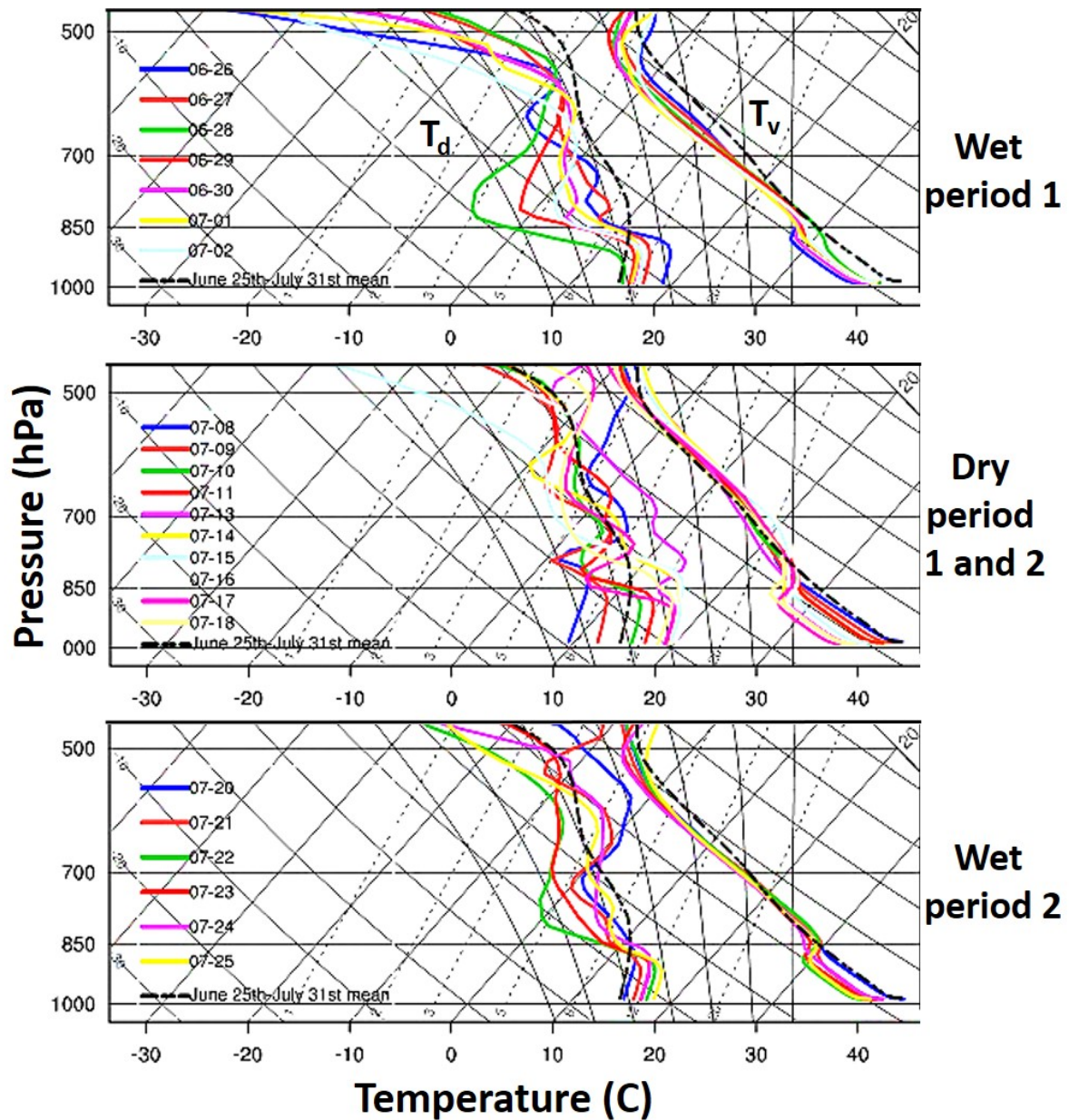


Figure 3.14: Oman grouped T_v and T_d profiles at 08.00 UTC for wet and dry periods to highlight common features. Also shown is the 25-06 to 31-07 mean at 09.00 (black dotted curve).

Some common factors are immediately obvious. The wet periods generally have smaller T_v inversions (~ 850 hPa) than the dry periods, representing lower CIN. Where a larger inversion *is* present in the wet period, CIN is correspondingly reduced by higher surface q_v (e.g. on 26.06). Conversely, where a significant T_v inversion is absent in dry periods, there is usually low surface q_v which raises the LCL (e.g. 08.07). A striking commonality is the T_v lapse rate between 700 and 500 hPa ($\Gamma_{700-500}$) where, almost without exception, days within Wet 1 and 2 periods have slopes greater than the mean, even approaching Γ_d . All days in Dry 1 and 2 have more stable $\Gamma_{700-500}$ slopes which are closer to the mean. The

moisture profiles are less simple to interpret, being more varied and having less common features. This could perhaps be a consequence of averaging over large areas. In the wet periods all days have surface q_v above the mean, whereas the dry periods have some days below and some above the mean. Perhaps surprisingly, on some dry period days there is greater q_v between 800 and 600 hPa than in the wet periods. In these cases, reasons for CI suppression could be a low $\Gamma_{700-500}$, a stronger capping inversion and/or a small P' . This reflects the different pathways by which CIN can be overcome, and convection initiated, heating, increased moisture, and lifting.

Overall, CI seems to require a favorable combination of factors, but a high $\Gamma_{700-500}$ may be the dominant prerequisite. Without exception, all wet period days have a $\Gamma_{700-500}$ approaching 9-10 K km⁻¹ or 'dry-neutral' stability (from Section 1.6). These $\Gamma_{700-500}$ values mean that if parcels gain enough buoyancy to penetrate the CIN layer through heating and persistent convergence, there is enough CAPE to make significant CI more likely.

4 single cases - profiles for CONTROL and IMPACT - Oman/Israel

In this section, individual ‘induced’ and ‘enhanced’ events are examined in terms a) background environment, and b) impact from adding the plantation. Instead of spatial averages, soundings are plotted on Skew-Ts, from a single grid cell at the northernmost corner of the plantation, to obtain finer detail at the location of CI (Figures 3.15, 3.16, 3.17, 3.18).

Oman 27.06 (Figure 3.15) - strongly enhanced Small patches of rainfall occurred along the coast in CONTROL, but this was significantly enhanced by IMPACT (see Figure 3.5, left).

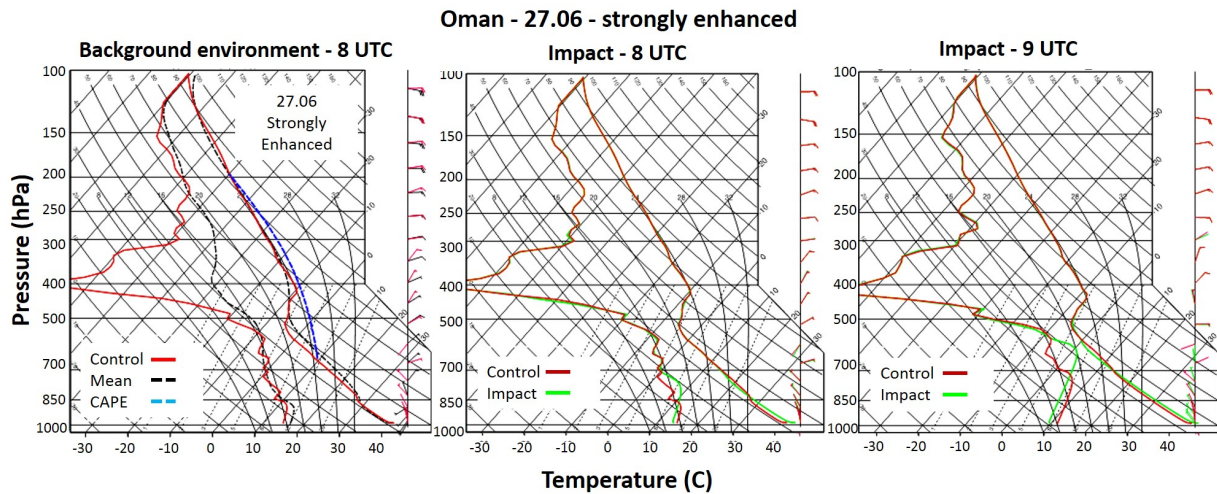


Figure 3.15: Oman - environment and impact 27-06 - strongly enhanced. The left panel shows profiles of T_d (left red) and T_v (right red) from CONTROL at 08.00 UTC along with the 38 day means (black). CAPE is also plotted (blue). The two right panels compare CONTROL and IMPACT (green) at 08.00 and 09.00.

In CONTROL, q_v is evenly distributed up to 500 hPa, with similar values to the mean. In the T_v profile, the inversion is weak at 850 hPa and a high $\Gamma_{700-500}$ ensures the presence of significant CAPE - hence the light existing rain in CONTROL. At 08.00 in IMPACT (centre, green) we can see that IMPACT reduces CIN by atmospheric heating and an increased surface Γ . Some mixing of q_v begins, with upward transport of q_v and downward transport of drier air. At 09.00, q_v at 600 hPa is increased significantly and the remaining CIN is overcome and leading to convection enhancement. This day had the strongest impact of the 38 days in terms of rainfall intensity and also has the highest P' (1.56 hPa).

Oman 30.06 (Figure 3.16) - moderately enhanced In CONTROL, a small amount of rainfall occurs within the plantation boundary, but this is significantly enhanced by IMPACT (Figure 3.5, centre).

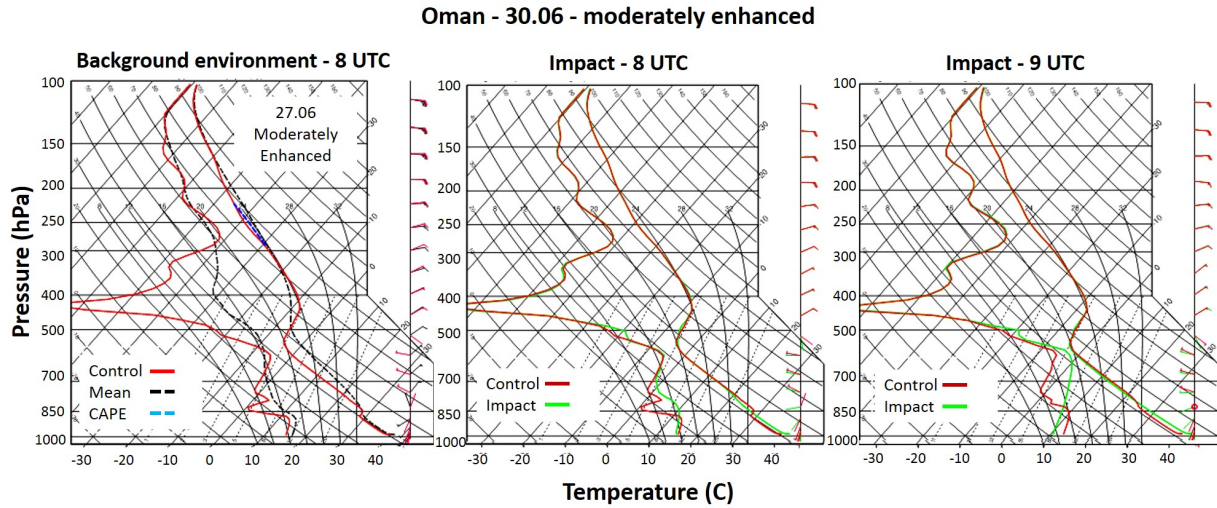


Figure 3.16: Oman environment and impact 30-06 - moderately enhanced. The plot format is as Figure 3.15.

The effect is not quite as strong as the 27.06 though. In CONTROL, surface q_v values are similar to the mean but there is a layer of dry air at 850 - 700 hPa. Furthermore, CIN is a little higher than on the 27.06 and less CAPE is present due to a strong inversion at 500 - 400 hPa which may limit deep convection. At the same time though, $\Gamma_{700-500}$ is very high which greatly increases instability. IMPACT produces similar effects as before, with upward q_v transport at 08.00 moistening the dry layer whilst CIN is broken down. At 09.00 an greater upward q_v transport to 600 hPa occurs than on the 27.06 which could easily be caused by the greater $\Gamma_{700-500}$.

Oman 25.07 (Figure 3.17) - moderately induced No rain occurred in the plantation for CONTROL, but some small spots appear far from the plantation (see Figure 3.5, right).

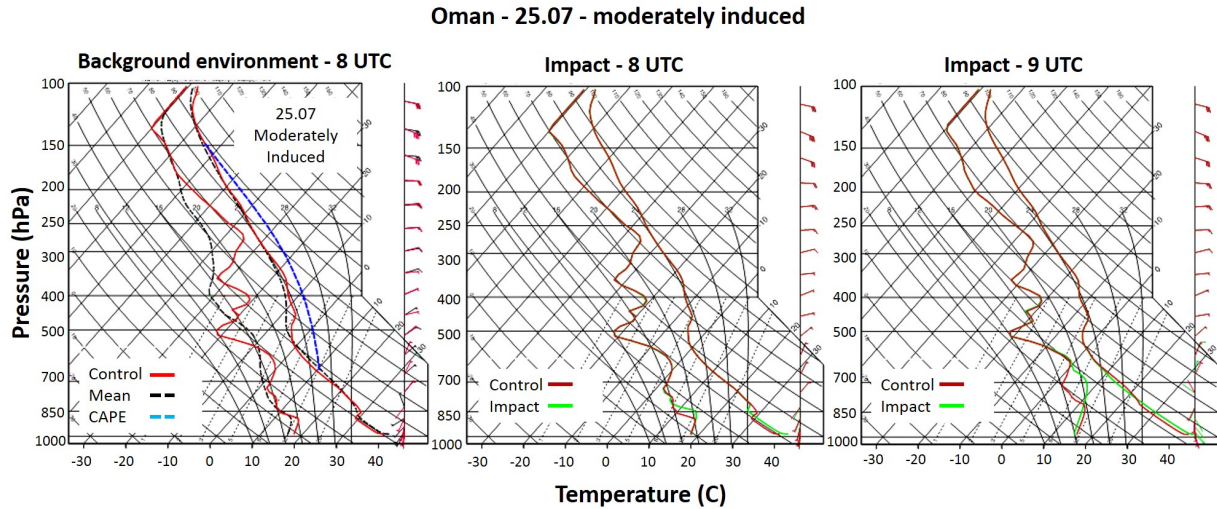


Figure 3.17: Oman environment and impact 25-07 - moderately induced. The plot format is as Figure 3.15.

Surface q_v in CONTROL is around 2 g kg^{-1} higher than the mean. High surface q_v (lower LFC), together with a smaller T_v inversion at 500 hPa (higher EL), maximises CAPE. CIN is quite high though due to a sharp inversion at 850 hPa. The $\Gamma_{700-500}$ is more stable than the previous two examples though - probably the reason why there is no rainfall in CONTROL, even with high CAPE. The background atmosphere is simply more stable in the 700 - 500 hPa layer.

Against this stability, IMPACT has to do more work than on the other days to initiate convection. The plantation has similar mixing effects as before and in this case, enough CIN is overcome to induce convection, but the effect is less strong. This also coincides with a lower P' which is slightly lower than the mean (1.1 hPa).

Israel 27.07 (Figure 3.18) - weakly induced No significant CONTROL rainfall occurred, but in IMPACT a small patch occurs just downstream from the plantation (max 4 mm) (see Figure 3.6).

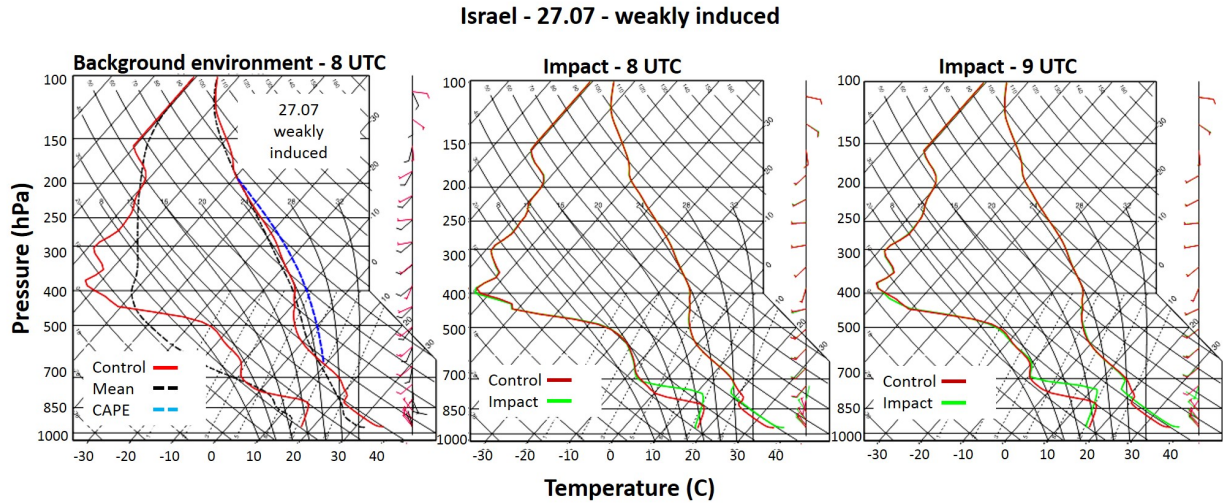


Figure 3.18: Israel environment and impact 27-07 - weakly induced. The plot format is as Figure 3.15.

In CONTROL a strong low level inversion at 850 hPa is present, but has warmer surface T_v and higher surface q_v . A fairly stable $\Gamma_{700-500}$ is also present but much higher than the mean. This highlights the more unstable conditions present during the single slight ‘wet’ period in Israel. Moderate CAPE exists, but with a very high CIN. Therefore, some favorable conditions exist at the surface compared to the mean values but the very dry conditions aloft and high CIN is likely to limit any CI impact. In IMPACT we see some mixing of q_v , but this is strictly limited to a ceiling of ~ 800 hPa. Some breakdown of CIN occurs but again it is very limited. It is likely that a very dry troposphere is causing extremely strong dry air entrainment, limiting CBL growth and therefore q_v transport.

Lateral forcings - The source of temperature lapse rates?

It is worthwhile to consider whether the observed T_v and q_v profiles above the CBL, are traceable primarily to advection via the lateral boundaries, or to processes operating within the mesoscale domain.

In Figures 3.19 and 3.20, the 08.00 UTC Skew-T profiles⁵ from three different dry/wet days, were plotted alongside the lateral forcings from the ECMWF analysis data at the closest preceding timestep to 08.00 (06.00 UTC).⁶ The plots show the observed WRF-NOAH values of T_v (left) and the lateral forcing, both at 600 hPa. The domain lateral boundaries are also marked on the right (yellow polygons). This pressure height was chosen because it lies in the center of the $\Gamma_{700-500}$ layer, which may be one of the strongest precursors for impacts.

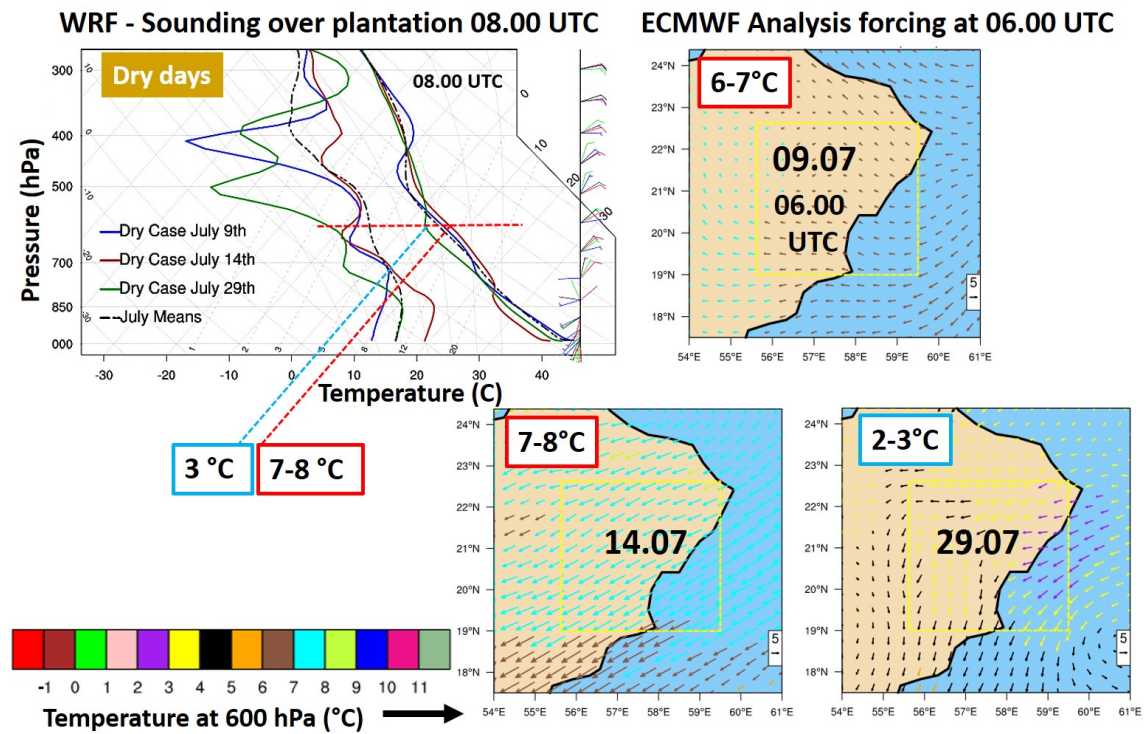


Figure 3.19: Dry days - Comparison of plantation and boundary temperatures (at 600 hPa). On the left, WRF T_v [$^{\circ}\text{C}$] for 09.07, 14.07 and 29.07 (at 08.00 UTC) are highlighted on the Skew-T with blue and red lines parallel to isotherms. On the right, equivalent T [$^{\circ}\text{C}$] boundary forcing from ECMWF analysis (at 06.00 UTC) is shown. The WRF model domain is marked with yellow polygon, and wind vectors are colored for T. The T scale is lower left. The dates are marked in the centre of the domain.

On the dry days (Figure 3.19) the WRF T_v values on 09.07 and 14.07 are similar ($7-8^{\circ}\text{C}$), but the 29.07 is cooler ($\sim 3^{\circ}\text{C}$), which gives us a useful point of comparison to the forcings.

⁵ Plantation footprint mean

⁶ ECMWF Analysis is 6-hourly at 0.00, 06.00, 12.00 and 18.00 UTC

In fact, the forcings appear to correspond well with all respective days, especially on the most relevant boundaries, upwind from the plantation. The differences between the days are also well matched.

On the wet days (Figure 3.20), the WRF T_v values for 29.06 and 30.06 are similar ($\sim 1^\circ\text{C}$), but the 24.07 is warmer (4°C). Again, these values are reflected well by the boundary forcings including the differences between the days.

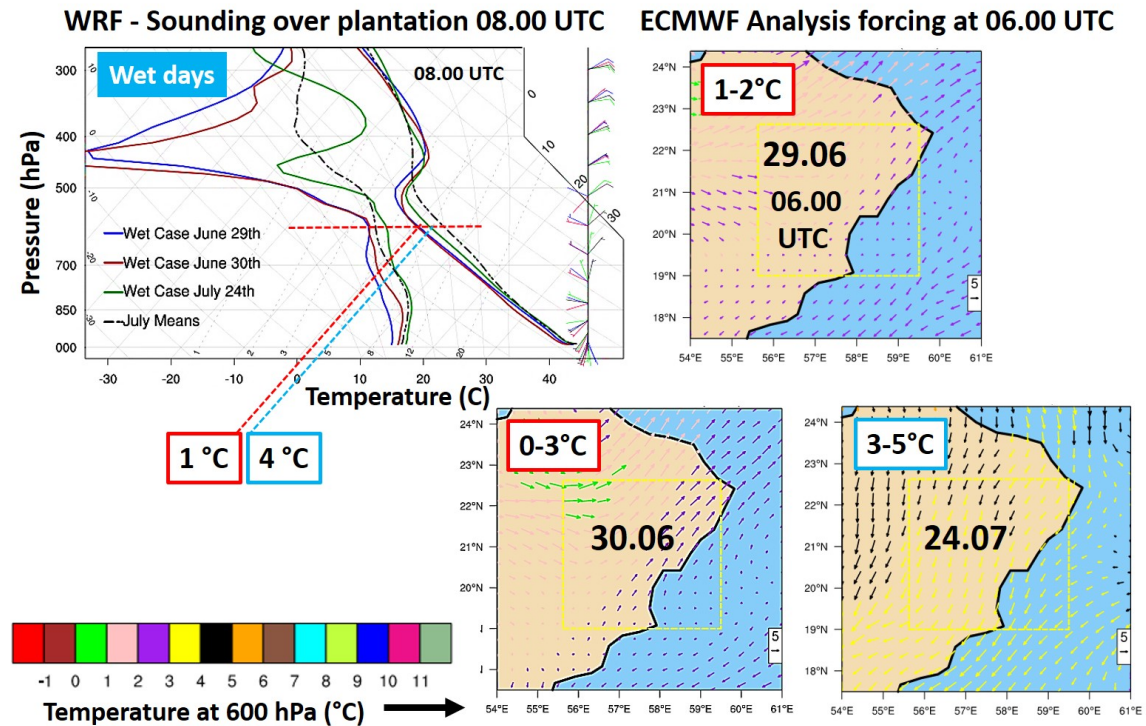


Figure 3.20: Wet days - Comparison of plantation and boundary temperatures (at 600 hPa) for 29.06, 30.06 and 24.07 (at 08.00 UTC). The format is as for Figure 3.19.

We might expect significant modifications to the air mass aloft as it advects from the boundary to the plantation, but the values remain quite consistent. We can therefore surmise that the temperatures and lapse rates at this height are associated primarily with advection from the boundaries, and are not determined or modified significantly by processes occurring within WRF. q_v advection was also examined and although the forcing is reasonably consistent with WRF at the same height, with no significant deviation, the correspondence is not as clear as the T_v comparisons.

3.4 Summary of results

The aim of this section was to assess the impact of plantations on CBL evolution in two regions - Oman and Israel, and to investigate the main mechanisms and precursors for CI.

Precipitation - There are significant CI impacts from plantations in Oman over multiple days, but impacts are extremely limited in Israel. Over 38 days in Oman, IMPACT received up to 24 mm more rain than CONTROL and over a significant area (total domain mass increase 59.9 Pg). In Israel only a maximum of 4 mm difference was observed in one small spot downwind from the plantation (domain mass increase 3.1 Pg).

In Oman, IMPACT enhanced the existing domain precipitation on eleven separate days, and induced rainfall on four days, when none fell in CONTROL. In Oman, two distinct ‘wet’ periods occurred where precipitation was either induced or enhanced. Three ‘dry’ periods could also be identified where all precipitation was suppressed. In Israel, practically the whole 38 days was dry apart from a period of two or three less stable days at the end of July, where a slight inducement of precipitation took place.

Processes - On each of the 38 days, differential heating produced a positive surface T' stratification and a corresponding P' . In Oman, P' ranged from 0.9 - 1.6 hPa (mean P' - 1.14 hPa) and in Israel, 0.85 - 1.5 hPa (mean P' - 1.12 hPa). On the 30.06 in Oman, limited CONTROL rainfall was significantly enhanced by the plantation. On this day, a strong P' of 1.26 hPa induced a mean convergence at the leeside of the plantation. Surface heating led to a progressive de-stratification of the CBL and turbulent transport of θ and q_v . Increased roughness progressively reduced wind speeds towards the leeside, contributing to increased mechanical turbulence and mixing. Convergence strengthened further just before CI (09.00 UTC), and the resulting mean ascent, together with turbulent mixing, led to a final breakdown of CIN, allowing the $\sim 2200 \text{ J kg}^{-1}$ of CAPE to be released. Organization of mean motions started before CI with bands or rolls, which aligned with the mean surface wind flow, and laterally spaced at $\sim 5\text{km}$. Then after CI, progressively larger circulations developed, with length scales between 20-40 km. Updrafts dominated at the beginning of CI, but eventually the downdrafts came to equal and then exceed the updrafts. Cold pooling soon began to reduce the instability at the surface and updrafts and convection then started to reduce.

Precursors - The strength of P' is positively correlated with convergence, T' and $\text{SW}\downarrow$, as expected, whilst T' is negatively affected by increased \bar{U} . Furthermore there appears to be a positive link between P' and CI events, but the thresholds relating to this link are not clear. Given the similar land surface perturbations in Israel and Oman, it is likely that a certain P' is a necessary but not a sufficient condition for CI. The other decisive factors relate to the atmospheric background state.

We have seen that on certain days, there are relatively unstable background conditions, and light patchy rainfall occurs. However, this is significantly enhanced by the plantation, e.g. Oman 27.07, 30.06. On other days, when more stable conditions exist, and zero rainfall occurs, IMPACT can still trigger CI to a certain extent, through convergence and turbulent transport of q_v - 25.07.

Enhancement - a combination of pre-conditions favor enhancement, and these are generally the same conditions required for CI generally (without a lifting mechanism) i.e a high CAPE, not too much CIN, a high lapse rate, and a well-distributed column q_v . The 27.06 is a good example with some small patches of rain. Here, almost all conditions for CI are present, except for a small amount of CIN, which limits the rainfall in CONTROL. CIN was then completely removed by the plantation effect. It is clear that favorable/unfavorable T_v and q_v profiles, can cancel each other out somewhat. On dry days, when a high surface q_v exists, a strong low-level inversion can dominate by increasing CIN, e.g. 17.07 (Figure 3.14). Conversely, there are wet days (e.g. 25.07) where a low-level inversion is offset by high surface q_v - enough, so CI could occur. The difference between dry/wet and induced/enhanced depends on the relative balance of such factors during the day, and whether or not surface parcels can reach their LFC.

Inducement - On days of no background rainfall, conditions are by definition, stable, often due to a low-level inversion. For inducement to even be possible on such days, a defining pre-requisite, is a high $\Gamma_{700-500}$. Even when a low-level inversion is present, a high $\Gamma_{700-500}$, means that if the plantation effect can overcome the CIN through heating and lifting, significant CAPE can be released, e.g. 25.07.

Dominant factors - $\Gamma_{700-500}$ appears to be the dominating factor constraining the possibility of CI. Without exception, on all days in the ‘wet’ periods, $\Gamma_{700-500}$ approaches Γ_d ($\sim 10 \text{ K km}^{-1}$). On all dry days (CONTROL or IMPACT), $\Gamma_{700-500}$ is nearer to a standard-atmosphere⁷ of $\Gamma \sim 6.5 \text{ K km}^{-1}$. Based on the analysis we can see that in July 2012, Israel has a very unsuitable environment for any kind of CI - triggered or not. This is due to the the stable $\Gamma_{700-500}$, and a large drop off in q_v above $\sim 850 \text{ hPa}$. As discussed in Section 1.6, extreme aridity aloft can significantly reduce the buoyancy of ascending parcels, even if surface conditions are favorable. Israel’s climate suitability may improve though during other seasons, or in other years.

Overall, the results suggest qualitatively that at smaller scales, q_v and T_v profiles in the CBL are important for determining CAPE/CIN, and ultimately whether inducement or enhancement occurs or not. Furthermore the strength of P' and \downarrow (driven by T' and $\text{SW}\downarrow$), influences the ability of the plantation to overcome CIN, but that T' is reduced at higher \bar{U} .

At large-scales the strongest atmospheric determinants for CI potential are a) high $\Gamma_{700-500}$, b) well distributed column q_v , and c) high surface q_v . These variables are important, because CAPE is generally optimized when there is both a high surface q_v (\sim lowest 100 hPa) together with a high $\Gamma_{700-500}$ (Markowski and Richardson, 2010), which lowers the LFC for lifted surface parcels. The mid-tropospheric temperatures and lapse rates appear

⁷ International Standard Atmosphere 1976 - ISO 2533:1975

to be predominantly large scale features (as seen at the model boundaries).

Mesoscale processes are inevitably embedded in larger scale systems, which determine the prevailing meteorological conditions (Weaver, 2004a) especially mean stratification, and ascent/descent (Weaver, 2004a,b; Carleton et al., 2008; Markowski and Richardson, 2010; Trapp, 2013). The forcings at the boundaries are completely consistent with this relationship, and especially the premise that differential advection of T at synoptic scales is the most significant determinant of $d\Gamma/dt$ (as discussed in Section 1.6).

Chapter 4

Global Perspectives

It is now apparent that geoengineering scale plantations are likely to have direct impacts on CI, through mean and turbulent motions. It also appears that the potential for the occurrence and strength of such events is dependent on the mid-tropospheric temperature lapse rate, distribution of column water vapor, and surface air humidity. If large-scale systems dictate these variables, then a regional climatological analysis could provide a good estimate of regional potential for impacts. If we can identify arid/semi-arid regions with more favorable mean conditions than others, this would provide more focussed targets for further mesoscale simulation and analysis. Subsequent simulations could then incorporate important smaller scale features, such as albedo (influential in terms of land surface contrasts), land cover, local winds, soils, orography (important for convective events e.g. see Schwitalla et al., 2008; Wulfmeyer et al., 2011). We will assume that hot arid regions will fulfil certain other general criteria, such as high SW \downarrow and clear skies at least for some part of the year.

Before deciding on which target regions to simulate and indeed before implementing plantations anywhere, we may consider what it is that we hope to achieve in terms of impacts. For instance, it may be more beneficial to induce rainfall in hyper-arid regions, or perhaps it could be more useful to enhance existing rainfall in e.g. semi-arid or Mediterranean climates? There may be a potential to achieve either (or both) of these aims, as demonstrated in Oman. Some arid/semi-arid regions have a hot, dry season, as well as transitional/rainy periods. A plantation may induce rainfall in a hot, dry season and yet still enhance existing rainfall at other times of the year. Or it may have no effect during the dry season, but enhance the rainfall at other times. In Oman, we have seen distinct but very short periods, of just a few days, where the potential for impacts varies considerably. Many complex possibilities exist, and these may be indicated in detailed mesoscale simulations incorporating the prevailing regional climate. This analysis will not address such impact ‘goals’, but aims to highlight general climatic potential present in any arid/semi-arid region.

One assumption is made for this analysis: that the most interesting areas will have periods of favorable atmospheric conditions but at the same time, little rainfall. During such times,

perhaps a small but significant inversion is typical which prevents CI, but which may be overcome by strong differential heating/increased turbulence. Clearly, locations where ‘ideal’ atmospheric conditions only coincide with significant rainfall, are less than optimal because there is less need to induce rainfall at these times. In order to investigate specific locations within the various continents and to see how closely climatological forcing data tallies with locally collected data, a further ‘point’ analysis of climate stations was made. This also gives us an opportunity to use local precipitation gauge data. Here, the monthly $\Gamma_{700-500}$ and surface q_v is compared to rainfall and T_{2m} (as a general proxy for solar radiation) station data for every month of the year.

One more factor to consider is the climate variability of potential regions as this could dictate the ‘reliability’ of a region or station for impacts, both for planning purposes and to account for the typical life span of a plantation. Becker et al. (2013) discuss the likelihood of a twenty year *Jatropha* plantation life cycle (due to soil salinity accumulation). Conceivably though, plantations could remain for longer. For instance, the soils under the Jojoba at Hatzetim, are said to have accumulated almost no salinity since 1948, in spite of constant irrigation (Branch et al., 2014).¹ Conducting statistical analyses over climatological timescales is preferable, to account for regional variability.

4.1 Methodology - Analysis of regional and local climates

Two main analyses were conducted: a mapping and a station analysis. For the **mapping analysis**, the following suitability indicator variables were used:

- temperature lapse rate between 700 and 500 hPa ($\Gamma_{700-500}$) [K km^{-1}]
- specific humidity at 900 hPa ($q_{s,925}$) [g kg^{-1}]
- integrated column water vapor (ICV) [kg m^{-2} or mm]

All variables were extracted from ERA-Interim data² (Dee et al., 2011) as thirty three year monthly means (1979-2012). ICV serves here as an indicator for column vapor distribution. This seems reasonable given that if a region has a high surface q_v but a low ICV, then this indicates drier conditions aloft similarly to Israel. Of course this would neglect sharp gradients which may exist in the column and therefore represents a bulk value. The bulk lapse rate ($\Gamma_{700-500}$) was calculated from the air temperature by subtracting T_{500} from T_{700} .

For the maps, mean January and July values of $\Gamma_{700-500}$, $q_{s,950}$ and ICV were plotted for three regions: Africa and the more arid part of Asia, the Americas, and Australia (Figures

¹ This is likely to be due to the annual flushing of the soils by winter rains in Israel ($\sim 200-300 \text{ mm yr}^{-1}$ at Beer’sheva).

² Horizontal grid resolution - 0.75°

4.1, 4.4 and 4.6). $\Gamma_{700-500}$ and q_s are overlaid in the top panels (filled contours are $\Gamma_{700-500}$ and line contours are $q_{s,950}$), and ICV is plotted in the bottom panels. The σ_{dev} and Coefficient of Variation [COV] ($\frac{\sigma_{dev}}{mean}$) were calculated for all variables and summarized as regional ranges in Tables 4.3 and 4.2. Using the COV provides a measure of multiplicative variability (in terms of the mean), and the σ_{dev} provides a measure of absolute deviation. Maps of σ_{dev} and COV can be found in Appendix 6.5.

For the **station analysis**, fourteen climate stations were allocated, selected with respect to a) their positions within known arid or semi-arid, coastal regions, b) availability of climate data, c) their corresponding suitability indicator values. The points are marked on the maps, and are identified by an alphabetical code. Further information for each station is given in Table 4.1.

Table 4.1: Stations analyzed for potential arid agroforestry. Monthly climatologies of $\Gamma_{700-500}$, q_v and precipitation. The station code (left column) is used to label the stations on the maps in Figures 4.1, 4.4 and 4.6. Stations not located in known deserts are marked not applicable (n/a)

Code	Station	Location	Description	Desert	Longitude	Latitude
b	Bir Moghrein	W. Sahara	Coast	Sahara	12.75 W	27.50 N
c	Sessfontein	N. Namibia	Coast	Namib	12.00 E	17.75 S
d	Gobabeb	S. Namibia	Coast	Karoo	15.00 E	23.25 S
f	Beer'sheva	Israel	Inland	Negev	31.25 E	34.50 N
g	Masirah	N. Oman	Coast	Arabian	57.75 E	21.00 N
h	Rajkot	Gujurat	Coast	n/a	69.00 E	23.25 N
i	Jaipur	India	Inland	Thar	71.75 E	27.25 N
j	Escondido	California	Coast	n/a	118.54.10 W	34.00 N
k	Ajo	Arizona	Inland	Sonoran	113.25 W	31.25 N
l	Ensenada	N. Baja Calif.	Coast	Sonoran	116.25 W	32.00 N
m	La Paz	S. Baja Calif.	Coast	Sonoran	110.00 W	23.72 N
n	Antofagasta	Atacama, Chile	Coast	Atacama	70.50 W	23.25 S
o	Boolathana	N.W. Australia	Coast	n/a	113.25 E	24.25 S
p	Badgingarra	W. Australia	Coast	n/a	115.5 E	30.00 S

For each station, the mean (and σ_{dev}) of $\Gamma_{700-500}$ were plotted against $q_{s,950}$, (at the closest corresponding grid cell to the climate station) - Figures 4.2, 4.3, 4.5 and 4.7. Also on the plots the monthly climatology of rainfall/maximum T_{2m} is plotted - Source NOAA (See Table 6.1 in Appendix 6.4 for details on the data source).

4.2 Results and discussion - Potential arid plantation zones

Africa mapping analysis - In Figure 4.1 (top left), the highest $\Gamma_{700-500}$ values occur at the very north west over Egypt (6.6 to 6.8 K km^{-1}) in January, corresponding to winter in the northern hemisphere.

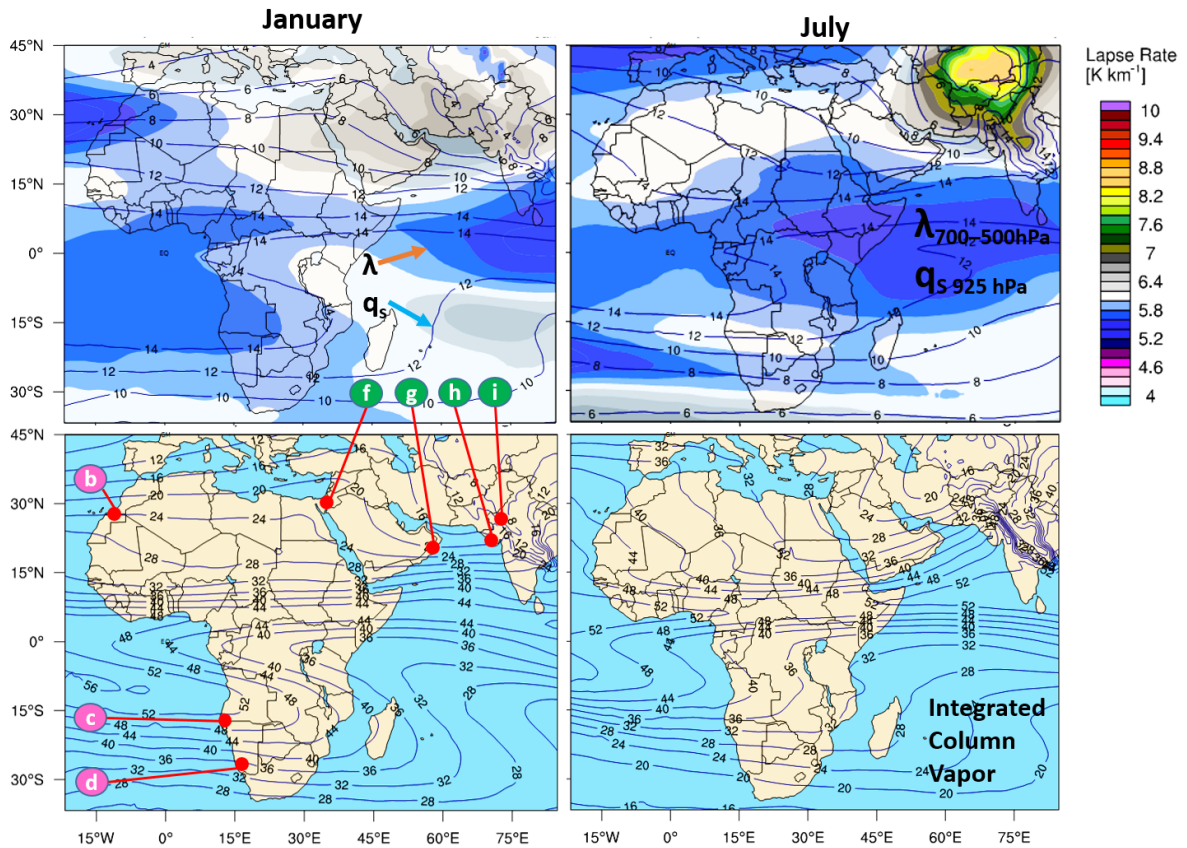


Figure 4.1: Africa and Asia - mapped lapse rate between 700–500 hPa ($\Gamma_{700-500}$) [K km^{-1}] and specific humidity at 950 hPa ($q_{s,950}$) [g kg^{-1}] (top panels). Contour lines are q_s and filled contours are Γ . Bottom panels are total column water vapor (ICV) [kg m^{-2}]. Left panels are January and right panels, July. Values shown are 33 year means from 1979–2012 from ERA-Interim data (ECMWF). Also indicated are potential arid/semi-arid sites for further climate analyses of Γ , q_s and rainfall (marked by letters).

Taking the standard atmosphere tropospheric lapse rate (Γ_{st} or $\sim 6.5 \text{ K km}^{-1}$) as a threshold for high or low $\Gamma_{700-500}$, then this value is unremarkable. It also highlights the generally low $\Gamma_{700-500}$ in Africa. Egypt has a mean $q_{s,925}$ of around 8–10 g kg^{-1} in January and is therefore one of the driest parts of Africa at this time. This is true for ICV as well (bottom left) with only a mean value of 24 kg m^{-2} (or mm). As a benchmark for ICV, Oman has values up to 40 mm during the summer impact runs but Israel, only 26–28 mm. All other areas of Africa are generally more moist in January but have sub- Γ_{st} lapse rates. The Namib desert, which has its summertime in January, has an unfavorable $\Gamma_{700-500}$ (5.8 to 6 K km^{-1}), but has a high $q_{s,925}$ (12–14 g kg^{-1}) and ICV (40–48 mm). Within

the climatic envelope, there are likely to be periods where the lapse rate climbs above the mean, and this high moisture would then provide good conditions for strong impacts. However, given that $\Gamma_{700-500}$ is such a dominant pre-requisite in the Oman/Israel impact runs, the Namib may not be a good choice in terms of long-term impact ‘probability’. During July, there appear to be no areas with particularly favorable conditions overall. The Sahara is very stable (low $\Gamma_{700-500}$, low $q_{s,925}$ and ICV) and the southern regions such as the Namib or Kalahari have low $\Gamma_{700-500}$ and slightly drier air than in January.

Regional σ_{dev} ranges for each region can be found in Table 4.2 and COV ranges in Table 4.3. Africa has reasonably low variability for $\Gamma_{700-500}$ with a max σ_{dev} of 0.4 K km^{-1} (max COV 4%) over both seasons, $q_{s,925}$ has a max σ_{dev} of 0.8 g kg^{-1} (COV 5%), and ICV is more variable with a max σ_{dev} of 9 mm (COV 12%) (See Appendix 6.5 for maps).

Tables of regional variability range

Table 4.2: Regional range of σ_{dev} for $\Gamma_{700-500}$ [K km^{-1}], $q_{s,925}$ [g kg^{-1}] and ICV [mm] for January and July - 1979-2012 ERA-Interim (n=33). See Appendix 6.5 for σ_{dev} maps.

	January			July		
	$\Gamma_{700-500}$ K km^{-1}	$q_{s,925}$ g kg^{-1}	ICV mm	$\Gamma_{700-500}$ K km^{-1}	$q_{s,925}$ g kg^{-1}	ICV mm
Africa	0.2 - 0.4	0.4 - 0.8	2.0 - 9.0	0.2	0.4 - 0.8	2.0 - 5.0
Asia	0.2	0.8 - 1.6	2.0 - 4.0	0.2	0.4 - 1.2	2.0 - 3.6
N.America	0.24 - 0.32	0.4 - 1.8	1.0 - 4.0	0.16 - 0.4	0.4 - 1.0	1.0 - 4.0
S.America	0.08 - 0.28	0.4 - 1.0	1.5 - 4.5	0.1 - 0.24	0.4 - 1.0	1.5 - 4.5
Australia	0.1 - 0.27	0.4 - 1.1	2.0 - 3.6	0.16 - 0.45	0.5 - 1.2	2.0 - 3.6

Table 4.3: Regional range of Coefficient of Variance % [$(\sigma_{dev}/\text{mean}) \times 100\%$] (COV) for $\Gamma_{700-500}$, $q_{s,925}$ and C_v for January and July - 1979-2012 ERA-Interim (n=33). See Appendix 6.5 for COV maps.

	January			July		
	$\Gamma_{700-500}$ %	$q_{s,925}$ %	ICV %	$\Gamma_{700-500}$ %	$q_{s,925}$ %	ICV %
Africa	3 - 4	5	8 - 16	2 - 5	5	8 - 12
Asia	3 - 5	5 - 30	12 - 16	2 - 5	5 - 15	4 - 16
N.America	3 - 5	15 - 30	12 - 16	2 - 5	5 - 16	8 - 16
S.America	2 - 8	5 - 10	4 - 16	2 - 8	5 - 15	4 - 16
Australia	2 - 4	5	8 - 12	3 - 9	5 - 15	8 - 16

Africa station analysis - Looking at some specific locations in Africa (Figure 4.2), the two Namibia stations have low $\Gamma_{700-500}$ ($\sim -6 \text{ K km}^{-1}$) but high $q_{s,925}$ particularly at Sessfontein (12-15 g kg^{-1}). Temperatures are moderately high all year but there is very low rainfall. These statistics fit with the Namib's status as a coastal desert dominated by subsidence but with moist coastal air. The consistently low $\Gamma_{700-500}$ would certainly rule out Gobabeb as a prime location, but in Sessfontein $\Gamma_{700-500}$ is highly variable and may signify some likely periods with favorable conditions, high temperatures and low rainfall, e.g. October to December. At Bir Moghrein in W. Sahara, favorable conditions appear evident apart from the $\Gamma_{700-500}$ which is consistently $< 6 \text{ K km}^{-1}$. Even though there are very moist conditions and high temperatures, significant impacts here may be minimize.

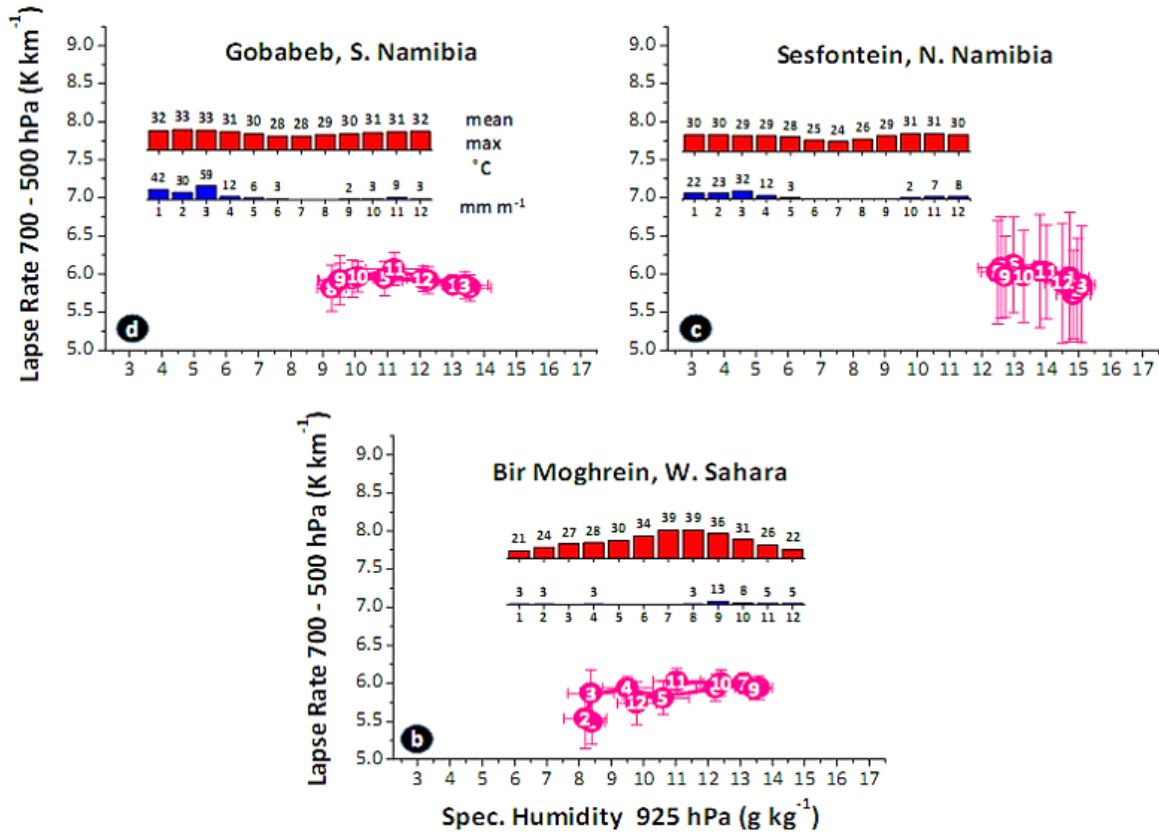


Figure 4.2: Africa stations - $\Gamma_{700-500}$ plotted against $q_{s,925}$ (monthly means and σ_{dev} - 1979-2012) from ERA-Interim. The numbered round points represent the month of the year and horizontal error bars are σ_{dev} for $\Gamma_{700-500}/q_{s,925}$. Also plotted are station climatologies for precipitation (mm m^{-1}) and T_{2m} [$^{\circ}\text{C}$] from NOAA. The single Era-Interim grid cell used corresponds approximately to each observation station. See Table 4.1 and Figure 4.1 for station details and position.

Summary for Africa - The mapping analysis shows that the arid parts of Africa have a low regional potential, with consistently low $\Gamma_{700-500}$. Apart from Egypt, the Sahara region as a whole has low lapse rates and very dry air both at the surface, and aloft. The southern half of Africa is much more moist with summer ICV values in the Namib Desert, close to that of Oman during the observed impact study (40-44 mm). However, the low climatological $\Gamma_{700-500}$ reduces the overall regional potential. Of the African stations, Sessfontein in N. Namibia is the only one worthy of further consideration due to its high moisture, low rainfall and highly variable $\Gamma_{700-500}$, but it cannot be considered optimal because of the low mean $\Gamma_{700-500}$. The others stations have higher $q_{s,925}$ values, but mean lapse rates in Africa are just too low to be of interest for impacts.

Asia mapping analysis (Figure 4.1) - This region is particularly affected by the monsoons occurring over the Indian subcontinent with some very strong effects on moisture and lapse rates (Figure 4.1). In January (during the N.E. monsoon) some slightly high values of $\Gamma_{700-500}$ are evident over Iran and Pakistan (6.6 to 6.8 K km⁻¹). However, due to the N.E. monsoon effect, the area is generally drier than in the S.E. monsoon in summer. The Oman and Israel regions have $\Gamma_{700-500}$ values close to Γ_{st} at this time and dry conditions ($q_{s,925} \sim 8$ g kg⁻¹ and ICV ~ 24 mm). In general, none of the Asian areas look promising during January because of low moisture, lower radiation and average $\Gamma_{700-500}$. During July there are some dramatic mean $\Gamma_{700-500}$ values over the Indian subcontinent and Himalayas (~ 8 to 9 K km⁻¹), as one might expect during the S.E. monsoon. The southern part of Asia is much more moist during this time. $q_{s,925}$ and ICV over Oman in particular increases dramatically (~ 12 g kg⁻¹ and 40 mm). In Israel it remains drier (~ 9 g kg⁻¹ and 26-27 mm).

Asia has low variability (Tables 4.2 and 4.3) for $\Gamma_{700-500}$ with a max σ_{dev} of 0.2 K km⁻¹ (COV 5%) for both seasons, but a higher variability for $q_{s,925}$ with a max σ_{dev} of 1.6 g kg⁻¹ (COV 30%). ICV is moderately variable with a σ_{dev} of up to 4 mm (COV 16%).

Asia station analysis - Starting with Israel, Beer'sheva (Figure 4.3, top right) as expected has a stable $\Gamma_{700-500}$ all year round (≤ 6.5 K km⁻¹) and remains quite dry (6.5-10 g kg⁻¹). Lapse rates increase fractionally during the winter but this is matched with corresponding temperatures which may hinder a strong heating effect. In general though, the unfavorable conditions and low variance of these variables, tends to rule out this area completely. Returning to Oman, Masirah has a wider range of both $\Gamma_{700-500}$ and $q_{s,925}$ compared to Israel. However, perhaps surprisingly, there are no large excursions above the Γ_{st} during the year with a max $\Gamma_{700-500}$ occurring March - May (6.75 K km⁻¹). This coincides with the lowest $q_{s,925}$ of the year though (6-7 g kg⁻¹). Actually, June/July may represent the best combination of factors in this part of Oman, medium $q_{s,925}$ and $\Gamma_{700-500}$ but with high max T_{2m} (35 °C). In spite of that, this location cannot be considered as a prime location in a probabilistic sense, due to the typically average $\Gamma_{700-500}$. Moving to

the two stations in India, we see a much larger range in $\Gamma_{700-500}$, $q_{s,925}$, T_{2m} and rainfall for both Jaipur and Rajkot. Both locations are semi-arid with very distinct wet/dry periods with substantial rainfall falling between June and September often in thunderstorms. Not surprisingly, these periods coincide with very high $\Gamma_{700-500}$ or $q_{s,925}$. These periods are not so interesting for rainfall inducement though. Outside of these periods there are drier months, where $\Gamma_{700-500}$ is significantly high, such as March/April in Jaipur (7.2 to 7.5 K km⁻¹) or April/May in Rajkot (7 to 7.5 K km⁻¹). These months coincide however with the N.E. monsoon drying where dry air is drawn down from the Himalayas, and $q_{s,925}$ of only 4-6 g kg⁻¹ are present. More promising perhaps in these areas are transitional periods around October when $q_{s,925}$ can be around 9-10 g kg⁻¹ and the $\Gamma_{700-500}$ is moderate (6.5 K km⁻¹) and max T_{2m} is still high (~35°C). Again though, if we consider an overall assessment, these locations can not be considered ideal because during the only periods when favorable conditions exist, significant rainfall occurs.

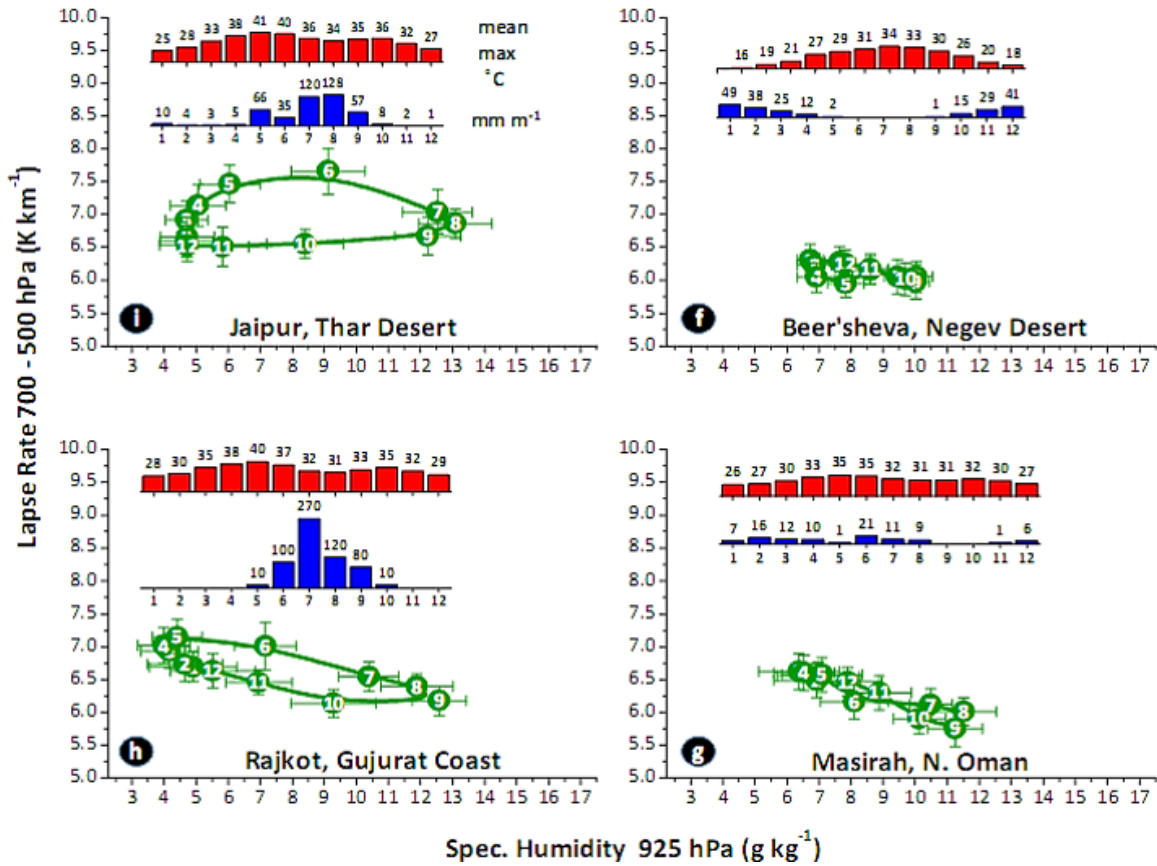


Figure 4.3: Asia stations - $\Gamma_{700-500}$ plotted against $q_{s,925}$ (monthly means and σ_{dev} - 1979-2012) from ERA-Interim. The format is as for Figure 4.2. See Table 4.1 and Figure 4.1 for station details and position.

Summary for Asia - The Asian arid/semi-arid regions see much more dramatic changes in $\Gamma_{700-500}$ and moisture, being affected strongly by the Indian Monsoon. During the N.E. Monsoon (January) there are higher lapse rates (6.6 to 6.8 K km⁻¹) over the Oman, Israel, Pakistan, and Thar Desert regions but this coincides with much drier air and lower radiation. During the S.E. Monsoon (July) the $\Gamma_{700-500}$ over Oman and Israel tends to reduce, but increases dramatically over Pakistan, India and the Himalayas. During this time the air is much more moist over Oman and the Indian subcontinent but Israel's atmosphere does not moisten significantly. None of the stations have 'optimal' conditions. Beer'sheva, Israel is consistently too dry and low $\Gamma_{700-500}$ all year round. Masirah has surprisingly less 'climate' potential than expected given the observed impacts, because the mean $\Gamma_{700-500}$ is quite low, and when it does rise, it tends to coincide with a dry atmosphere. Therefore, the simulations occurred within a period of non-typically high $\Gamma_{700-500}$. At the two semi-arid stations, Rajkot and Jaipur, the best conditions for CAPE occur when significant rain falls and during the dry season the air is far too dry.

Americas mapping analysis (Figure 4.4) - The North American region is profoundly affected by the North American Monsoon (NAM) which normally arrives towards the end of a normally dry June bringing rains which progress up from Mexico to the U.S. great plains. This can be seen in the very strong $\Gamma_{700-500}$ in Figure 4.4. In January, fairly high $\Gamma_{700-500}$ are seen in dry areas such as Southern California and Arizona (up to 6.8 K km⁻¹) but this coincides with very low $q_{s,925}$ and low ICV (4-6 g kg⁻¹ and 14-16 mm, respectively). This is very arid indeed and tends to rule out this time of year, for impacts. In the southern hemisphere the mid-west coast of Chile is well known to be arid (Atacama), but there is a complex coastal variation in moisture, with sharp gradients from the coast, to the Andes. In January (summer), this region is at its most moist. There is a small area around Santiago where a high $\Gamma_{700-500}$ exists and also a higher $q_{s,925}$, but the ICV at the coast does not appear to be very high (≤ 25 mm).

During July, when the monsoon occurs, very large $\Gamma_{700-500}$ values are present in the western part of the USA (8 to 9 K km⁻¹). Large values are also present in drier areas of southern California and Arizona too (7 to 7.4 K km⁻¹). Here, large increases of $q_{s,925}$ and ICV occur, especially towards southern Baja and the Sonoran Desert ($\sim 9-12$ g kg⁻¹ and 40-44 mm). North America has low variability (Tables 4.2 and 4.3) for $\Gamma_{700-500}$ with a max σ_{dev} of 0.4 K km⁻¹ over both seasons (COV 5%). $q_{s,925}$ is a more variable with a max σ_{dev} of 1.8 g kg⁻¹ (COV 30%), and ICV varies up to 4 mm (COV 16%).

Along the Chilean coast there are large increases in $\Gamma_{700-500}$ (6.8 to 7.2 K km⁻¹) too but this coincides with very dry air ($q_{s,925}$ of 4-8 g kg⁻¹, and ICV 12-18 mm). In general, South America has low variability (Tables 4.2 and 4.3) for $\Gamma_{700-500}$ with a max σ_{dev} of 0.28 K km⁻¹ over both seasons (COV 8%). $q_{s,925}$ has fairly low variance with a max σ_{dev} of 1.0 g kg⁻¹ (COV 15%), and ICV varies up to 4.5 mm (COV 16%).

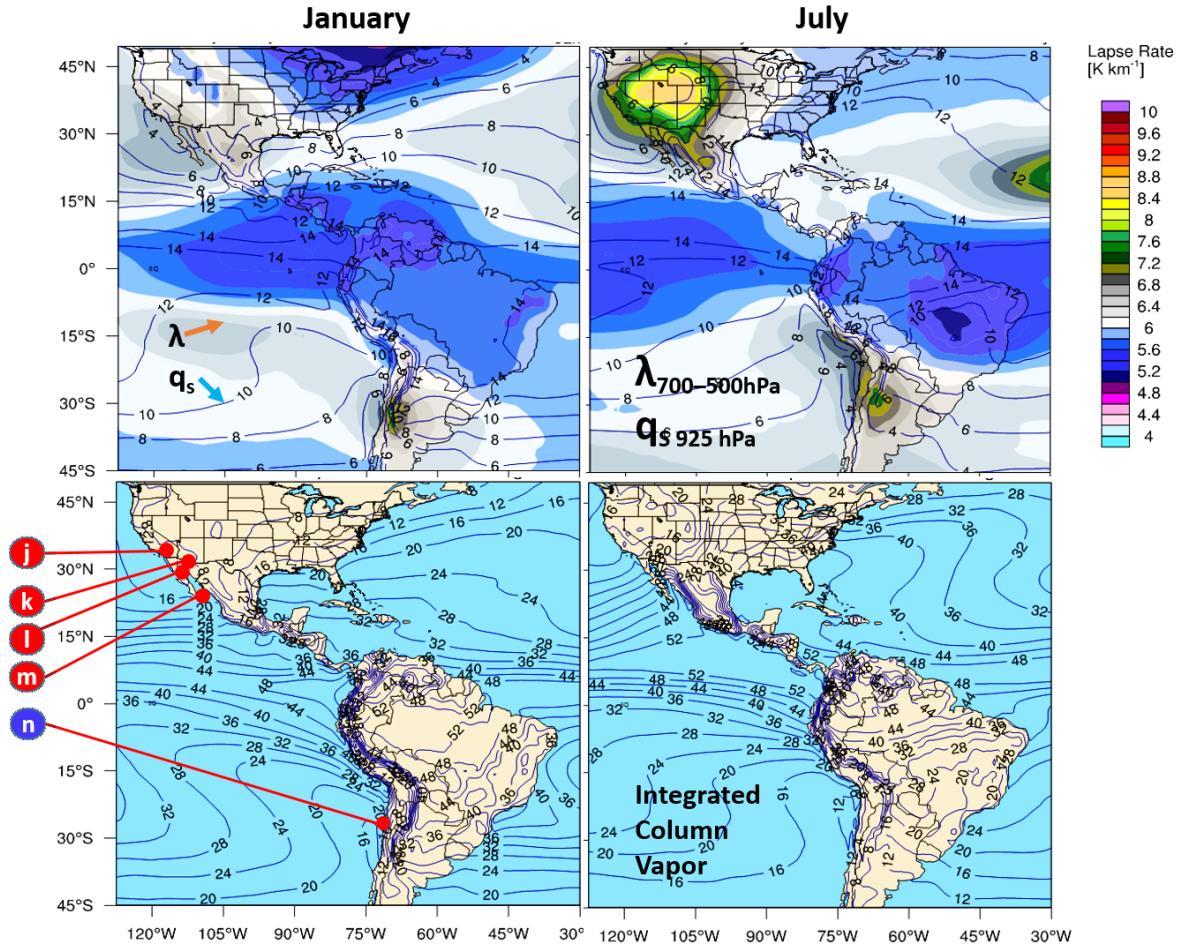


Figure 4.4: Americas - mapped lapse rate between 700–500 hPa ($\Gamma_{700-500}$) [K km^{-1}] and specific humidity at 950 hPa ($q_{s,950}$) [g kg^{-1}] (top panels) - 1979–2012. Bottom panels are ICV contours [kg m^{-2}]. Format is as for Figure 4.1.

Americas station analysis (Figure 4.5) - The four stations in N. America vary considerably both between themselves, and over the year in terms of $\Gamma_{700-500}$, $q_{s,925}$, $\max T_{2m}$ and rainfall. Ajo, in the Northern Sonoran Desert (top left) corresponds approximately to the location of the Sonoran plantation scenario in Wulfmeyer et al. (2014), where rainfall impacts were simulated in June. Ajo tends to have low $q_{s,925}$ throughout the year (3–7.5 g kg^{-1}) with the max values and variance occurring during the monsoon (July–August). What is most striking are the very strong $\Gamma_{700-500}$, which for ten months of the year, strongly exceed Γ_{st} (up to 8.5 to 8.7 K km^{-1} in June). Between April and September these are above 8 K km^{-1} . Even though $q_{s,925}$ tends to be a bit low, the extreme $\Gamma_{700-500}$, high temperatures ($> 35^\circ\text{C}$) and the large variance in moisture in July and August make this location worthy of investigation. Yes, rainfall does occur during these times but it is limited (30–50 mm), and may be considerably enhanced with a plantation, especially with periods of high $q_{s,925}$ advection. Escondido (near Los Angeles) has a Mediterranean climate with winter rain and hot summers. The air tends to be quite dry over the whole

year (3-6.5 g kg⁻¹) but $\Gamma_{700-500}$ values well above Γ_{st} are common throughout the year, reaching a maximum during May-June (~ 7.5 K km⁻¹) which coincides with the highest $q_{s,925}$ (6-7 g kg⁻¹), AND the least rainfall. During the hottest months, July/August (32 °C) the lapse rate falls to ~ 7 K km⁻¹, but this is still greater than Γ_{st} .

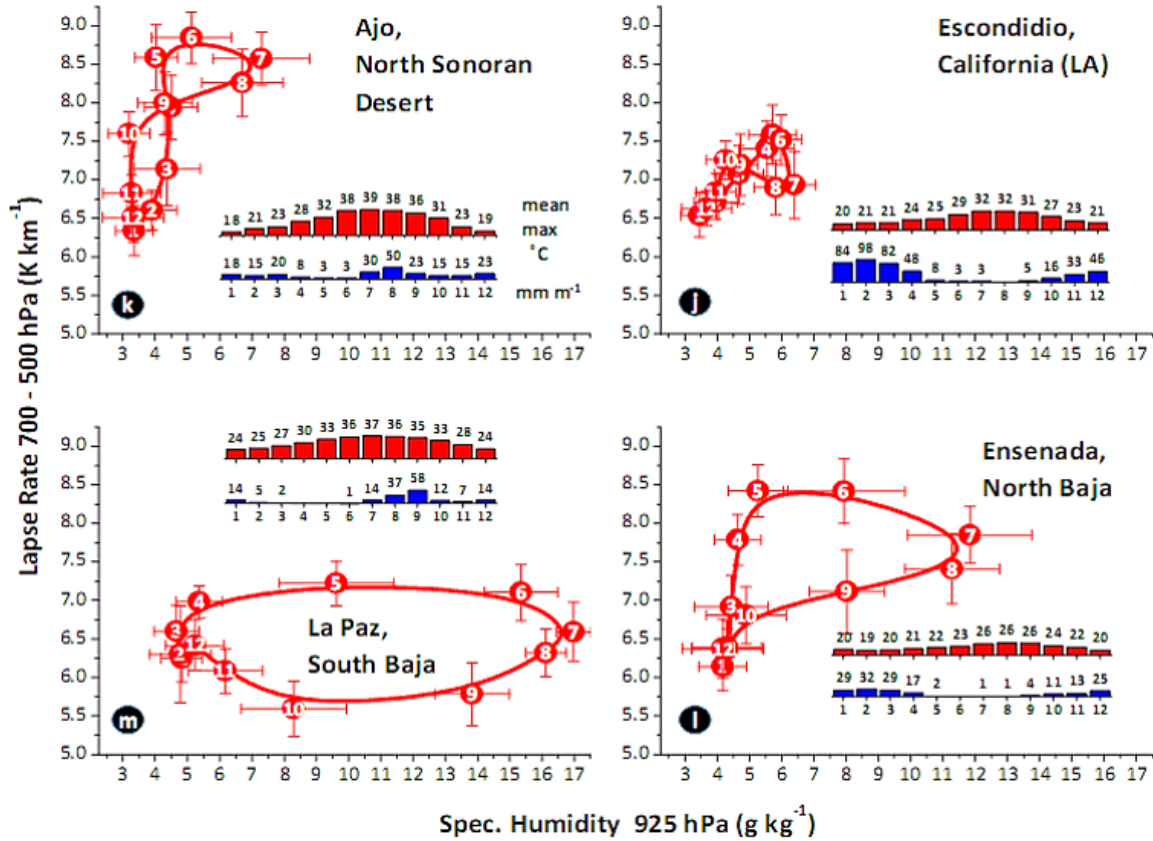


Figure 4.5: North America stations - $\Gamma_{700-500}$ plotted against $q_{s,925}$ (monthly means and σ_{dev} - 1979-2012) from ERA-Interim (single grid cell). The format is as for Figure 4.2. See Table 4.1 and Figure 4.4 for station details and position.

Summary for North America - North America also sees dramatic changes in both $q_{s,925}$ and $\Gamma_{700-500}$, due to the monsoon and there are periods of extremely high values of both variables, within the drier areas of the western USA and Mexico. For this reason the whole region is very interesting from a climate engineering point of view. In January, $\Gamma_{700-500}$ is moderately high over California, Arizona and N.W. Mexico (6.6 to 6.8 K km⁻¹) but $q_{s,925}$ and ICV is quite low. $\Gamma_{700-500}$ increases significantly when the monsoon arrives in July along with $q_{s,925}$ and ICV, with values approaching 10-14 g kg⁻¹ and 30-44 mm, respectively at the tip of the Baja peninsula. From the stations, Escondidio, and La Paz have the largest potential for impacts due to high $\Gamma_{700-500}$ and moisture and the relative timing of rainfall and high temperatures. Ajo, as simulated in Wulfmeyer et al. (2014), is a little dry but has the highest lapse rates of all the observed stations. Any increase in moisture during the summer months would therefore bring about optimal conditions, and

so it is worth further analysis. Escondido is in general too dry.

Australia mapping analysis (Figure 4.6) - The largest $\Gamma_{700-500}$ values occur in the south west of Australia, both in January and July. In January (summer), values of 6.6 to 6.8 K km^{-1} are common along the west coast.

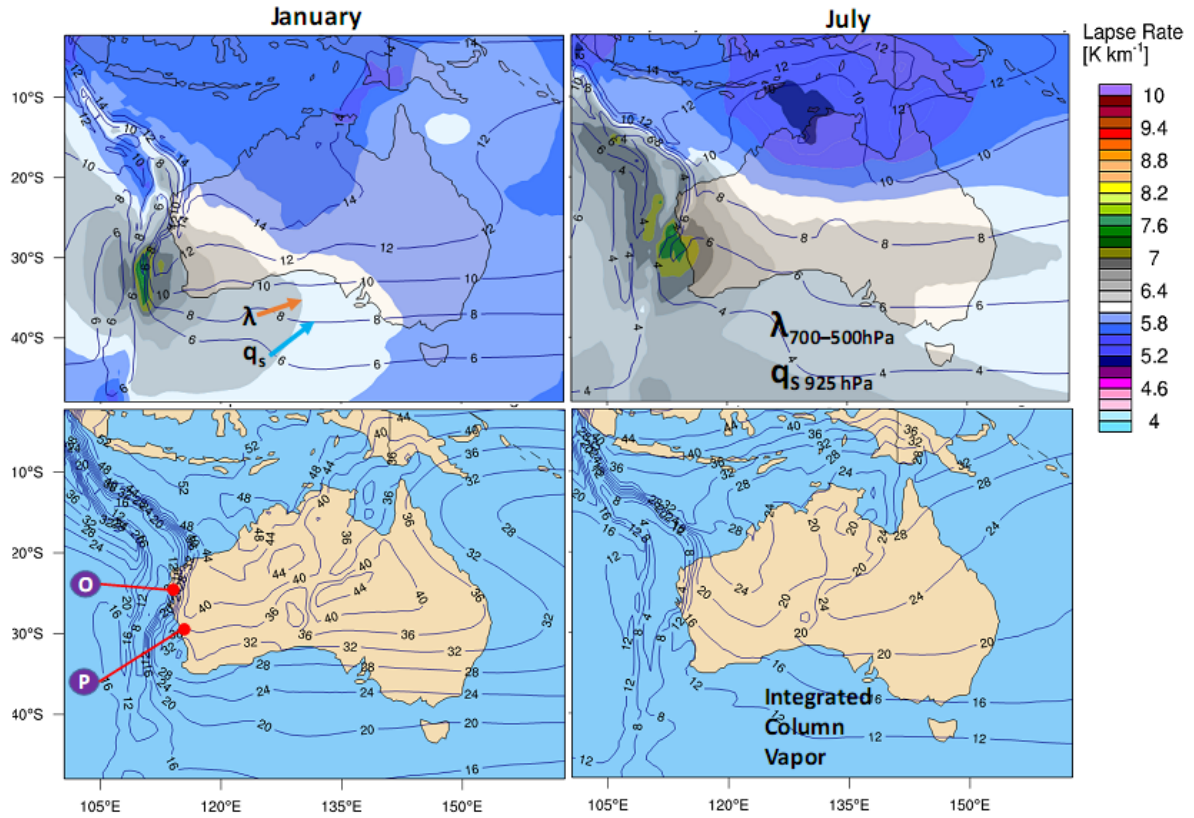


Figure 4.6: Australasia - mapped lapse rate between 700-500 hPa ($\Gamma_{700-500}$) [K km^{-1}] and specific humidity at 950 hPa ($q_{s,950}$) [g kg^{-1}] (top panels) - 1979-2012. Bottom panels are ICV contours [kg m^{-2}]. Format is as for Figure 4.1.

Along this coast, moisture appears quite variable and has sharp gradients, with $q_{s,925}$ varying from 10-14 g kg^{-1} and high ICV values between 32-44 mm. January coincides with the monsoon when most of the annual rainfall occurs in Northern Australia.

In general, Australia has quite low variability for $\Gamma_{700-500}$ with a max σ_{dev} of 0.45 K km^{-1} over both seasons (COV 9%). $q_{s,925}$ also has a fairly low variance with a max σ_{dev} of 1.2 g kg^{-1} (COV 15%), and ICV varies up to 3.6 mm (COV 16%).

Australia and S. America station analysis (Figure 4.7) - Boolathana on the N.W. Australia coast is very arid with almost no rainfall, and high temperatures all year round, peaking in May (40°C).

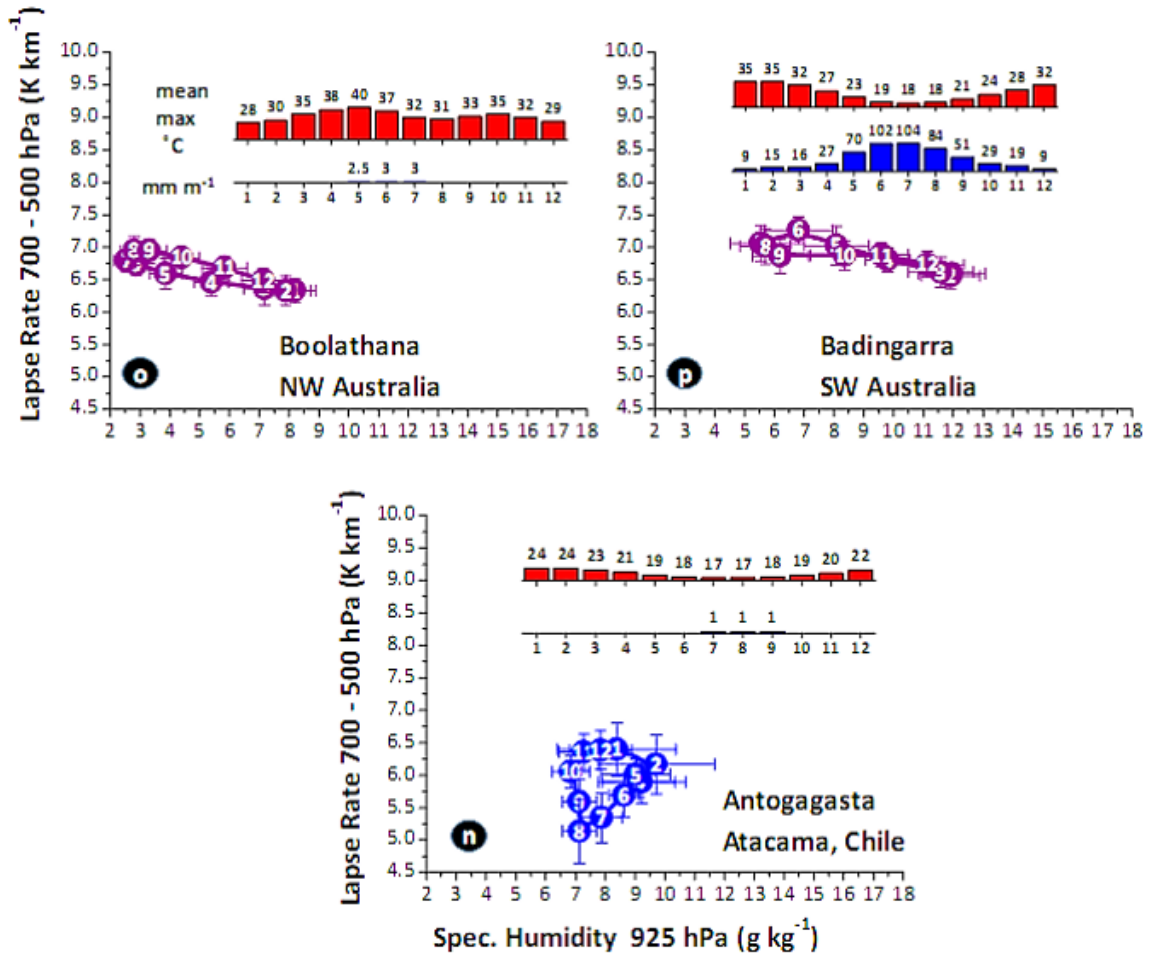


Figure 4.7: North America stations - $\Gamma_{700-500}$ plotted against $q_{s,925}$ (monthly means and σ_{dev} - 1979-2012) from ERA-Interim (single grid cell). The format is as for Figure 4.2. See Table 4.1 and Figs. 4.4 and 4.6 for station details and position.

$\Gamma_{700-500}$ range from $\sim 6.5 K km^{-1}$ in summer (DJF) to $\sim 7 K km^{-1}$ in late winter (August-September). It is likely that this area is far too dry in summer ($2 g kg^{-1}$) when the $\Gamma_{700-500}$ is high ($7 K km^{-1}$). And when the $q_{s,925}$ increases to $8-9 g kg^{-1}$ in winter, then the $\Gamma_{700-500}$ is low ($\sim 6.2 K km^{-1}$). Because of this, the area would not represent a potential location. Badingarra, further south is a more Mediterranean climate with some winter rain and hot summers. The only potentially interesting period in regard to potential impacts is within the dry season (around December), and indeed there tends to be a reasonably high $\Gamma_{700-500}$ ($6.75 K km^{-1}$), high temperatures ($32^{\circ}C$), and high $q_{s,925}$ ($11-12 g kg^{-1}$). Therefore this area may be worthy of further investigation. At Antofagasta, Chile (Figure 4.7, bottom), the most striking thing are the low annual temperatures (max $24^{\circ}C$). These are mostly a result of the abundant cloud/fogs which, although seemingly at odds with the lack of rainfall, are a peculiarity of this coastal desert. $q_{s,925}$ varies between $7-10 g kg^{-1}$, but $\Gamma_{700-500}$ are generally low (5 to $6.5 K km^{-1}$) over the whole year. Conditions here do not appear promising because of the consistently low $\Gamma_{700-500}$,

and also the high predominance of cloud cover which would likely impact on the surface radiation generally.

Summary for Australia and South America - In Australia, higher lapse rates (6.6 to 6.8 K km⁻¹) only occur in the west/south-west of the continent. In the summertime (January), $q_{s,925}$ and ICV values are at their highest along the west coast (10-14 g kg⁻¹ and 32-44 mm) but there are sharp gradients. From the stations, Badingarra with its Mediterranean climate has dry season potential because of the high $\Gamma_{700-500}$, T_{2m} , $q_{s,925}$ and low rainfall.

In South America, sharp gradients of moisture exist along the Atacama coast so it may be dangerous to generalize about impact potential in this area. Relatively high $\Gamma_{700-500}$ can be found but there is generally too little moisture at the coast. Maximum annual ICV is half that found at optimal times elsewhere (20-24 mm). At Antofagasta there are sub-optimal conditions due to low $\Gamma_{700-500}$ and low T_{2m} .

Chapter 5

Conclusions and Outlook

At the outset, the aims of this thesis were summarized as four research questions:

1. *Can desert and Jojoba land surfaces be simulated in a reasonable way by WRF-NOAH, so that mean diurnal fluxes and other quantities correspond well with field observations?*
2. *How do 100×100 km Jojoba plantations modify the summer mesoscale climate in Israel and Oman, particularly regarding CBL processes and CI?*
3. *What are the primary mechanisms and precursors for these impacts?*
4. *Is there a potential for regional selection whereby impacts are more likely?*

The success of addressing each question is discussed, along with key assumptions made, the implications for arid agroforestry, and ideas for future research to improve understanding and methodology.

Question 1 was addressed in Chapter 2 where the principle aim was to configure WRF-NOAH to represent an idealized arid agroforestry scenario within a desert setting. This model would then provide the basis for the impact study. This was accomplished through tailored parameterization of biogeophysical land surface properties, and by introducing a coded irrigation scheme, based on the requirements of specialist desert species. The main requirement for WRF-NOAH was that it should simulate realistically, the mean (and σ_{dev}) of diurnal energy balances and standard meteorological quantities over the desert and plantation. To test the performance of WRF-NOAH, comparisons were made with desert and Jojoba observations.

Key assumptions made within this section were that:

- Grid-scale addition of irrigation water to the sub-soils can represent the more realistic heterogeneous spatiotemporal evolution of soil moisture

- It is a valid approach to compare model output from a simulated 10×10 km plantation, with observations from a $\sim 2 \times 2$ km plantation
- The Penman-Monteith models provide a good estimate of Q_E

In regard to the first point, the model irrigation is sub-surface, and hence there is no direct soil evaporation (ET_D), and hence Q_E is comprised solely from the plant transpiration, which more or less matches the reality at Hatzetim. However, the temporal evolution of the soil cannot be simulated so easily. In reality, water is targeted directly at the root ball, whereas in NOAH, the entire volume of each layer is wetted. Drainage is therefore extremely slow and hence the evolution of η is unrealistic. In fact, η remains almost constant, despite the 7-day watering interval, whereas in reality, η fluctuates more dramatically. Therefore, the variability in Q_E over time scales of e.g. a few days, may not be well represented (see Branch et al., 2014). The difference in variance is evident in Figure 2.6, which shows that observed peak $Q_E \sigma_{dev}$ is 20-25 $W m^{-2}$ (Penman FAO 56), whereas in WRF-NOAH σ_{dev} is 10 $W m^{-2}$. The implication is that actual partitioning into Q_H will also be more variable. On days when Q_H is high we would expect a stronger P' , more turbulence, and a stronger impact, and vice versa on weaker days. In the end though the Q_E variance is not significantly large. This simplification is one reason for validating only mean diurnal curves, and not time series.

For the second assumption, we are assuming that the air mass over the 2×2 km plantation would acquire similar characteristics to a larger plantation of e.g. 10×10 km. Normally, an internal boundary layer develops upon a stepped change in roughness, and the rate at which it grows with fetch, depends on roughness and stability. In rural conditions, height:fetch ratios might vary from 1:10 in unstable conditions, to as large as 1:500 in stable cases (WMO, 2008). In unstable conditions and with a height change of 3 - 4m, we can therefore expect advection effects to be greatly reduced after a few hundred metres. Despite this, P' and \bar{U} may scale with the plantation size. Additionally, the wide spacing between the Jojoba plants ($\sim 70\%$ canopy cover) could lead to local heterogeneity and unusual turbulence effects, leading to CBL effects which WRF-NOAH cannot capture. To test the effect of plantation size, informal comparisons were made between the 5×5 cell plantation and a single grid cell, over one week. Diurnal cycles and σ_{dev} of fluxes and U were not significantly different. Therefore we may assume that the methodology used is reasonably sound.

Regarding the last assumption, the Penman Monteith model should provide a full solution to the energy balance, with the only compromise being the linearity of the vapor pressure to temperature relationship. This remains valid as long as crop surface temperature is within a few degrees of air temperature. Used with representative climate data, soil heat flux and resistances, it is theoretically a sound model of evaporation Brutsaert (1982); Monteith and Unsworth (1990).

Turning to the validation results, we have seen that for the most important variables relating to Q_E (T_{2m} , \bar{U} , VPD and R_N), the model generally deviates only marginally from the mean observations (during daytime). IMPACT T_{2m} is a little too cool though at high noon (~ 1.5 °C) implying that simulated P' may be too low, and the impact may be underestimated. The general shape of the diurnal curves are well matched (apart from Q_G) and σ_{dev} generally match with the observations. For the fluxes, which are arguably the most important results for the impact study, Q_E matches well with the Penman FAO 56 model especially the diurnal curve shape and simulated Q_H matches well with observed residual Q_H . Simulated Q_E variance is a little low, as discussed though. In answer to the research question, we can say that the simulation of Jojoba and desert along with their corresponding surface exchanges, has been largely successful barring some adjustments to soil thermal properties. In particular, the fluxes are well simulated. Therefore, conducting further impact studies with this configuration is a reasonable prospect.

A final aim was to assess the resulting flux gradients and weigh the implications for regional studies. The strong heating effect over Jojoba compared to the desert, seems to contrast with findings/assumptions of ‘irrigation cooling’ effects cited by numerous studies (Section 1.5.3). The primary reasons for this reversal relate to assumptions about crop types, and irrigation methods. Jojoba/Jatropha can thrive on minimal irrigation without stress, whereas other crops may require more intensive irrigation. Furthermore, we are assuming sub-surface deficit irrigation, which minimizes input requirements and losses to ET_D . Other crops may be irrigated with furrow, flood or sprinkler methods, where much greater Q_E comes through ET_D and canopy interception. These differences have significant implications not only for climatic impacts, but also for assumptions made in arid regional studies of irrigation.

For further studies, there are various pathways one may take to improve or expand these methods, and this should be considered in terms of remaining uncertainties. In this thesis, WRF-NOAH was configured to simulate a very large canopy, with homogeneous soil moisture - an idealized case one might say. For such a scenario, a relatively simple canopy representation may be sufficient to assess mesoscale impacts, as long as the mean energy partitioning is representative, and \bar{U} and T_{2m} reasonable (for P'). However, such a success might not be achieved for the right reasons in terms of plant/water or other land surface processes. This may not matter if we are only interested in CI impacts, because the main exchanges with the CBL have been adequately reproduced. However, we may wish to improve the physical realism of plant/canopy/irrigation representation a) to increase our certainty that land/atmosphere coupling is realistic, and b) to make adjustments to variables in a more physically based manner. In that case, more complex descriptions of land surface processes may be necessary - and such developments are ongoing. The original NOAH community model (used here) represents the land surface with a single canopy (and energy balance). The newer NOAH-MP, or multi-physics model (Niu et al., 2011)

offers a dual-layer canopy and a semi-tile approach to canopy cover, as well as multiple options for runoff, leaf dynamics, and stomatal resistance schemes. At the moment it is not certain whether added complexity for all processes would significantly improve realism in a case like this one. Important variables for the fluxes, such as R_N may benefit from more advanced descriptions. NOAH-MP for instance uses a probabilistic gap method for shaded/sunlit SW transfer, whilst calculating the LW and fluxes using the semi-tile approach. This has implications for the diurnal evolution of available energy. It is certainly likely that model performance can benefit from parameter or process adjustments for arid conditions, as found by Unland et al. (1996) (Section 1.1). The ability to select different land surface physics options, may be very useful in this respect.

In terms of validation for the impact studies, further confirmation of flux partitioning and information on stability may be desirable. In this case, the measurements could be extended to include eddy covariance, or other energy balance methods. Furthermore, given the high deviation of Q_G more heat flux plates may provide a better representation of Q_G and confirm that the model deviation is not attributable to measurement error. If not, then soil conductivity and diffusivity parameters may be further adjusted in the model, ideally with soil measurements/calibration. Next, the inclusion of irrigation, sap flow and soil measurements could allow for deeper insight into the diurnal and inter-diurnal hydrological cycle. Combining these latter measurements with fluxes, could allow a more detailed ‘real-time’ irrigation parameterization to be developed - calibrated to account for sub-grid and temporal heterogeneity. Finally, more detailed representation of species characteristics, especially stomatal resistances, LAI and phenological stages, may improve their representation within the model.

2. *How do 100×100 km Jojoba plantations modify the summer mesoscale climate in Israel and Oman, particularly regarding CBL processes and CI?*
3. *What are the primary mechanisms and precursors for these impacts?*

Question 2 and 3 were addressed in the Chapter 3 impact study. The methodology used was a qualitative assessment of CI events and precipitation. The main processes occurring in IMPACT were analyzed, relating to turbulent transport of scalars within the CBL and the organization of circulations. Statistical correlations between important surface variables were also examined to assess links between $SW\downarrow$ and \bar{U} with P' , T' and $\vec{\psi}$. Finally, based on the categorization of CI events in Oman and Israel, an analysis of atmospheric precursors was carried out.

By keeping the model configuration consistent (with changes to domains), it is presumed that the fluxes and other key variables are representative over the relevant land surfaces. In spite of this, some key assumptions are still being made:

- Scaling the 10×10 km plantation up to 100×100 km would yield a ‘realistic’ simulation
- Processes relating to the CBL, CI and convective precipitation are simulated in a reasonable way by WRF-NOAH

Regarding the first point, it is certainly likely that the wind field, T_{2m} , P' , and other quantities will differ from those over a smaller canopy. The slowing of \bar{U} due to progressive drag over a large canopy, is one example of such a difference. Ultimately though, without large-scale canopy data, we have no means to assess how closely the upscaling would mirror reality. In this case, the best effort has been made to connect these scales, and to achieve ‘representativeness’, given the data available.

Regarding the second point, we have mentioned the advantages of finer convection permitting resolutions on convective processes in Section 1.1. Grid resolutions in WRF of $\lesssim 3$ -4 km have been demonstrated to yield superior performance, in weather forecast (Bauer et al., 2011) and in regional downscaling modes (Warrach-Sagi et al., 2013). Furthermore the best effort to match appropriate physics schemes for the application has been made (Section 2.2). Further analyses of the performance of WRF-NOAH (and physics schemes), is out of the scope of this study, and so a reasonable representation of convection processes is assumed.

One of the aims of the impact study was to compare findings with those of Wulfmeyer et al. (2014), but based on a validated configuration. In terms of positive precipitation impacts and the primary mechanisms by which CI impacts occur, the results tend to confirm the Wulfmeyer et al. (2014) findings. Additionally, some key relationships and constraints on these mechanisms have also been identified, particularly through comparison between Israel and Oman and of wet/dry days in Oman.

We have established that there are two simultaneous mechanisms for CI. One is an increase in buoyant/mechanical turbulence caused by CBL heating/increased roughness. This leads to a thorough mixing of q_v and T_v throughout the CBL and a progressive increase in CBL height. This has the effect of breaking down CIN through de-stratification and the lifting of moist parcels towards their LFC. The second mechanism is a heat-induced P' and wind convergence, which provides a further lifting mechanism and generates circulations. $\vec{\psi}$ is dependent on P' , and is likely to be negatively proportional to \bar{U} . P' itself is dependent on R_N , T' and \bar{U} and T' is dependent on Q_E / Q_H partitioning. These (mostly non-linear) relationships imply that the generation of convergence and buoyant/mechanical turbulence could be maximized through species choice, plantation design/location and irrigation management.

Choice of species could have a large effect on P' and TKE, via a multitude of characteristics. However R_N and T' are two primary pathways. We have already seen the Jojoba/Jatropha albedo difference [$\sim 0.12/0.17$] and T_{2m} difference [36/38 °C] from Figure 1.3. Counter

intuitively though, the increased Jojoba R_N was not translated into higher T_{2m} , signifying other factors at work. There are many potential reasons, but possibilities are: a) increased *Jatropha* Z_{0m} , leading to lower \bar{U} (See Appendix 6.1, Figure 6.3), b) differences in diurnal R_{st} and Q_E patterns, and c) differences in leaf heat-radiation efficiency (as discussed in Section 1.4).¹

However the *Jatropha* T' surplus occurs, we might expect P' , and buoyant TKE over large *Jatropha* plantations to be larger than equivalent Jojoba ones. Furthermore, slower winds are likely to be less detrimental to circulation development, as found in Dixon et al. (2013) and Avissar and Schmidt (1998) (Sections 1.5.2 and 3.3.2). Just to complicate things though, increased shear turbulence from greater roughness may decrease T' stratification in accordance with Equation 3.1, and weaken P' so there may be some cancelling effects. These are issues where further model sensitivity tests of land surface properties could provide great insight.

The specific positioning of a plantation could also directly affect the strength of the horizontal flux gradients through plant/substrate albedo (R_N) contrasts. This could be optimized by choosing areas with high albedo soils, and using low albedo species.

Another means of maximising impacts could be through irrigation or transpiration management. For instance, by withholding irrigation for some days (especially when atmospheric conditions are seen as optimal for CI), a resulting closure of stomatal apertures could significantly increase energy partitioning into Q_H as seen by Saaroni et al. (2004) during the noon hiatus in the oasis cooling effect (Section 1.5.3). If this stress impact is manageable by the plant, this would significantly increase TKE and P' for a short time, through buoyant turbulence and heating. This effect could also be achieved through partial root zone drying or using the anti-transpiration methods mentioned in Section 1.3. For the latter, one of the problems found with some anti-transpirants was a limited temporal effectiveness, before unacceptable stress occurred (Kreith et al., 1975). Perhaps a brief period of application may be ideal for this purpose, if it could be applied on relevant scales.

It is clear, especially through the regional comparisons, that P' is a necessary but not sufficient condition for impacts. Indeed, once P' reaches a certain magnitude, other factors may become just as important. We have seen that the mean atmospheric state is extremely important for regional CI potential, and that the strongest determinants are a) a high $\Gamma_{700-500}$, b) a well distributed column q_v , and c) a high surface q_v . The first two variables in particular can be considered as pre-requisites for CI impacts to occur at all, even when a daily P' of $\sim 1\text{hPa}$ is present. In Israel, the sharp negative gradient in q_v above 850 hPa, and the stable $\Gamma_{700-500}$ strongly prevents impacts from occurring, and signifies the

¹ Advection bias over the smaller 2 ha *Jatropha* plantation can be ruled out, because peak T_{2m} over both plantations is higher than over the desert in any case (Figure 1.3)

importance of the atmospheric state aloft. Within a more favorable climate, such as Oman, thermally-induced CI becomes possible. From the analyses of cases we can see that profiles of q_v and T_v within the CBL are extremely important for CAPE/CIN, but also that various combinations of (compensatory) surface profiles can allow, or prevent CI impacts. Ultimately, the strongest clear finding is the dependence of CI on $\Gamma_{700-500}$ (from Figure 3.14), where it is the defining difference between wet and dry days.

Further modelling case studies may provide insight into how convection processes might change, when other plantation variables are altered and may be considered once suitable regions have been identified. Examples of variables are, plantation sizes, shapes, species, and albedo contrasts. We may wish to improve the resolution of turbulence and convective processes, for visualization and better understanding. To explicitly simulate eddies on much smaller scales than the CBL height, much finer grid scales will be necessary. The embedding of large-eddy simulation (LES) modes within mesoscale grids is now becoming more common, as computing power advances (e.g. Moeng et al., 2007; Talbot et al., 2012; Wang et al., 2013). Such tools could deliver extremely high resolution of plantations and turbulence (~ 100 m or less), that is, if large enough domains can still be realized at those resolutions. As well as explicitly resolving very fine eddy scales, we can represent much smaller land surface units, such as land use type, soils and orography. Through the reduction of turbulence parameterization, this opens the door to: a) improved simulation of convection, b) direct investigation of edge/wake/IBL/coastal phenomena, and c) the direct examination of canopy turbulent processes (e.g. such as Finnigan et al., 2009). Such analyses would significantly improve our understanding of CBL processes over plantations and verify the quality of these findings.

4. *Is there a potential for regional selection whereby impacts are more likely?*

Question 4 was addressed in Chapter 4 through a qualitative global analysis of thirty three years of ERA-Interim climate data, and based on the mean suitability indicators: $\Gamma_{700-500}$, $q_{s,925}$ and ICV identified in Chapter 3. The mapping analysis was to provide a general sense of the potential of a whole region, in summer and winter. The main aim being, to prioritize certain areas for further modelling and analysis. The point analysis zooms in on some potential locations for a more detailed monthly analysis of CAPE determinants ($\Gamma_{700-500}$ and $q_{s,925}$) and takes advantage of climate station rainfall/temperature data - the idea being, to explore seasonal coincidence of CAPE predictors, temperatures, and rainfall at selected locations.

During the analysis two key assumptions have been made:

- Optimal or non-optimal regions can be identified with a coarse scale analysis
- Potential for specific locations within regions can be identified by combining the

mean state with local station data

The first point relies firstly on the premise that mesoscale phenomena are embedded in and are strongly influenced by synoptic scale systems. If the mean state of the atmosphere - in terms of $\Gamma_{700-500}$, and also $q_{s,925}$ and ICV - is largely determined on such spatial scales, then a 0.75° scale analysis should be representative for those variables, depending on variability. We know that convective processes are determined both by the mean state, but also by finer landscape features such as orography, coastal effects, soil moisture gradients, and many others. In spite of this, if we are only trying to identify those regions with a high probability of an optimal mean state, then the approach makes sense - especially so, if the goal is to set priorities for further simulations, using finite resources.

Taking this regional approach, it seems reasonable to regard arid Africa for example, as a region of low 'mean state' potential, primarily due to the low $\Gamma_{700-500}$. Within Africa though, specific areas may have landscape characteristics which may improve local potential, whilst still being constrained by the mean state. Our point analysis takes the regional analysis a step further and aims to provide a measure of both regional and mesoscale potential. In doing so, we rely on the assumption that precipitation climatologies are representative for a location, and also that combining it with coarser scale data is a valid approach. Climate data tends to be less densely measured in arid developing regions. If the inherent temporal and spatial variability of rainfall and rain gauge error are considered, then some measure of caution is needed with interpretation. However in general, twenty years of station data has been used so it seems reasonable to expect that the seasonal distribution of rainfall should be well represented, even if the quantities are biased.

Variance is an important factor within the analysis and can indicate the changeability of a region's climate and hence, the reliability of our estimate. It may also indicate problems within the data, such as suddenly altered methodologies. Low variances are preferred because of the higher certainty they give our estimations. The other side of the coin is that high variability of e.g. $q_{s,925}$ may allow impacts to occur in low potential areas in spite of a poor mean conditions, such as in Oman. Given that probabilistic estimates of suitability are a key aim, the variance should be strongly factored into any interpretations.

The main findings suggest, based on the last three decades, that the south-west of North America has the highest potential of all the regions, due to high simultaneous values of all indicators, particularly $\Gamma_{700-500}$. Furthermore, Baja California and the Sonoran Desert areas appear the most suitable candidates for simulations. This is due to extremely favorable mean conditions, and also because low rainfall coincides with optimal conditions, particularly at La Paz and Ensenada in Baja California. Variability in moisture is high however in this area, with common summer (most optimal months) COV values of 15%, for $q_{s,925}$, but this may bring more moist, as well as drier periods. In general, those areas

with large annual variability, such as in monsoonal areas, e.g. La Paz and Jaipur, tend to exhibit the largest monthly variances, and those with the lowest annual variability, e.g. Beer'sheva, also have the lowest monthly variances too. The consistent association of these variances to monsoonal or non-monsoonal zones, makes it more likely that high variances seen at Ensenada arise for climate-based reasons, and not from data error. One or two stations though had low annual but high monthly variance, such as Sessfontein and Antofagasta, which decreases certainty at the locations

Other regions around the globe have less than optimal mean conditions, when the point analysis and variability are factored in. Over the Indian monsoonal region, high $\Gamma_{700-500}$ values were also found to some extent. However, point analysis reveals that optimal conditions in Asia (summer) tended to coincide with heavy rainfall at Rajkot and Jaipur. Before disregarding Asia though, further climate stations should perhaps be examined, to be more certain of regional potential, especially in view of the favorably high $\Gamma_{700-500}$. Another interesting sub-region which may be worthy of further investigation is the coast of N. Namibia. This area has the most conducive mean conditions in Africa, including a highly variable $\Gamma_{700-500}$. S.W. Australia may also have potential due to the coincidence of low winter rainfall with optimal mean conditions.

Ultimately, it may be wise only to consider those results which really stand out, as being conclusive. In that case, we could probably say with confidence that the south-west of North America can be considered a priority region. The first reason for this conclusion hinges on the regional presence of high $\Gamma_{700-500}$, high ICV and reasonably high $q_{s,925}$. The second is the high coincidence of these conditions with periods of low rainfall at two of its stations. The other regions of Asia, Australia and African appear to be less than optimal, but may require more detailed analysis before they can be regarded as having 'low potential'.

Further studies could be directed towards improving the robustness of predictions, at least in a modelling sense. One way of doing so may be to include more variables in the regional/station analysis, such as solar radiation and divergence. Furthermore, instead of using selected single climate stations, gridded data would be preferable, where it is available at high enough spatial densities and quality, and over sufficient time spans. This would provide a more solid picture of rainfall distribution with which to compare with the coarser data. Finally, these or similar predictions, should be tested by running simulations at optimal or/and sub-optimal sites, e.g. La Paz and Antofagasta over a representative period for comparisons.

Implications and Outlook

Arid agroforestry implemented on geoengineering scales could provide a significant contribution towards mitigation of anthropogenic climate change. Moreover, the exclusive use of marginal or degraded lands could minimize food security issues typically associated with land use change. Other agroforestry potentials are the advancement of agricultural/economic development in arid regions, and the mitigation of desertification.

Until now, the likely impacts of agroforestry on mesoscale climate within different arid regions has been relatively uncertain. Wulfmeyer et al. (2014) demonstrated with mesoscale models, that plantations could have significant impacts on the climate, particularly convective processes. Still lacking though, was a realistic model scenario, with irrigation and validation. This thesis has attempted to address these issues. In doing so, we have gained a deeper understanding of the most important CI impact processes, and identified some important relationships/thresholds which relate T' , P' , \bar{U} , $SW\downarrow$, and thermodynamic profiles to CI occurrence. Most significantly, these experiments demonstrate that plantations can in fact induce or enhance convective precipitation, but that strong impacts will only occur under the right atmospheric conditions. A central premise underlying the 'impact' hypothesis, is that Q_H will dominate Q_E over plantations during the day - a relation which in turn depends on a myriad of plant/soil/irrigation characteristics and evolving states and feedbacks. Through analyses of observations, we now have some confirmation that Q_H does in fact dominate Q_E over an operational Jojoba plantation. We have also identified potential pathways to increase this heating effect, primarily through agricultural manipulation of irrigation/transpiration. With this in mind, it should be considered that an increase in surface temperatures may not be a welcome impact for workers and local inhabitants.

Finally, the identification of the three key climate precursors for CI impacts ($\Gamma_{700-500}$, $q_{s,925}$ and ICV) is a significant finding. These precursors hint at the potential for maximizing CI probability through selective placement of plantations. If climate constraints really are the primary determinants for impacts, such analyses would then be made easier because climate data of the relevant variables are readily available. The preliminary analysis carried out here has identified the Baja California/Sonoran Desert region as an optimal location in terms of climate precursors, and this is an important first step for prioritizing further modelling and analysis. More research lies ahead though, to confirm these findings and also the status of other regions.

The outcomes of this thesis have underlined the significant potential for arid agroforestry, in the context of urgent global environmental issues. They have also highlighted several areas of remaining uncertainty, as well as some potential avenues of research to address them. Through research of this kind, we can provide policy makers with the decision making tools needed to make holistic assessments of arid agroforestry solutions.

Symbols and Abbreviations

$\bar{u}(z)$	Mean wind velocity at a reference height [m s ⁻¹]
$\Delta z(t)$	Displacement height at time t [m]
η_{fc}	Soil field capacity [m ³ m ⁻³]
η_{wp}	Soil wilting point [m ³ m ⁻³]
η	Soil moisture fraction [m ³ m ⁻³]
Γ	Environmental lapse rate [K km ⁻¹]
$\Gamma_{700-500}$	Lapse rate of T_v between 700 and 500 hPa height [K km ⁻¹]
Γ_d	Dry adiabatic lapse rate [K km ⁻¹]
γ_p	Parcel lapse rate (dry adiabatic) [K km ⁻¹]
Γ_s	Saturated adiabatic lapse rate [K km ⁻¹]
λ_{psy}	Psychometric constant [kPa K ⁻¹]
\bar{T}_0	Environmental temperature [K]
\bar{T}_v	Environmental virtual temperature [K]
Φ	Mixed layer θ stratification [K m ⁻¹]
Φ_0	Initial stratification of θ close to the land surface [K m ⁻¹]
Π	Exner function or $C_p T/\theta$
Ψ	A constant for the drag term in Equation 3.2
ρ	Density of air [kg m ⁻³]
σ_{dev}	Standard deviation [variable units]
$\vec{\psi}$	Horizontal wind divergence [s ⁻¹]

\vec{U}_{10m}	10 m horizontal wind vectors [m s^{-1}]
\vec{V}	Horizontal wind vector [m s^{-1}]
\vec{V}_G	Geostrophic wind - Balanced PGF and Coriolis forces whereby the winds flow parallel to straight isobars [m s^{-1}]
\vec{V}_g	Gradient wind - Deviation from geostrophic balance due to friction [m s^{-1}]
C_p	specific heat of dry air at constant pressure [$1004 \text{ J K}^{-1} \text{ kg}^{-1}$]
e_a	Actual water vapor pressure [hPa]
e_s	Saturated water vapor pressure [hPa]
F_{AW}	fractional root zone available water [-]
I_k	Layer irrigation term in Equation 2.2 [mm s^{-1}]
k	von Karman constant or ~ 0.41 [-]
L_v	Latent heat of vaporization at 100°C [$2.25 \times 10^6 \text{ J kg}^{-1}$]
P_D	Precipitation term in Equation 2.2 [mm s^{-1}]
R_a	Aerodynamic resistance [s m^{-1}]
R_d	Gas constant for dry air [$287 \text{ J K}^{-1} \text{ kg}^{-1}$]
R_s	Surface resistance [s m^{-1}]
T_v	Virtual temperature or $T'_v + \bar{T}_v$ [K]
U_{dir}	Measure wind direction [Degrees from true north]
z_0	Starting displacement height [m]
α	Albedo [-]
d	Displacement height [m]
AER	Anthropogenic Emissions Reduction
BECS	Bio-energy with Carbon Sequestration
Bowen ratio	The relation Q_H/Q_E [-]
C_D	Surface drag coefficient
CAPE	Convective available potential energy [J kg^{-1}]

CBL	Convective boundary layer
CCS	Carbon Capture and Sequestration
CDM	Clean Development Mechanism
CDR	Carbon Drawdown and Removal
CI	Convection initiation
CIN	Convective inhibition energy [J kg^{-1}]
CO ₂	Carbon dioxide
COV	Coefficient of Variation $\frac{\sigma_{dev}}{mean}$ [-]
D	Hydraulic diffusivity in Equation 2.2 [$\text{m}^2 \text{s}^{-1}$]
DMC	Deep moist convection
E_{dir}	direct evaporation from the surface [mm s^{-1}]
E_{ti}	Layer root uptake term in Equation 2.2 [mm s^{-1}]
ECMWF	European Centre for Medium Range Weather Forecasting
EL	Equilibrium level [m]
ET	Evapotranspiration [mm]
ET ₀	Reference or potential ET [mm t^{-1}]
ET _c	Crop evapotranspiration [mm]
ET _D	Direct soil evaporation [mm]
g	Gravitational acceleration [m s^{-2}]
GCM	General Circulation Model
h	PBL height [m]
h _c	Canopy height [m]
HCR	Horizontal convective roll
IBL	Internal boundary layer
ICV	Integrated column water vapor [mm]
ITCZ	Inter-tropical convergence zone

K	Soil hydraulic conductivity in Equation 2.2 [m s^{-1}]
K_c	Crop coefficient for Penman FAO 56 Equation [-]
L_S	Spatial length scale [km]
LAI	Leaf area index [$\text{m}^2 \text{m}^{-2}$]
LAI_{eff}	Effective leaf area index - usually LAI/2 [$\text{m}^2 \text{m}^{-2}$]
LCL	Lifting condensation level [m]
LES	Large Eddy Simulation
LFC	Level of free convection [m]
LLCJ	Low-level coastal jet
LSA	Large-Scale Afforestation
$\text{LW}\downarrow$	Downwelling long wave radiation at the surface [W m^{-2}]
$\text{LW}\uparrow$	Upwelling long wave radiation from the surface [W m^{-2}]
MCC	Mesoscale convective cell
MODIS	Moderate Resolution Imaging Spectroradiometer (IGBP) modified land surface data
NAM	North American Monsoon
NOAA	National Oceanic and Atmospheric Administration
P'	Pressure perturbation [hPa]
PBL	Planetary boundary layer
PET	Potential or reference evapotranspiration [mm]
PGF	Pressure gradient force [Pa m^{-1}]
PRD	Partial root zone drying
Q_G	Ground heat flux (W m^{-2})
$q_{v,s}$	Vapor mixing ratio at saturation [kg kg^{-1}]
q_v	Water vapor mixing ratio [g kg^{-1}]
Q_E	Latent heat flux [W m^{-2}]

Q_H	Sensible heat flux [W m^{-2}]
R	Runoff term in Equation 2.2 [mm s^{-1}]
r	Pearson correlation coefficient (0.95% confidence)[-]
R_N	Net radiation at the surface [W m^{-2}]
$R_{st,bulk}$	Bulk stomatal resistance [s m^{-1}]
$R_{st,min}$	Minimum stomatal resistance (parameter) [s m^{-1}]
R_{st}	Stomatal resistance [s m^{-1}]
RCM	Regional Climate Model
RCP	Representative Concentration Pathway
RH	Relative humidity [%]
RHS	Right hand side
SLP	Sea level pressure [hPa]
SRM	Solar Radiation Management
ST_{5cm}	soil temperature at 5cm depth [$^{\circ}\text{C}$]
SW_{\downarrow}	Downwelling short wave radiation at the surface [W m^{-2}]
SW_{\uparrow}	Upwelling short wave radiation from the surface [W m^{-2}]
T'	Temperature perturbation [K]
T_{2m}	2 m air temperature [K]
T'_v	virtual temperature [K]
TKE	Turbulence kinetic energy [J kg^{-1}]
U	Measured wind speed [m s^{-1}]
u	Horizontal wind component in the x direction [m s^{-1}]
u^*	Friction velocity [m s^{-1}]
UNCCD	United Nations Convention to Combat Desertification
UNFCCC	United Nations Framework Convention on Climate Change
v	Horizontal wind component in the y direction [m s^{-1}]

VPD Vapor pressure deficit [hPa]

w Vertical wind component in the z direction [m s^{-1}]

w_{max} Maximum vertical velocity [m s^{-1}]

WUE Water Use Efficiency

Z_{0m} Roughness length [m]

List of Figures

1.1	Global desert biomes	6
1.2	Climatology of Beer'sheva, Israel and Masirah, Oman	9
1.3	Albedo of Jojoba and Jatropha	15
1.4	Soil moisture feedbacks to the atmosphere	17
1.5	Schematic of thesis work flow	28
2.1	Topographic map of the eastern Mediterranean	32
2.2	Plantation configuration and location within MODIS land surface data set .	34
2.3	Photos of measurement sites at <i>Jojoba</i> and <i>Desert</i>	36
2.4	Comparison of simulated and observed T_{2m} , VPD and U variables	38
2.5	Comparison of simulated and observed R_N , Q_G , ST_{5cm} variables	39
2.6	Comparison of simulated and observed latent and sensible heat fluxes . . .	40
3.1	Model domains over Israel and Oman	46
3.2	Accumulated precipitation impact over Israel and Oman (24.06 to 31.07 2012)	48
3.3	Oman - daily precipitation over plantation and domain	49
3.4	Israel - daily precipitation over plantation and domain	50
3.5	Oman - classification of impacts	51
3.6	Israel - classification of impacts	52
3.7	Oman - impact frequency	53
3.8	Oman - pressure perturbation 30.06	54
3.9	Oman - evolution of Θ and q_v profile on 30.06	56
3.10	Oman - evolution of vertical velocity (w) from before to after CI on 30.06 .	58
3.11	Oman - maximum pressure perturbation and rainfall events	60
3.12	Oman - 38 day scatter plots and correlations of P' , $SW\downarrow$, $\vec{\psi}$, U , T'	61
3.13	Oman and Israel- mean thermodynamic profiles from 25.06 to 31.07	63
3.14	Oman grouped T_v and T_d profiles for wet and dry periods	65
3.15	Oman environment and impact 27-06 - strongly enhanced	67
3.16	Oman environment and impact 30-06 - moderately enhanced	68
3.17	Oman environment and impact 25-07 - strongly induced	69
3.18	Israel environment and impact 27-07 - weakly induced	70

3.19	Lateral boundary temperature forcings on 3 dry days - 600 hPa	71
3.20	Lateral boundary temperature forcings on 3 wet days - 600 hPa	72
4.1	Lapse rate, specific humidity and integrated column vapor - Africa and Asia	80
4.2	Africa stations - climatologies of lapse rate, humidity and precipitation . . .	82
4.3	Asia stations - climatologies of lapse rate, humidity and precipitation	84
4.4	Lapse rate, specific humidity and integrated column vapor - Americas	86
4.5	N. America stations - climatologies of lapse rate, humidity and precipitation	87
4.6	Lapse rate, specific humidity and integrated column vapor - Australasia . . .	88
4.7	Australia and S. America stations - climatologies of lapse rate, humidity and precipitation	89
6.1	Israel - observed summer daily mean, max and min of T_{2m} and RH	125
6.2	Israel - observed summer daily mean, max and min of T_{2m} and RH	126
6.3	Israel - observed summer daily means of R_N , U , U_{dir} and P	127
6.4	Israel - observed summer diurnal cycle of T_{2m} , RH, U_{6m} , R_N , Albedo and P	128
6.5	Israel - observed summer wind field statistics	129
6.6	Israel - mean daily maximum of sensible and latent heat flux in WRF Impact (over the 10×10 km plantation)	131
6.7	Africa - standard deviation (σ_{dev}) of $\Gamma_{700-500}$, $q_{s,925}$, ICV - 1979-2012 . . .	133
6.8	Americas - standard deviation (σ_{dev}) of $\Gamma_{700-500}$, $q_{s,925}$, ICV - 1979-2012 . .	134
6.9	Australia - standard deviation (σ_{dev}) of $\Gamma_{700-500}$, $q_{s,925}$, ICV - 1979-2012 . .	135
6.10	Africa - coefficient of variance for $\Gamma_{700-500}$, $q_{s,925}$, ICV - 1979-2012	136
6.11	Americas - coefficient of variance for $\Gamma_{700-500}$, $q_{s,925}$, ICV - 1979-2012 . . .	137
6.12	Australia - coefficient of variance for $\Gamma_{700-500}$, $q_{s,925}$, ICV - 1979-2012 . . .	138

List of Tables

2.1	Physics schemes used in WRF-NOAH and appropriate references	32
2.2	Vegetation parameters used for simulation of Jojoba plantation	34
2.3	Measured variables at <i>Desert</i> and <i>Jojoba</i> including error estimation.	36
2.4	Summary of maximum WRF-NOAH deviations from observations	41
3.1	Oman and Israel - selected wet and dry periods	50
4.1	Stations analyzed for potential arid agroforestry	79
4.2	Regional range of σ_{dev} - ERA-Interim 1979-2012	81
4.3	Regional range of coefficient of variance - ERA-Interim 1979-2012	81
6.1	Climate data source for global analysis	132

Bibliography

- Abou Kheira, A. and N. M. Atta (2009, October). Response of *Jatropha curcas* L. to water deficits: Yield, water use efficiency and oilseed characteristics. *Biomass and Bioenergy* 33(10), 1343–1350.
- Allen, R., L. Pereira, and D. Raes (1998). Crop evapotranspiration: Guidelines for computing crop water requirements. FAO Irrigation and Drainage Paper No. 56, Rome.
- Allen, R. G. (1998). FAO Irrigation and Drainage Paper Crop 56.
<http://www.fao.org/docrep/x0490e/x0490e00.htm>.
- Alpert, P. and M. Mandel (1986, November). Wind Variability - An Indicator for a Mesoclimatic Change in Israel. *Journal of Climate and Applied Meteorology* 25(11), 1568–1576.
- Ansari, M., K. Rana, D. Rana, and A. Kumar (2012). Effect of anti-transpirant and nutrient management on pearl millet (*Pennisetum glaucum*)-pigeonpea (*Cajanus cajan*) intercropping system under rainfed conditions. *Indian Journal of Agronomy* 57(4), 343–348.
- Avissar, R. and T. Schmidt (1998). An evaluation of the scale at which ground-surface heat flux patchiness affects the convective boundary layer using large-eddy simulations. *Journal of the Atmospheric Sciences* (1995), 2666–2689.
- Avissar, R. and D. Werth (2005). Global hydroclimatological teleconnections resulting from tropical deforestation. *Journal of Hydrometeorology* (1993), 134–145.
- Baidya Roy, S. (2003). A preferred scale for landscape forced mesoscale circulations? *Journal of Geophysical Research* 108(D22), 8854.
- Bauer, H.-S., T. Weusthoff, M. Dorninger, V. Wulfmeyer, T. Schwitalla, T. Gorgas, M. Arpagaus, and K. Warrach-Sagi (2011, January). Predictive skill of a subset of models participating in D-PHASE in the COPS region. *Quarterly Journal of the Royal Meteorological Society* 137(S1), 287–305.
- Becker, K., V. Wulfmeyer, T. Berger, J. Gebel, and W. Münch (2013, July). Carbon farming in hot, dry coastal areas: an option for climate change mitigation. *Earth System Dynamics* 4(2), 237–251.
- Bellamy, R., J. Chilvers, N. E. Vaughan, and T. M. Lenton (2012). A review of climate geoengineering appraisals. *Wiley Interdisciplinary Reviews: Climate Change* 3(6), 597–615.
- Ben-Gai, T., A. Bitan, A. Manes, and P. Alpert (1993). Long-term change in October rainfall patterns in southern Israel. *Theoretical and Applied Climatology* 46(4), 209–217.

- Ben-Gai, T., A. Bitan, A. Manes, and P. Alpert (1994). Long-term changes in annual rainfall patterns in southern Israel. *Theoretical and Applied Climatology* 49(2), 59–67.
- Ben-Gai, T., A. Bitan, A. Manes, P. Alpert, and S. Rubin (1998, December). Spatial and Temporal Changes in Rainfall Frequency Distribution Patterns in Israel. *Theoretical and Applied Climatology* 61(3-4), 177–190.
- Benzioni, A. (1995). Jojoba Domestication and Commercialization in Israel. In *Horticultural Reviews*, pp. 233–266. John Wiley & Sons, Inc.
- Benzioni, A. and R. L. Dunstone (1988, September). Effect of air and soil temperature on water balance of Jojoba growing under controlled conditions. *Physiologia Plantarum* 74(1), 107–112.
- Beringer, T., W. Lucht, and S. Schaphoff (2011, August). Bioenergy production potential of global biomass plantations under environmental and agricultural constraints. *GCB Bioenergy* 3(4), 299–312.
- Betts, R. (2007, July). Implications of land ecosystem-atmosphere interactions for strategies for climate change adaptation and mitigation. *Tellus B* 59(3), 602–615.
- Betts, R. A. (2000, November). Offset of the potential carbon sink from boreal forestation by decreases in surface albedo. *Nature* 408(6809), 187–90.
- Bird, D. N., M. Kunda, a. Mayer, B. Schlamadinger, L. Canella, and M. Johnston (2008, April). Incorporating changes in albedo in estimating the climate mitigation benefits of land use change projects. *Biogeosciences Discussions* 5(2), 1511–1543.
- Bonan, G. B. (2008). *Ecological climatology: concepts and applications*. Number Ed.2. Cambridge University Press.
- Boyd, P. W. (2008, October). Ranking geo-engineering schemes. *Nature Geoscience* 1(11), 722–724.
- Branch, O., K. Warrach-Sagi, V. Wulfmeyer, and S. Cohen (2014). Simulation of semi-arid biomass plantations and irrigation using the WRF-NOAH model - a comparison with observations from Israel. *Hydrology and Earth System Sciences* 18(5), 1761–1783.
- Brutsaert, W. (1982). *Evaporation Into the Atmosphere. Theory, History and Applications*. London: D. Reidel.
- Budyko, M. (1986). *The Evolution of the Biosphere*. Springer Netherlands.
- Carleton, A. M., D. J. Travis, J. O. Adegoke, D. L. Arnold, and S. Curran (2008, July). Synoptic Circulation and Land Surface Influences on Convection in the Midwest U.S. “Corn Belt” during the Summers of 1999 and 2000. Part I: Composite Synoptic Environments. *Journal of Climate* 21(14), 3389–3415.
- Charney, J. G. (1975, April). Dynamics of deserts and drought in the Sahel. *Quarterly Journal of the Royal Meteorological Society* 101(428), 193–202.

- Chen, F. and J. Dudhia (2001, April). Coupling an Advanced Land Surface Hydrology Model with the Penn State NCAR MM5 Modeling System. Part I: Model Implementation and Sensitivity. *Monthly Weather Review* 129(4), 569–585.
- Chen, F., K. Mitchell, J. Schaake, Y. Xue, H.-L. Pan, V. Koren, Q. Y. Duan, M. Ek, and A. Betts (1996, March). Modeling of land surface evaporation by four schemes and comparison with FIFE observations. *Journal of Geophysical Research* 101 (D3), 7251.
- Cook, B. I., M. J. Puma, and N. Y. Krakauer (2010, November). Irrigation induced surface cooling in the context of modern and increased greenhouse gas forcing. *Climate Dynamics* 37(7-8), 1587–1600.
- Costanza, R., R. D’Arge, R. de Groot, S. Farber, M. Grasso, B. Hannon, K. Limburg, S. Naeem, R. V. O’Neill, J. Paruelo, R. G. Raskin, P. Sutton, and M. van den Belt (1997, May). The value of the world’s ecosystem services and natural capital. *Nature* 387(6630), 253–260.
- Dalu, G. A., R. A. Pielke, M. Baldi, and X. Zeng (1996, November). Heat and Momentum Fluxes Induced by Thermal Inhomogeneities with and without Large-Scale Flow. *Journal of the Atmospheric Sciences* 53(22), 3286–3302.
- de Gorter, H., D. Drabik, D. R. Just, and E. M. Kliaugu (2013, July). The impact of OECD biofuels policies on developing countries. *Agricultural Economics* 44 (4-5), 477–486.
- Dee, D. P., S. M. Uppala, A. J. Simmons, P. Berrisford, P. Poli, S. Kobayashi, U. Andrae, M. A. Balmaseda, G. Balsamo, P. Bauer, P. Bechtold, A. C. M. Beljaars, L. van de Berg, J. Bidlot, N. Bormann, C. Delsol, R. Dragani, M. Fuentes, A. J. Geer, L. Haimberger, S. B. Healy, H. Hersbach, E. V. Hölm, L. Isaksen, P. Kållberg, M. Köhler, M. Matricardi, A. P. McNally, B. M. Monge-Sanz, J.-J. Morcrette, B.-K. Park, C. Peubey, P. de Rosnay, C. Tavolato, J.-N. Thépaut, and F. Vitart (2011, April). The ERA-Interim reanalysis: configuration and performance of the data assimilation system. *Quarterly Journal of the Royal Meteorological Society* 137(656), 553–597.
- Dixon, N. S., D. J. Parker, C. M. Taylor, L. Garcia-Carreras, P. P. Harris, J. H. Marsham, J. Polcher, and a. Woolley (2013, April). The effect of background wind on mesoscale circulations above variable soil moisture in the Sahel. *Quarterly Journal of the Royal Meteorological Society* 139(673), 1009–1024.
- D’Odorico, P., A. Bhattachan, K. F. Davis, S. Ravi, and C. W. Runyan (2013, January). Global desertification: Drivers and feedbacks. *Advances in Water Resources* 51, 326–344.
- Du, C., W. Wu, X. Liu, and W. Gao (2006, August). Simulation of Soil Moisture and Its Variability in East Asia. In W. Gao and S. L. Ustin (Eds.), *Society of Photo-Optical Instrumentation Engineers (SPIE) Conference Series*, Volume 6298, pp. 62982F–62982F–6.
- Dyer, A. J. and B. B. Hicks (1970, October). Flux-gradient relationships in the constant flux layer. *Quarterly Journal of the Royal Meteorological Society* 96 (410), 715–721.
- Eurostat (2014). Greenhouse gas emissions by country, 2000-2010.
- Evans, J. P. and B. F. Zaitchik (2008, August). Modeling the large-scale water balance impact of different irrigation systems. *Water Resources Research* 44 (8).

- Finnigan, J., R. Shaw, and E. Patton (2009). Turbulence structure above a vegetation canopy. *Journal of Fluid Mechanics* 637, 387–424.
- Frei, C. (2003). Daily precipitation statistics in regional climate models: Evaluation and intercomparison for the European Alps. *Journal of Geophysical Research* 108 (D3), 4124.
- Fritzmann, C., J. Löwenberg, T. Wintgens, and T. Melin (2007, October). State-of-the-art of reverse osmosis desalination. *Desalination* 216(1-3), 1–76.
- Fujita, T. T. (1981, August). Tornadoes and Downbursts in the Context of Generalized Planetary Scales. *Journal of the Atmospheric Sciences* 38(8), 1511–1534.
- Gao, Y., G. Yu Qiu, H. Shimizu, K. Tobe, B. Sun, and J. Wang (2002, December). A 10-Year Study on Techniques for Vegetation Restoration in a Desertified Salt Lake Area. *Journal of Arid Environments* 52(4), 483–497.
- Groner, V. (2013). The impact of a large scale plantation of *Jatropha curcas* L. on convection initiation under monsoonal conditions in the coastal desert of Oman. Master Thesis. University of Hohenheim. Institute of Physics and Meteorology.
- Hamilton, A. J., F. Stagnitti, X. Xiong, S. L. Kreidl, K. K. Benke, and P. Maher (2007, November). Wastewater Irrigation: The State of Play. *Vadose Zone Journal* 6(4), 823.
- Hargreaves, M. (1957). *Dry Farming in the Northern Great Plains: 1920-1990*. Cambridge: Harvard University Press.
- Hong, S.-Y., Y. Noh, and J. Dudhia (2006, September). A New Vertical Diffusion Package with an Explicit Treatment of Entrainment Processes. *Monthly Weather Review* 134(9), 2318–2341.
- Hong, X. (1995, August). Role of vegetation in generation of mesoscale circulation. *Atmospheric Environment* 29(16), 2163–2176.
- Hu, X.-M., J. W. Nielsen-Gammon, and F. Zhang (2010, September). Evaluation of Three Planetary Boundary Layer Schemes in the WRF Model. *Journal of Applied Meteorology and Climatology* 49(9), 1831–1844.
- Hulme, M. (2012, August). Climate change: Climate engineering through stratospheric aerosol injection. *Progress in Physical Geography* 36(5), 694–705.
- Hussain, G., M. Bashir, and M. Ahmad (2011). Brackish water impact on growth of jojoba (*Simmondsia chinensis*). *Journal of Agricultural Research* v. 49(4).
- Huzayyin, A., A. Bawady, M. Rady, and A. Dawood (2004, August). Experimental evaluation of Diesel engine performance and emission using blends of jojoba oil and Diesel fuel. *Energy Conversion and Management* 45(13-14), 2093–2112.
- Iacono, M., J. Delamere, E. Mlawer, M. Shephard, S. Clough, and W. Collins (2008, July). Radiative forcing by long-lived greenhouse gases: Calculations with the AER radiative transfer models. *Journal of Geophysical Research* 113(D13), D13103.

- IPCC (2012). Meeting Report of the Intergovernmental Panel on Climate Change Expert Meeting on Geoengineering [O. Edenhofer, R. Pichs-Madruga, Y. Sokona, C. Field, V. Barros, T.F. Stocker, Q. Dahe, J. Minx, K. Mach, G.-K. Plattner, S. Schlömer, G. Hansen, M. Mastrandr. Technical report.
- IPCC (2013). Summary for Policymakers: Climate Change 2013: The Physical Science Basis. Contribution of Working Group I to the Fifth Assessment Report of the Intergovernmental Panel on Climate Change [Stocker T.F., D. Qin, G.-K. Plattner, M. Tignor, S.K.A. Technical report, Cambridge University Press, Cambridge, United Kingdom and New York, NY, USA., Cambridge.
- Izrael, Y. A., A. G. Ryaboshapko, and N. N. Petrov (2009, August). Comparative analysis of geo-engineering approaches to climate stabilization. *Russian Meteorology and Hydrology* 34(6), 335–347.
- Jacquemin, B. and J. Noilhan (1990, July). Sensitivity study and validation of a land surface parameterization using the HAPEX-MOBILHY data set. *Boundary-Layer Meteorology* 52(1-2), 93–134.
- Justice, C., J. Townshend, E. Vermote, E. Masuoka, R. Wolfe, N. Saleous, D. Roy, and J. Morisette (2002, November). An overview of MODIS Land data processing and product status. *Remote Sensing of Environment* 83(1-2), 3–15.
- Kéfi, S., M. Rietkerk, C. L. Alados, Y. Pueyo, V. P. Papanastasis, A. Elaich, and P. C. de Ruiter (2007, September). Spatial vegetation patterns and imminent desertification in Mediterranean arid ecosystems. *Nature* 449(7159), 213–7.
- Keith, D. W., M. Ha-Duong, and J. K. Stolaroff (2005, December). Climate Strategy with CO₂ Capture from the Air. *Climatic Change* 74(1-3), 17–45.
- Khawaji, A. D., I. K. Kutubkhanah, and J.-M. Wie (2008, March). Advances in seawater desalination technologies. *Desalination* 221(1-3), 47–69.
- Köppen, W. (1931). *Grundriss der Klimatkunde. Zweite, verbesserte Auflage der Klimate der Erde*. Walter de Gruyter und Company.
- Kreith, F., A. Taori, and J. E. Anderson (1975, April). Persistence of selected antitranspirants. *Water Resources Research* 11(2), 281–286.
- Kumar, K. K., B. Rajagopalan, M. Hoerling, G. Bates, and M. Cane (2006, October). Unraveling the mystery of Indian monsoon failure during El Niño . *Science (New York, N.Y.)* 314(5796), 115–9.
- Lal, R. (2005, December). Forest soils and carbon sequestration. *Forest Ecology and Management* 220(1-3), 242–258.
- Lam, D. K., T. K. Rimmel, and T. D. Drezner (2010, December). Tracking Desertification in California Using Remote Sensing: A Sand Dune Encroachment Approach. *Remote Sensing* 3(1), 1–13.
- Lee, S.-H. and F. Kimura (2001, November). Comparative Studies In The Local Circulations Induced By Land-Use And By Topography. *Boundary-Layer Meteorology* 101(2), 157–182.

- Lenton, T. and N. Vaughan (Eds.) (2013). *Geoengineering Responses to Climate Change*. New York, NY: Springer New York.
- Lenton, T. M. and N. E. Vaughan (2009, January). The radiative forcing potential of different climate geoengineering options. *Atmospheric Chemistry and Physics Discussions* 9(1), 2559–2608.
- Letzel, M. O. and S. Raasch (2003, September). Large Eddy Simulation of Thermally Induced Oscillations in the Convective Boundary Layer. *Journal of the Atmospheric Sciences* 60(18), 2328–2341.
- Lim, Y.-J., J. Hong, and T.-Y. Lee (2012, September). Spin-up behavior of soil moisture content over East Asia in a land surface model. *Meteorology and Atmospheric Physics* 118(3-4), 151–161.
- Lobell, D., G. Bala, A. Mirin, T. Phillips, R. Maxwell, and D. Rotman (2009, April). Regional Differences in the Influence of Irrigation on Climate. *Journal of Climate* 22(8), 2248–2255.
- Lorenz, K. and R. Lal (2009). *Carbon Sequestration in Forest Ecosystems*(Google eBook). Springer.
- Ludwig, N., R. Cabrini, F. Faoro, M. Gargano, S. Gomasasca, M. Iriti, V. Picchi, and C. Soave (2010, January). Reduction of evaporative flux in bean leaves due to chitosan treatment assessed by infrared thermography. *Infrared Physics & Technology* 53(1), 65–70.
- Lynn, B. H., D. Rind, and R. Avissar (1995, February). The Importance of Mesoscale Circulations Generated by Subgrid-Scale Landscape Heterogeneities in General Circulation Models. *Journal of Climate* 8(2), 191–205.
- Mahfouf, J.-F., E. Richard, and P. Mascart (1987, November). The Influence of Soil and Vegetation on the Development of Mesoscale Circulations. *Journal of Climate and Applied Meteorology* 26(11), 1483–1495.
- Mahmood, R., R. a. Pielke, K. G. Hubbard, D. Niyogi, P. a. Dirmeyer, C. McAlpine, A. M. Carleton, R. Hale, S. Gameda, A. Beltrán-Przekurat, B. Baker, R. McNider, D. R. Legates, M. Shepherd, J. Du, P. D. Blanken, O. W. Frauenfeld, U. Nair, and S. Fall (2013, June). Land cover changes and their biogeophysical effects on climate. *International Journal of Climatology*.
- Mahrt, L. and M. Ek (1984, February). The Influence of Atmospheric Stability on Potential Evaporation. *Journal of Climate and Applied Meteorology* 23(2), 222–234.
- Mahrt, L. and H. Pan (1984, May). A two-layer model of soil hydrology. *Boundary-Layer Meteorology* 29(1), 1–20.
- Mahrt, L., J. Sun, and D. Vickers (1994). Observations of fluxes and inland breezes over a heterogeneous surface. *Journal of the Atmospheric Sciences* 51(17).
- Markowski, P. M. and Y. P. Richardson (2010). *Mesoscale Meteorology in Midlatitudes*. John Wiley & Sons.

- McPherson, R. A. (2007, June). A review of vegetation–atmosphere interactions and their influences on mesoscale phenomena. *Progress in Physical Geography* 31(3), 261–285.
- Meigs, P. (1953). World Distribution of Arid and Semi-arid Homoclimates. In, UNESCO, Reviews of Research on Arid Zone Hydrology, Paris: United Nations.
- Mlawer, E. J., S. J. Taubman, P. D. Brown, M. J. Iacono, and S. A. Clough (1997, July). Radiative transfer for inhomogeneous atmospheres: RRTM, a validated correlated-k model for the longwave. *Journal of Geophysical Research* 102(D14), 16663.
- Moeng, C.-H., J. Dudhia, J. Klemp, and P. Sullivan (2007, June). Examining Two-Way Grid Nesting for Large Eddy Simulation of the PBL Using the WRF Model. *Monthly Weather Review* 135(6), 2295–2311.
- Molthan, A. L. and B. A. Colle (2012, May). Comparisons of Single- and Double-Moment Microphysics Schemes in the Simulation of a Synoptic-Scale Snowfall Event. *Monthly Weather Review* 140(9), 2982–3002.
- Montagnini, F. and P. Nair (2004). Carbon sequestration: an underexploited environmental benefit of agroforestry systems. *Agroforestry Systems*, 281–295.
- Monteith, J. (1965). Evaporation and environment. 19th Symposia of the Society for Experimental Biology. University Press, Cambridge, 205-234.
- Monteith, J. and M. Unsworth (1990). *Principles of Environmental Physics. Second Edition.* London: Arnold.
- Morrison, H. and A. Gettelman (2008, August). A New Two-Moment Bulk Stratiform Cloud Microphysics Scheme in the Community Atmosphere Model, Version 3 (CAM3). Part I: Description and Numerical Tests. *Journal of Climate* 21(15), 3642–3659.
- Mueller, E. N., J. Wainwright, A. J. Parsons, and L. Turnbull (2014). *Patterns of Land Degradation in Drylands.* Dordrecht: Springer Netherlands.
- Niu, G., D. Rodriguez, M. Mendoza, J. Jifon, and G. Ganjegunte (2012). Responses of *Jatropha curcas* to Salt and Drought Stresses. *International Journal of Agronomy* 2012, 1–7.
- Niu, G.-Y., Z.-L. Yang, K. E. Mitchell, F. Chen, M. B. Ek, M. Barlage, A. Kumar, K. Manning, D. Niyogi, E. Rosero, M. Tewari, and Y. Xia (2011, June). The community Noah land surface model with multiparameterization options (Noah-MP): 1. Model description and evaluation with local-scale measurements. *Journal of Geophysical Research* 116(D12), 1–19.
- Ogburn, M. and E. Edwards (2010). The Ecological Water-Use Strategies of Succulent Plants. *Advances in Botanical Research - ADVAN BOTAN RES* 55, 179 – 225.
- Ookouchi, Y., M. Segal, R. C. Kessler, and R. A. Pielke (1984, November). Evaluation of Soil Moisture Effects on the Generation and Modification of Mesoscale Circulations. *Monthly Weather Review* 112(11), 2281–2292.
- Openshaw, K. (2000). A review of *Jatropha curcas*: an oil plant of unfulfilled promise. *Biomass and Bioenergy* 19(1), 1–15.

- Orlanski, I. (1975). A rational subdivision of scales for atmospheric processes. *Bulletin of the American Meteorological Society* 56, 527 – 530.
- Oron, G., C. Campos, L. Gillerman, and M. Salgot (1999, January). Wastewater treatment, renovation and reuse for agricultural irrigation in small communities. *Agricultural Water Management* 38(3), 223–234.
- Otterman, J. (1989). Enhancement of surface-atmosphere fluxes by desert-fringe vegetation through reduction of surface albedo and of soil heat flux. *Theoretical and Applied Climatology* 40(1-2), 67–79.
- Otterman, J., A. Manes, S. Rubin, P. Alpert, and D. O. Starr (1990, December). An increase of early rains in Southern Israel following land-use change. *Boundary-Layer Meteorology* 53(4), 333–351.
- Ozdogan, M. and M. Rodell (2010). Simulating the effects of irrigation over the United States in a land surface model based on satellite-derived agricultural data. *Journal of Hydrometeorology* (April).
- Pal Arya, S. (2001). *Introduction to Micrometeorology*. Academic Press.
- Palmer, J. R. (2014). Biofuels and the politics of land-use change: tracing the interactions of discourse and place in European policy making. *Environment and Planning A* 46(2), 337–352.
- Pan, H.-L. and L. Mahrt (1987, January). Interaction between soil hydrology and boundary-layer development. *Boundary-Layer Meteorology* 38(1-2), 185–202.
- Parish, T. R. (2000, December). Forcing of the Summertime Low-Level Jet along the California Coast. *Journal of Applied Meteorology* 39(12), 2421–2433.
- Paulson, C. A. (1970, December). The Mathematical Representation of Wind Speed and Temperature Profiles in the Unstable Atmospheric Surface Layer. *Journal of Applied Meteorology* 9(6), 857–861.
- Penman, H. L. (1948, April). Natural Evaporation from Open Water, Bare Soil and Grass. *Proceedings of the Royal Society A: Mathematical, Physical and Engineering Sciences* 193(1032), 120–145.
- Perlin, N. and P. Alpert (2001). Effects of land use modification on potential increase of convection: A numerical mesoscale study over south Israel. *Journal of Geophysical Research* 106(D19), 22,621–22,634.
- Peterson, T., C. Folland, G. Gruza, W. Hogg, A. Mokssit, and N. Plummer (2001). Report on the activities of the working group on climate change detection and related rapporteurs 1998–2001. WMO-TD 1071, World Meteorological Organisation Report WCDMP-47, Geneva, Switzerland. Technical report.
- Pielke, R., J. Adegoke, A. Beltrán-Przekurat, C. Hiemstra, J. Lin, U. Nair, D. Niyogi, and T. Nobis (2007, July). An overview of regional land-use and land-cover impacts on rainfall. *Tellus B* 59(3), 587–601.

- Pielke, R., A. Pitman, D. Niyogi, R. Mahmood, C. McAlpine, F. Hossain, K. K. Goldewijk, U. Nair, R. Betts, S. Fall, M. Reichstein, P. Kabat, and N. de Noblet (2011, November). Land use/land cover changes and climate: modeling analysis and observational evidence. *Wiley Interdisciplinary Reviews: Climate Change* 2(6), 828–850.
- Pielke, R. A. (2002). *Mesoscale meteorological modelling* (2nd ed.). Academic Press.
- Pielke, R. A., G. A. Dalu, J. S. Snook, T. J. Lee, and T. G. F. Kittel (1991, November). Nonlinear Influence of Mesoscale Land Use on Weather and Climate. *Journal of Climate* 4(11), 1053–1069.
- Portnov, B. and U. Safriel (2004, March). Combating desertification in the Negev: dryland agriculture vs. dryland urbanization. *Journal of Arid Environments* 56(4), 659–680.
- Potter, C., S. Klooster, M. Steinbach, P. Tan, V. Kumar, S. Shekhar, and C. R. de Carvalho (2004, May). Understanding global teleconnections of climate to regional model estimates of Amazon ecosystem carbon fluxes. *Global Change Biology* 10(5), 693–703.
- Puigdefábregas, J. and T. Mendizabal (1998, June). Perspectives on desertification: western Mediterranean. *Journal of Arid Environments* 39(2), 209–224.
- Qian, Y., M. Huang, B. Yang, and L. K. Berg (2013, June). A Modeling Study of Irrigation Effects on Surface Fluxes and Land–Air–Cloud Interactions in the Southern Great Plains. *Journal of Hydrometeorology* 14(3), 700–721.
- Rajaona, A., H. Brueck, and F. Asch (2013, April). Leaf Gas Exchange Characteristics of *Jatropha* as Affected by Nitrogen Supply, Leaf Age and Atmospheric Vapour Pressure Deficit. *Journal of Agronomy and Crop Science* 199(2), 144–153.
- Rajaona, A., H. Brueck, C. Seckinger, and F. Asch (2012, December). Effect of salinity on canopy water vapor conductance of young and 3-year old *Jatropha curcas* L. *J. Arid Environ.* 87, 35–41.
- Ramankutty, N., C. Delire, and P. Snyder (2006, November). Feedbacks between agriculture and climate: An illustration of the potential unintended consequences of human land use activities. *Global and Planetary Change* 54(1-2), 79–93.
- Ranjha, M. R. (2013). *Global Climatology and Regional Modeling of Coastal Low-Level Jets*. Ph. D. thesis, Stockholm University, Faculty of Science, Department of Meteorology.
- Ranjha, R., G. Svensson, M. Tjernström, and A. Semedo (2013, August). Global distribution and seasonal variability of coastal low-level jets derived from ERA-Interim reanalysis. *Tellus A* 65.
- Rao, P. H. V. V., E. Amminedu, and R. V. R. Rao (2000, December). Spectral responses of jojoba under salinity stress. *Journal of the Indian Society of Remote Sensing* 28(4), 281–291.
- Raupach, M. and J. Finnigan (1996). Coherent eddies and turbulence in vegetation canopies: the mixing-layer analogy. *Boundary-Layer Meteorology*, 351–382.
- Ridder, K. D. and H. Gallée (1998). Land surface-induced regional climate change in southern Israel. *Journal of applied meteorology* 37(1993), 1470–1485.

- Rotach, M. W., P. Ambrosetti, C. Appenzeller, M. Arpagaus, L. Fontannaz, F. Fundel, U. Germann, A. Hering, M. A. Liniger, M. Stoll, A. Walser, F. Ament, H.-S. Bauer, A. Behrendt, V. Wulfmeyer, F. Bouttier, Y. Seity, A. Buzzi, S. Davolio, M. Corazza, M. Denhard, M. Dorninger, T. Gorgas, J. Frick, C. Hegg, M. Zappa, C. Keil, H. Volkert, C. Marsigli, A. Montaini, R. McTaggart-Cowan, K. Mylne, R. Ranzi, E. Richard, A. Rossa, D. Santos-Muñoz, C. Schär, M. Staudinger, Y. Wang, and J. Werhahn (2009a, September). MAP D-PHASE: Real-Time Demonstration of Weather Forecast Quality in the Alpine Region. *Bulletin of the American Meteorological Society* 90(9), 1321–1336.
- Rotach, M. W., P. Ambrosetti, C. Appenzeller, M. Arpagaus, L. Fontannaz, F. Fundel, U. Germann, A. Hering, M. A. Liniger, M. Stoll, A. Walser, F. Ament, H.-S. Bauer, A. Behrendt, V. Wulfmeyer, F. Bouttier, Y. Seity, A. Buzzi, S. Davolio, M. Corazza, M. Denhard, M. Dorninger, T. Gorgas, J. Frick, C. Hegg, M. Zappa, C. Keil, H. Volkert, C. Marsigli, A. Montaini, R. McTaggart-Cowan, K. Mylne, R. Ranzi, E. Richard, A. Rossa, D. Santos-Muñoz, C. Schär, M. Staudinger, Y. Wang, and J. Werhahn (2010b, February). MAP D-PHASE: Real-Time Demonstration of Weather Forecast Quality in the Alpine Region.
- Rotenberg, E. and D. Yakir (2010, January). Contribution of semi-arid forests to the climate system. *Science (New York, N.Y.)* 327(5964), 451–4.
- Rowland, J. R. J. (1993). *Dryland farming in Africa*. MacMillan.
- Royal Society (2009). Geoengineering the climate: science, governance and uncertainty. Report 10/09, 2009, 82 pp. Technical report.
- Saaroni, H., A. Bitan, E. B. Dor, and N. Feller (2004, July). The mixed results concerning the ‘oasis effect’ in a rural settlement in the Negev Desert, Israel. *Journal of Arid Environments* 58(2), 235–248.
- Schwitalla, T., H.-S. Bauer, V. Wulfmeyer, and G. Zängl (2008, December). Systematic errors of QPF in low-mountain regions as revealed by MM5 simulations. *Meteorologische Zeitschrift* 17(6), 903–919.
- Segal, M. and R. W. Arritt (1992, October). Nonclassical Mesoscale Circulations Caused by Surface Sensible Heat-Flux Gradients. *Bulletin of the American Meteorological Society* 73(10), 1593–1604.
- Seneviratne, S. I., T. Corti, E. L. Davin, M. Hirschi, E. B. Jaeger, I. Lehner, B. Orlowsky, and A. J. Teuling (2010, May). Investigating soil moisture–climate interactions in a changing climate: A review. *Earth-Science Reviews* 99(3–4), 125–161.
- Seneviratne, S. I. and R. D. Koster (2012, February). A Revised Framework for Analyzing Soil Moisture Memory in Climate Data: Derivation and Interpretation. *Journal of Hydrometeorology* 13(1), 404–412.
- SEPASAL (2010). Survey of Economic Plants for Arid and Semi-Arid Lands. <http://www.kew.org/science-conservation/research-data/science-directory/projects/survey-economic-plants-arid-and-semi>.
- Shepherd, J. (2009, September). Geoengineering the climate: science, governance and uncertainty. The Royal Society. <http://royalsociety.org/policy/publications/2009/geoengineering-climate/>.

- Shin, H. H. and S.-Y. Hong (2011, January). Intercomparison of Planetary Boundary-Layer Parametrizations in the WRF Model for a Single Day from CASES-99. *Boundary-Layer Meteorology* 139(2), 261–281.
- Shinohara, T. and D. I. Leskovar (2014, January). Effects of ABA antitranspirants, heat and drought stress on plant growth, physiology and water status of artichoke transplants. *Scientia Horticulturae* 165, 225–234.
- Silva, E., R. Ribeiro, S. Ferreira-Silva, R. Viégas, and J. Silveira (2010, October). Comparative effects of salinity and water stress on photosynthesis, water relations and growth of *Jatropha curcas* plants. *Journal of Arid Environments* 74(10), 1130–1137.
- Sinclair, T. R., C. B. Tanner, and J. M. Bennett (1984, January). Water-Use Efficiency in Crop Production. *BioScience* 34(1), 36–40.
- Skamarock, W. C., J. B. Klemp, J. Dudhia, D. O. Gill, D. M. Barker, W. Wang, and J. G. Powers (2005, June). A Description of the Advanced Research WRF Version 2.
- Söderberg, S. and M. Tjernström (2001, August). Supercritical channel flow in the coastal atmospheric boundary layer: Idealized numerical simulations. *Journal of Geophysical Research* 106(D16), 17811.
- Spreer, W., M. Nagle, S. Neidhart, R. Carle, S. Ongprasert, J. Müller, and J. Müller (2007, March). Effect of regulated deficit irrigation and partial rootzone drying on the quality of mango fruits (*Mangifera indica* L., cv. ‘Chok Anan’). *Agricultural Water Management* 88(1-3), 173–180.
- Sridhar, V. (2013). Tracking the Influence of Irrigation on Land Surface Fluxes and Boundary Layer Climatology. *Journal Of Contemporary Water Research & Education* (152), 79–93.
- Steen, M. and D. Reed (2004). Knowledge reference for national forest assessments - modeling for estimation and monitoring.
- Stohlgren, T. J., T. N. Chase, R. A. Pielke, . Sr, T. G. F. Kittel, and J. S. Baron (1998, June). Evidence that local land use practices influence regional climate, vegetation, and stream flow patterns in adjacent natural areas. *Global Change Biology* 4(5), 495–504.
- Talbot, C., E. Bou-Zeid, and J. Smith (2012, October). Nested Mesoscale Large-Eddy Simulations with WRF: Performance in Real Test Cases. *Journal of Hydrometeorology* 13(5), 1421–1441.
- Taylor, G. I. (1916, January). Skin Friction of the Wind on the Earth’s Surface. *Proceedings of the Royal Society A: Mathematical, Physical and Engineering Sciences* 92(637), 196–199.
- Thorntwaite, C. (1948). An Approach to a Rational Classification of Climate. *Geographical Review*, v. 38, no. 1, p. 55-94.
- Torres, A. B., R. Marchant, J. C. Lovett, J. C. Smart, and R. Tipper (2010, January). Analysis of the carbon sequestration costs of afforestation and reforestation agroforestry practices and the use of cost curves to evaluate their potential for implementation of climate change mitigation. *Ecological Economics* 69(3), 469–477.

- Trapp, R. (2013). *Mesoscale-Convective Processes in the Atmosphere*. New York: Cambridge University Press.
- Trier, S. (2003). Convective Storms: Convection Initiation. In *Encyclopedia of Atmospheric Sciences*, pp. 560–570. Academic Press.
- UN (1977). World Map of Desertification. United Nations Conference on Desertification, Nairobi, Kenya, 29 August–9 September 1977, UN Document A/CONF.74/2. 1978: United Nations Conference on Desertification: Roundup, Plan of Action and Resolutions, United Nations.
- UN (2012). Economic and World Population Prospects The 2012 Revision.
<http://esa.un.org/wpp/>.
- UN (2014). United Nations Decade for Deserts and the Fight against Desertification.
http://www.un.org/en/events/desertification_decade/whynow.shtml.
- UNCCD (1994). United Nations Convention to Combat Desertification, Intergovernmental Negotiating Committee For a Convention to Combat Desertification, Elaboration of an International Convention to Combat Desertification in Countries Experiencing Serious Drought and/or Des.
- Unland, H. E., P. R. Houser, W. J. Shuttleworth, and Z.-L. Yang (1996, December). Surface flux measurement and modeling at a semi-arid Sonoran Desert site. *Agricultural and Forest Meteorology* 82(1-4), 119–153.
- van Heerwaarden, C. C., J. Vilà-Guerau de Arellano, A. F. Moene, and A. A. M. Holtslag (2009, July). Interactions between dry-air entrainment, surface evaporation and convective boundary-layer development. *Quarterly Journal of the Royal Meteorological Society* 135 (642), 1277–1291.
- Vuuren, D. P., E. Stehfest, M. G. J. Elzen, T. Kram, J. Vliet, S. Deetman, M. Isaac, K. Klein Goldewijk, A. Hof, A. Mendoza Beltran, R. Oostenrijk, and B. Ruijven (2011, August). RCP2.6: exploring the possibility to keep global mean temperature increase below 2C. *Climatic Change* 109(1-2), 95–116.
- Wallace, J. and P. Hobbs (2006). *Atmospheric Science, Second Edition: An Introductory Survey (International Geophysics)*. Academic Press.
- Wang, Y., S. Basu, and L. Manuel (2013, July). Coupled Mesoscale-Large-Eddy Modeling of Realistic Stable Boundary Layer Turbulence.
- Warner, T. (2006, October). Desert Meteorology, Thomas T. Warner, Cambridge University Press, Cambridge, UK, 2004. 595 Pages. Hardback. ISBN 0-521-81798-6. *International Journal of Climatology* 26(12), 1737–1738.
- Warrach-Sagi, K., T. Schwitalla, V. Wulfmeyer, and H.-S. Bauer (2013, March). Evaluation of a climate simulation in Europe based on the WRF–NOAH model system: precipitation in Germany. *Climate Dynamics*.
- Weaver, C. (2004a). Coupling between large-scale atmospheric processes and mesoscale land-atmosphere interactions in the US Southern Great Plains during summer. Part I: Case. *Journal of Hydrometeorology*, 1223–1246.

- Weaver, C. (2004b). Coupling between large-scale atmospheric processes and mesoscale land-atmosphere interactions in the US Southern Great Plains during summer. Part II: Mean Impacts of the Mesoscale. *Journal of Hydrometeorology*, 1223–1246.
- Weusthoff, T., F. Ament, M. Arpagaus, and M. W. Rotach (2010, September). Assessing the Benefits of Convection-Permitting Models by Neighborhood Verification: Examples from MAP D-PHASE. *Monthly Weather Review* 138(9), 3418–3433.
- WMO (2008). Guide to Meteorological Instruments and Methods of Observation. Technical report.
- Wood, R., S. Gardiner, and L. Hartzell-Nichols (2013, November). Climatic change special issue: geoenvironmental research and its limitations. *Climatic Change* 121(3), 427–430.
- Wu, W. and R. Dickinson (2004). Time Scales of Layered Soil Moisture Memory in the Context of Land Atmosphere Interaction. *Journal of Climate* 17(14), 2752 – 2764.
- Wulfmeyer, V., A. Behrendt, H. Bauer, C. Kottmeier, U. Corsmeier, A. Blyth, G. Craig, U. Schumann, M. Hagen, S. Crewell, P. Di Girolamo, C. Flamant, M. Miller, A. Montani, S. Mobbs, E. Richard, M. Rotach, M. Arpagaus, H. Russchenberg, P. Schlüssel, M. König, V. Gärtner, R. Steinacker, M. Dorninger, D. Turner, T. Weckwerth, A. Hense, and C. Simmer (2008). The Convective and Orographically-induced Precipitation Study: A Research and Development Project of the World Weather Research Program for improving quantitative precipitation forecasting in low-mountain regions. *Bull Amer Meteorol Soc* 89(10), 1477–1486.
- Wulfmeyer, V., A. Behrendt, C. Kottmeier, U. Corsmeier, C. Barthlott, G. C. Craig, M. Hagen, D. Althausen, F. Aoshima, M. Arpagaus, H.-S. Bauer, L. Bennett, A. Blyth, C. Brandau, C. Champollion, S. Crewell, G. Dick, P. Di Girolamo, M. Dorninger, Y. Dufournet, R. Eigenmann, R. Engelmann, C. Flamant, T. Foken, T. Gorgas, M. Grzeschik, J. Handwerker, C. Hauck, H. Höller, W. Junkermann, N. Kalthoff, C. Kiemle, S. Klink, M. König, L. Krauss, C. N. Long, F. Madonna, S. Mobbs, B. Neininger, S. Pal, G. Peters, G. Pigeon, E. Richard, M. W. Rotach, H. Russchenberg, T. Schwitalla, V. Smith, R. Steinacker, J. Trentmann, D. D. Turner, J. van Baelen, S. Vogt, H. Volkert, T. Weckwerth, H. Wernli, A. Wieser, and M. Wirth (2011, January). The Convective and Orographically-induced Precipitation Study (COPS): the scientific strategy, the field phase, and research highlights. *Quarterly Journal of the Royal Meteorological Society* 137(S1), 3–30.
- Wulfmeyer, V., O. Branch, K. Warrach-Sagi, H.-S. Bauer, T. Schwitalla, and K. Becker (2014, January). The impact of plantations on weather and climate in coastal desert regions. *Journal of Applied Meteorology and Climatology*, 140117143424003.
- Xie, K., X.-X. Wang, R. Zhang, X. Gong, S. Zhang, V. Mares, C. Gavilán, A. Posadas, and R. Quiroz (2012, February). Partial root-zone drying irrigation and water utilization efficiency by the potato crop in semi-arid regions in China. *Scientia Horticulturae* 134, 20–25.
- Xu, L., S. Raman, and R. V. Madala (1995, December). A review of non-hydrostatic numerical models for the atmosphere. pp. 3595–3609.

Chapter 6

Appendices

6.1 Israel summer of 2012 observations

The following plots are the summer observed statistics for measured variables during summer 2012 (JJA) at 3 meteorological stations at Kibbutz Hatzerim near Beer'sheva, Israel. The stations are named: *Desert*, *Jatropha* and *Jajoba* (See Figure 6.1 below for location). See Table 2.3 in Chapter 2 for details on measurement and sensor data.

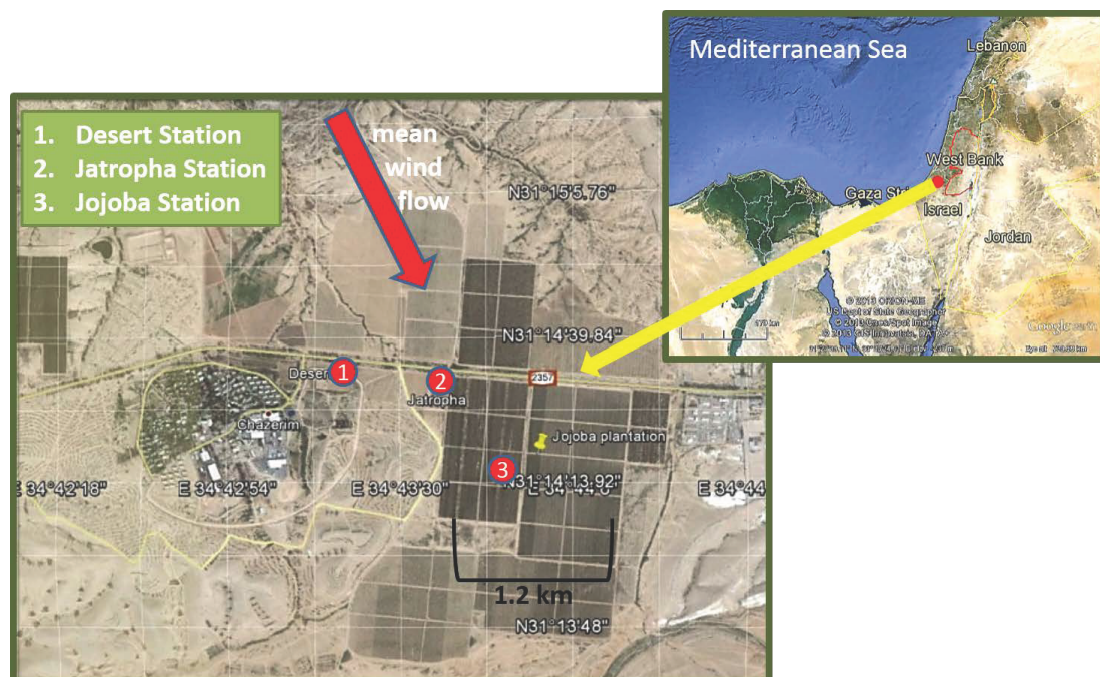


Figure 6.1: - The location of meteorological stations (left): *Desert* (1), *Jatropha* (2) and *Jojoba* (3) stations at Kibbutz Hatzerim close to Beer'sheva city, central Israel which is 40 km from the eastern Mediterranean coast (31.24°N , 34.72°E). The regional position is indicated in the inset box and mean wind flow is marked with an arrow. *Desert*, marked (1), is located on a bare, desert sandy-loam Loess soil with no vegetation. *Jatropha* (2) is in a 2 ha irrigated *Jatropha curcas* plantation (canopy height $h \sim 5$ m). *Jojoba* (3) is in a 400 ha plantation of irrigated *Jojoba* ($h = 3 - 3.5$ m).

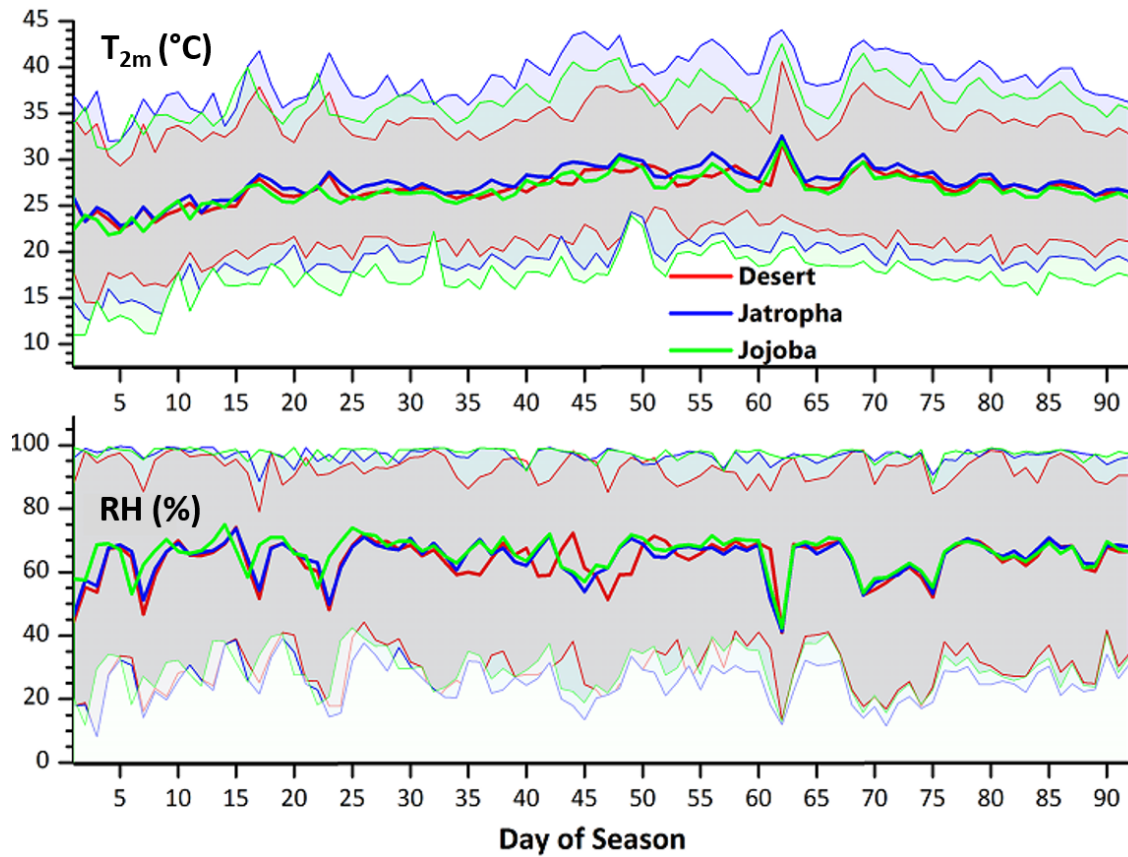


Figure 6.2: Observed daily mean, maxima and minima of T_{2m} [$^{\circ}\text{C}$] and relative humidity (%) for the Desert, Jatropha and Jojoba stations - summer 2012 (JJA). The thick curves at the center of the shaded areas are the daily mean values. The upper and lower thin lines bounding the shaded areas are the daily maxima and minima.

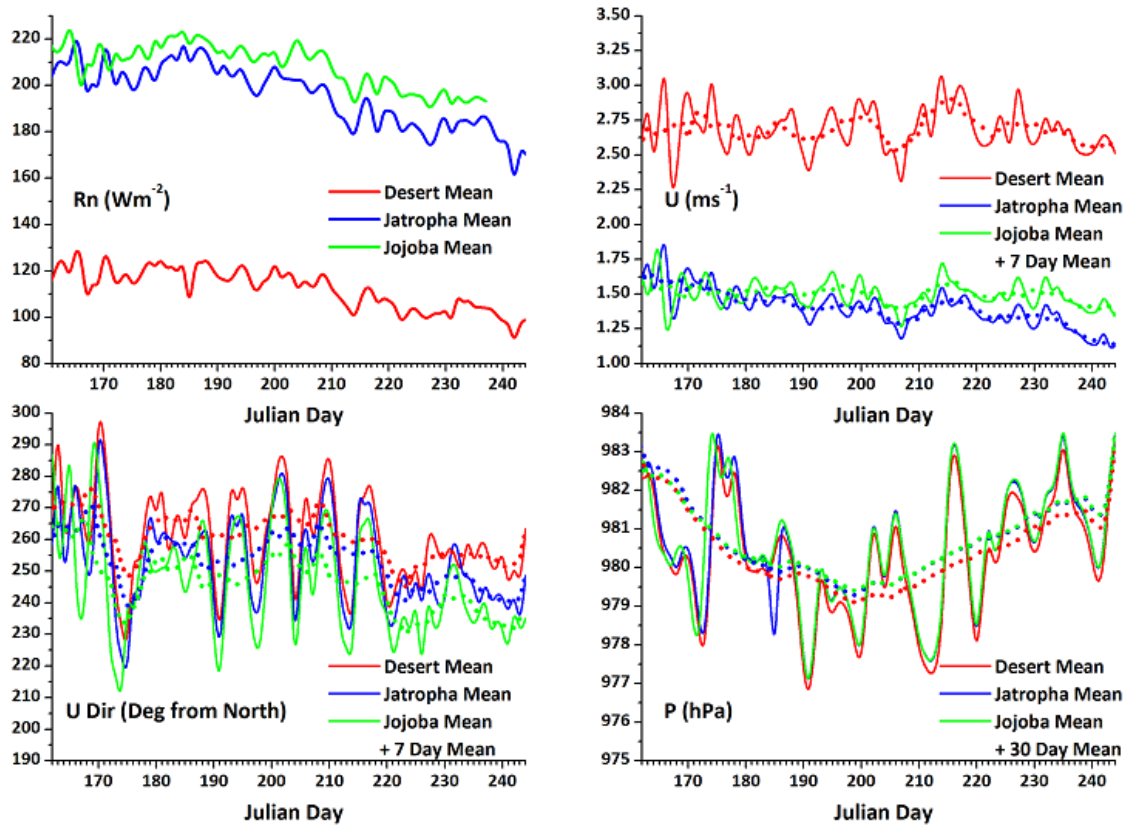


Figure 6.3: Observed daily 24 hour mean values of R_N [$W m^{-2}$], U [$m s^{-1}$], U direction [$^{\circ}$ from north] and P [hPa] for summer 2012 (JJA). 7 or 30 day means are plotted for U , U_{dir} and P based on peak analysis to highlight differences between the stations, and also the evolution of the summer climate. Due to poor quality flags, Jojoba R_N data was rejected for the last 8 days of the season.

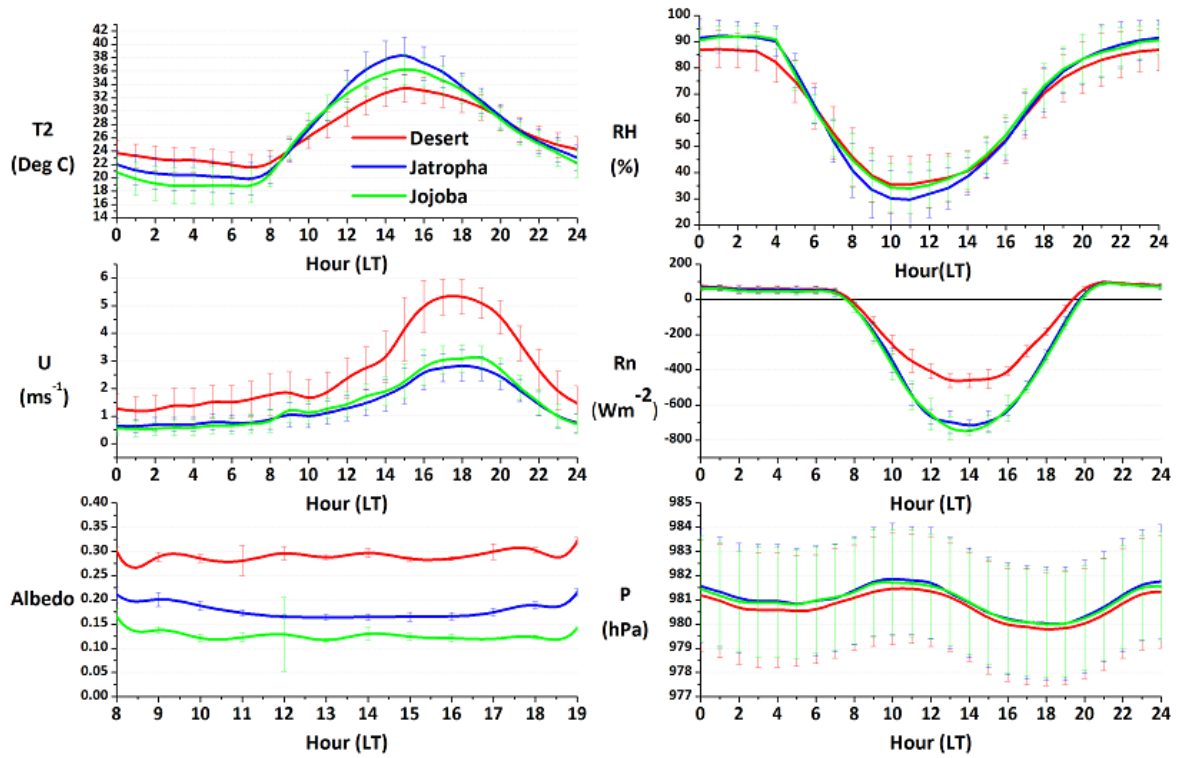


Figure 6.4: Observed mean diurnal cycle of T_{2m} [$^{\circ}\text{C}$], RH [%], U_{6m} [m s^{-1}], R_N [W m^{-2}], Albedo and P [hPa] for summer 2012 (JJA). The error bars represent temporal standard deviation.

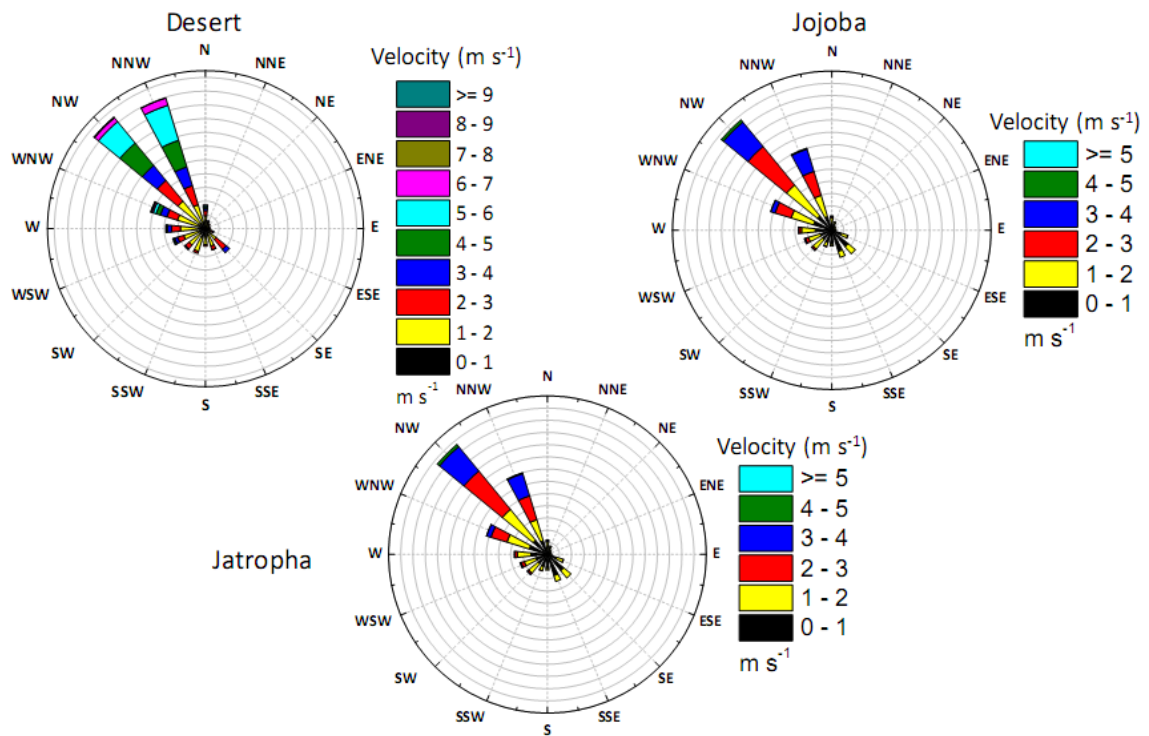


Figure 6.5: Israel - observed wind field over *Desert*, *Jojoba* and *Jatropha* for summer 2012 (JJA) [m s^{-1}]. Sensors are approximately 4 m above ground or canopy. Bars are split according to proportion of number of events.

6.2 Penman Monteith evapotranspiration models

The following are methods were used to calculate mean diurnal crop ET over JJA of 2012. See Branch et al. (2014) for a more detailed description of how it was implemented with the meteorological data.

6.2.1 Penman-Monteith 56 FAO equation

The following expression is the Penman 56 FAO, using a crop coefficient K_c to modify ET_0 :

$$ET_0 = \frac{0.408\Delta(R_N - Q_G) + \lambda_{psy} \left(\frac{900 [^\circ\text{C}]}{T_{2m} + 237.16 [^\circ\text{C}]} \right)}{\Delta + \lambda_{psy} (0.34 U_z + 1 \left[\frac{m}{s} \right]) \left[\frac{s}{m} \right]} \quad (6.1)$$

where ET_0 is the reference evapotranspiration of a well-irrigated cut grass crop [mm d^{-1}], Δ is the slope of e_s against T [kPa K^{-1}], $(R_N - Q_G)$ is the net available radiation [MJ d^{-1}], λ_{psy} is the psychrometric constant [kPa K^{-1}], and U_z is the wind speed at standard height [m s^{-1}]. ET_0 is then modified to crop ET (ET_c) using a crop coefficient K_c (For Jojoba, 0.7).

6.2.2 Penman-Monteith R_a/R_s equation

The second method, Penman R_a/R_s is calculated as:

$$ET_c L_v = \frac{\Delta(R_N - Q_G)}{(\Delta + 1 \left[\frac{\text{kPa}}{\text{K}} \right])} + \frac{\frac{\rho_a C_P (e_s - e_a)}{R_a}}{\Delta + \lambda_{psy} \left(1 + \frac{R_s}{R_a} \right)} \quad (6.2)$$

where ET_c is the crop ET (mm d^{-1}) when multiplied with the vegetation fraction, L_v is the latent heat of vaporization [J kg^{-1}], $R_N - Q_G$ is the available radiation [W m^{-2}], e_s and e_a are saturated and actual water vapor pressures respectively [kPa]. R_s and R_a are the surface and aerodynamic resistances respectively [s m^{-1}] and defined as:

$$R_s = \frac{R_{st,bulk}}{LAI_{eff}} \quad (6.3)$$

and

$$R_a = \frac{\ln \left(\frac{Z-d}{Z_{0m}} \right) \ln \left(\frac{Z-d}{Z_{0h}} \right)}{k^2 U_z} \quad (6.4)$$

In Equation 6.3, $R_{st,bulk}$ is a bulk stomatal resistance [$s\ m^{-1}$] and LAI_{eff} is effective leaf area index (usually $LAI/2$) [$m^2\ m^{-2}$], and k is the von Karman constant [-]. In Equation 6.4, Z is the standard measurement height [m], Z_{0h} and Z_{0m} are roughness heights for water vapor and momentum, respectively [m]. Estimation methods for d , Z_{0m} , Z_{0h} were suggested by Allen (1998) as $d=2/3h_c$, $Z_{0m}=0.123h_c$ and $Z_{0h}=0.1Z_{0m}$, assuming equivalent roughness heights for vapour and heat and where h_c is the canopy height [m].

6.3 Plots of mean max turbulent fluxes over plantation

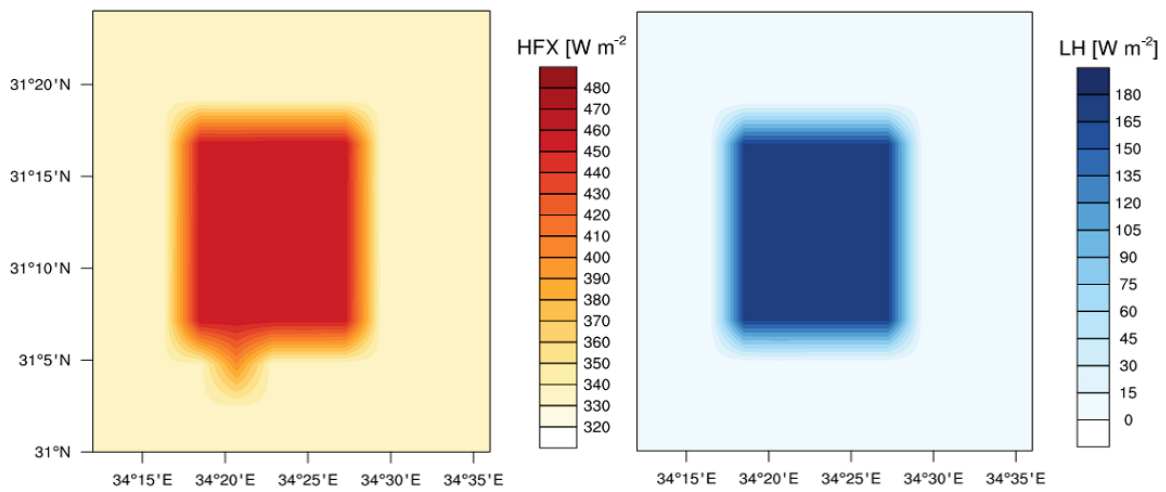


Figure 6.6: Mean daily maximum of sensible and latent heat fluxes in WRF Impact (JJA) to show the spatial gradient between the 10×10 km plantation and the surrounding desert. Values of Q_H over plantation and desert are around 460 and 330 $W\ m^{-2}$ respectively, which is a 130 $W\ m^{-2}$ gradient. Values of Q_E over the plantation and desert are respectively 165 and 0 $W\ m^{-2}$ which is a 165 $W\ m^{-2}$ gradient..

6.4 Climate station data sources

Table 6.1: Climate data source for station point analysis (Chapter 4)

Station	Station code	Source	Data range
Boolathana	GHCND:ASN00006003	NOAA Monthly summaries	1992-2012
Badingarra	GHCND:ASN00009037	NOAA Monthly summaries	1992-2012
Antofagasto	GHCND:CI000085442	NOAA Monthly summaries	1992-2012
Ajo	GHCND:USW00053168	NOAA Monthly summaries	2010-2014
Escondido	GHCND:USC00042863	NOAA Monthly summaries	1992-2012
Ensenada	GHCND:MX000002072	NOAA Monthly summaries	1978-1998
La paz	GHCND:MX000003074	NOAA Monthly summaries	1992-2012
Beer'sheva	GHCND:IS000051690	NOAA Monthly summaries	1985-2005
Masirah	GHCND:MU000041288	NOAA Monthly summaries	1992-2012
Rajkot	GHCND:IN005150100	NOAA Monthly summaries	1992-2012
Jaipur	GHCND:IN019131301	NOAA Monthly summaries	1992-2012
Bir Moghrein	GHCND:MR000061401	NOAA Monthly summaries	1992-2012
Sesfontein	GHCND:WA010472480	NOAA Monthly summaries	1965-1985
Gobabeb	GHCND:WA006490640	NOAA Monthly summaries	1992-2012

6.5 Climate variance maps - 1979-2012 - $\Gamma_{700-500}$, $q_{s,925}$, C_v

Here the standard deviations of $\Gamma_{700-500}$, $q_{s,925}$, and ICV are plotted to provide insight into regional variability over thirty three years of the three climate suitability indicators.



Figure 6.7: Africa - standard deviation (σ_{dev}) of $\Gamma_{700-500}$, $q_{s,925}$, ICV - ERA-Interim - 1979-2012 - January and July.

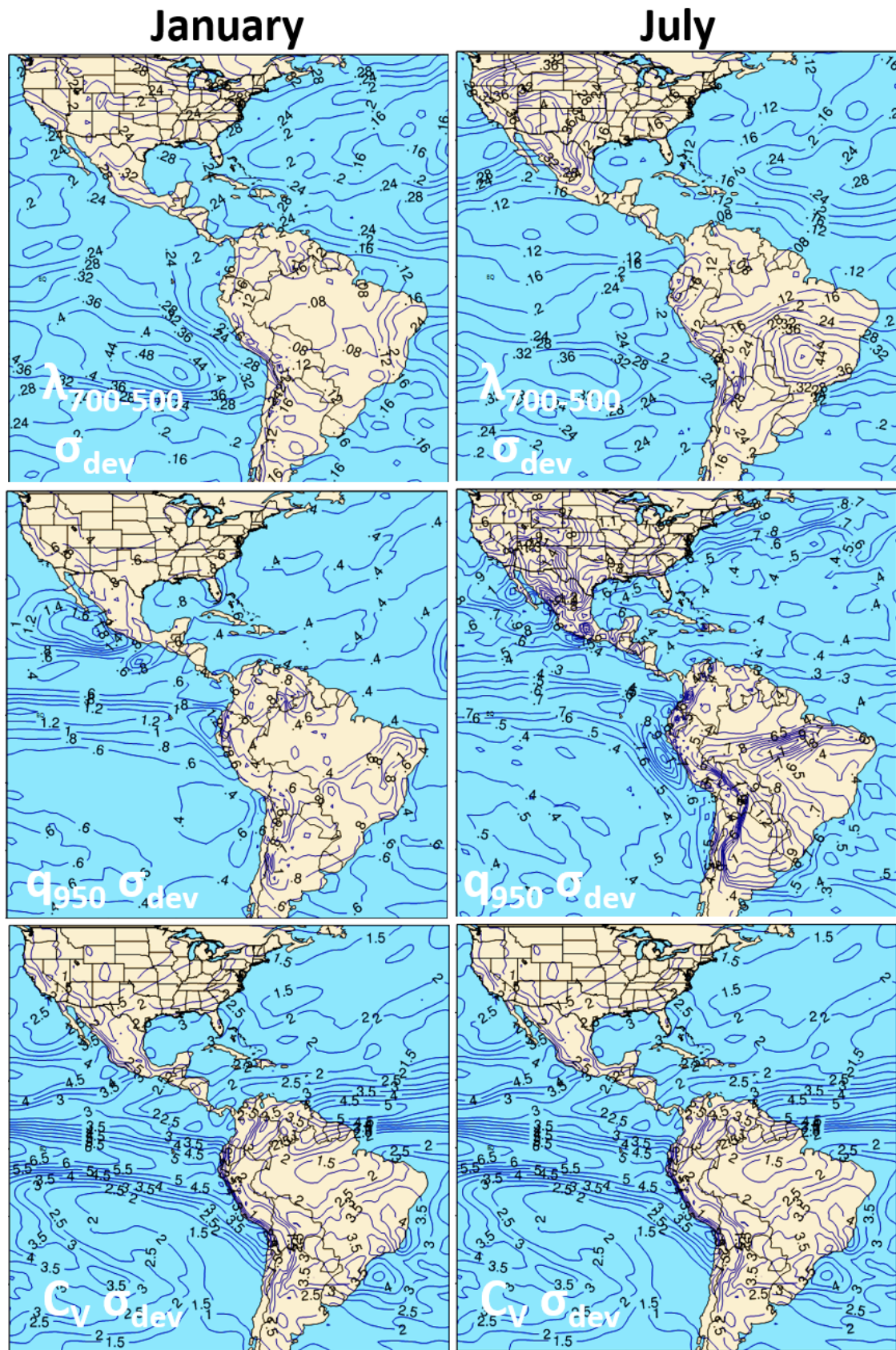


Figure 6.8: Americas - standard deviation (σ_{dev}) of $\Gamma_{700-500}$, $q_{s,925}$, ICV - ERA-Interim - 1979-2012 - January and July.

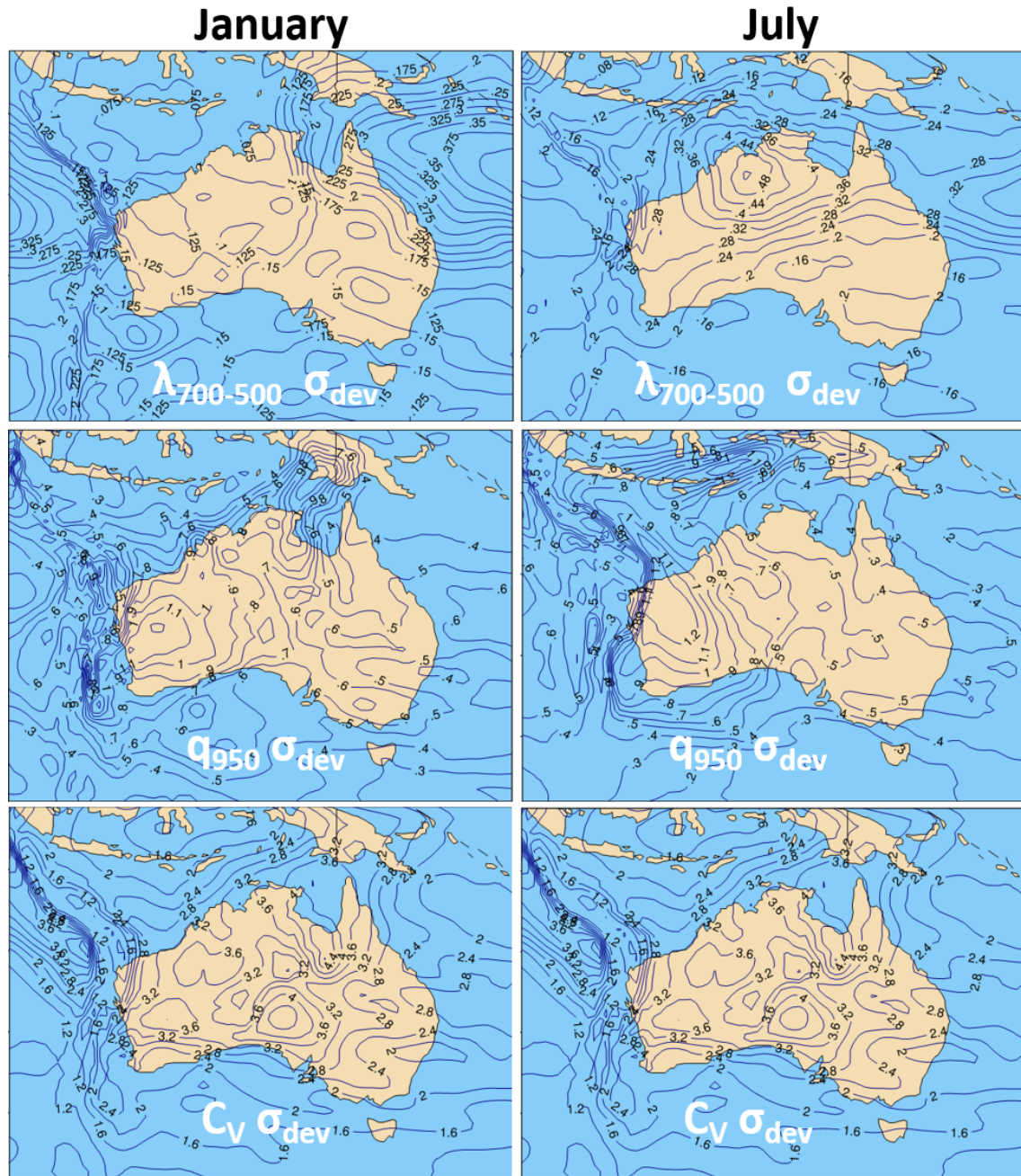


Figure 6.9: Australia - standard deviation (σ_{dev}) of $\Gamma_{700-500}$, $q_{s,925}$, ICV - ERA-Interim - 1979-2012 - January and July.



Figure 6.10: Africa - coefficient of variance (COV) $\left[\frac{\sigma_{dev}}{mean} \right]$ for $\Gamma_{700-500}$, $q_{s,925}$, ICV - ERA-Interim - 1979-2012 - January and July.

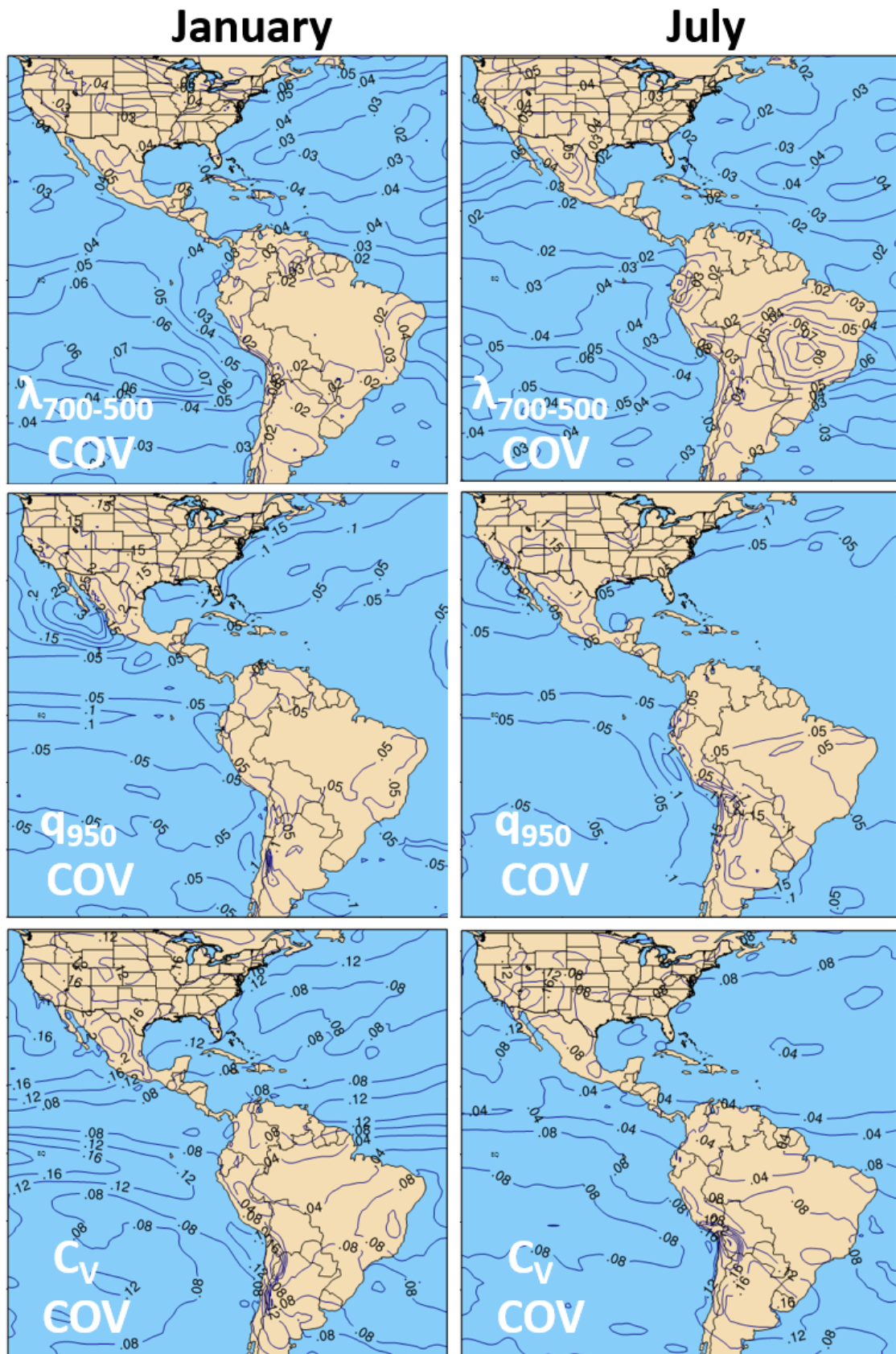


Figure 6.11: Americas - coefficient of variance (COV) $\left[\frac{\sigma_{dev}}{mean}\right]$ for $\Gamma_{700-500}$, $q_{s,925}$, ICV - ERA-Interim - 1979-2012 - January and July.

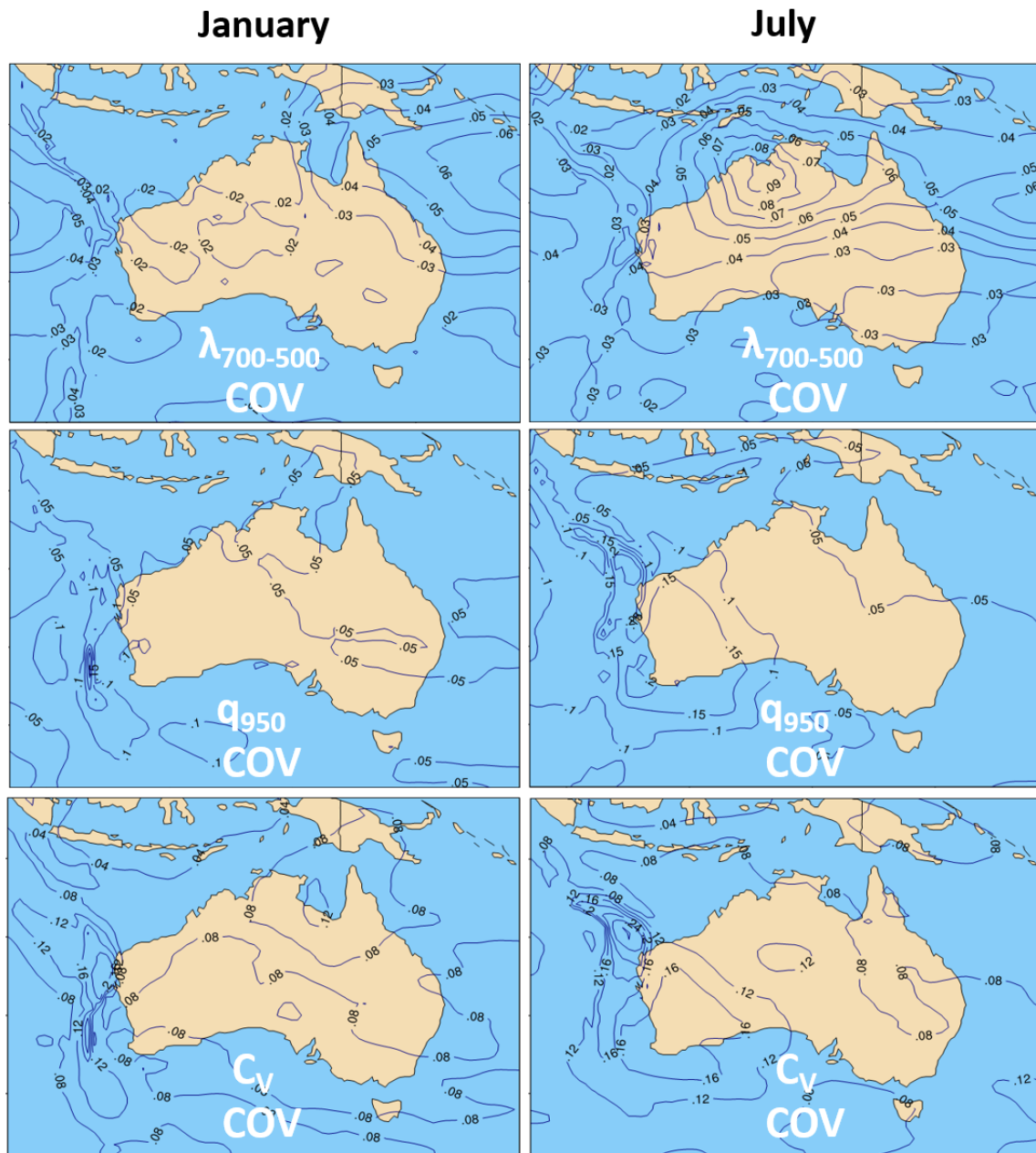


Figure 6.12: Australia - coefficient of variance (COV) $\left[\frac{\sigma_{dev}}{mean}\right]$ for $\Gamma_{700-500}$, $q_{s,925}$, ICV - ERA-Interim - 1979-2012 - January and July.

6.6 Data and software used

6.6.1 Data

ECMWF Operational analysis data (0.125 °) - Model forcing for all simulations

ECMWF ERA-Interim re-analysis data (0.75 °) - Regional climate analysis

6.6.2 Software

NCAR Command Language. (2013). Boulder, Colorado:

UCAR/NCAR/CISL/VETS. <http://dx.doi.org/10.5065/D6WD3XH5>

- General array analysis/plots - NETCDF and GRIB

VAPOR - a product of the Computational Information Systems Laboratory at the National Center for Atmospheric Research (www.vapor.ucar.edu)

- 3-dimensional visualization

Origin (OriginLab, Northampton, MA)

- General analysis/plots

ESRI 2011. ArcGIS Desktop: Release 9. Redlands, CA: Environmental Systems Research Institute.

- Manipulation of MODIS land surface and FAO soil data

Systat - Systat Software, Inc., San Jose California USA

- Correlations/scatterplots

Acknowledgements

Foremost, I would like to express my sincere gratitude to my advisor Professor Volker Wulfmeyer for his continuous support of my PhD research, enthusiasm for arid climate engineering research, for his valuable criticism, ideas, and immense knowledge

Die Stiftung Energieforschung, Baden-Wurttemberg is gratefully acknowledged for their generous financial backing of this research

I would particularly like to thank Kirsten Warrach-Sagi, Thomas Schwitalla, Hans-Stefan Bauer and Josipa Milovac from the Modelling group for giving their valued knowledge, technical and scientific support and critical analysis

I would also like to thank my other colleagues Elisabeth Ott, Hans-Dieter Wizemann, Andreas Behrendt, Atoussa Bakshai, Simon Metzendorf, Florian Späth, Eva Hammann for support and comradeship at the institute

A special thanks to Alex Geissler for his valued technical expertise on the Israel field campaign

Special thanks to our partners in Israel who provided immense support and goodwill - Shabtai Cohen at Volcani ARO, Dan Yakir at the Weizmann Institute, Nurit Agam, and at Kibbutz Hatzerim/Netafim: Ami Charitan, Opher Silberberg, Ronen Rotschild, Oscar Lutenberg, and Eli Matan

Thanks also to those in Egypt who offered their support even though ultimately our field campaign was not conducted there, especially to Rahid Mikhael and family, Dr. Wagdy Khalil, and the Governorate of Luxor

Love and gratitude to my parents for always being there in good and bad times

Many thanks to Aad and Claudia for their kind support, unceasing enthusiasm and for their hospitality during the writing of my thesis. I could not have completed it without them.

Most of all, thank you to my wife Gele for her love and support over the years and also to my children Hendrik and Emilia for bringing me inspiration and so much joy!

Curriculum Vitae

Personal Data

Name: Oliver Lloyd Branch

Address: Dorotheenweg 11, 70771 Leinfelden-Echterdingen

Date of Birth: 27th June 1972

Citizenship: British

Email: oliver_branch@uni-hohenheim.de

Education

04/2014 - Present Scientist position at Water and Earth System Science (WESS)

11/2011 - 03/2014 PhD student

08/2008 - 11/2011 University of Hohenheim/Copenhagen
Double MSc Environmental Science (ENVEURO)

10/1994 - 07/1997 University of Salford, UK - Bsc (Hons) Audio Engineering

09/1992 - 07/1994 York College of Higher Education, UK
BTEC National Diploma Engineering

09/1983 - 06/1988 Nunthorpe Grammar School, York, UK

Work History

02/2004 - 09/2007 Easy Blue World Diving Centre, Tenerife
Professional PADI Scuba Diving Instructor

12/2003 - 11/2004 Dressel Divers, Playa Del Carmen, Mexico
Professional PADI Scuba Diving Instructor

12/1997 - 12/2003 York Pavilion Hotel, York, UK
Administration/sales/reservations

Publications

Branch, O., Warrach-Sagi, K., Wulfmeyer, V., Cohen, S., 2014. Simulation of semi-arid biomass plantations and irrigation using the WRF-NOAH model - a comparison with observations from Israel. *Hydrology and Earth System Sciences*, 18(5), pp.17611783. Available at: <http://www.hydrol-earth-syst-sci.net/18/1761/2014/>.

Wulfmeyer, V., Branch, O., Warrach-Sagi, K., Bauer, H-S., Schwitalla, T., Becker, K., 2014. The impact of plantations on weather and climate in coastal desert regions. *Journal of Applied Meteorology and Climatology*, p.140117143424003. Available at: <http://journals.ametsoc.org/doi/abs/10.1175/JAMC-D-13-0208.1> [Accessed January 27, 2014].

Erklärung

Hiermit erkläre ich, dass ich die vorgelegte Dissertation selbständig angefertigt und nur die angegebenen Quellen und Hilfsmittel verwendet habe. Wörtlich oder inhaltlich übernommene Stellen sind als solche gekennzeichnet.

Stuttgart, den 31st June 2014

A handwritten signature in blue ink, consisting of several loops and a long horizontal stroke at the bottom.



Anlage 2 zur Promotionsordnung der Universität Hohenheim zum Dr. rer. nat.

Eidesstattliche Versicherung gemäß § 7 Absatz 7 der Promotionsordnung der Universität Hohenheim zum Dr. rer. nat.

1. Bei der eingereichten Dissertation zum Thema

The Impact of Irrigated Biomass Plantations on Mesoscale Climate in Coastal Arid Regions

handelt es sich um meine eigenständig erbrachte Leistung.

2. Ich habe nur die angegebenen Quellen und Hilfsmittel benutzt und mich keiner unzulässigen Hilfe Dritter bedient. Insbesondere habe ich wörtlich oder sinngemäß aus anderen Werken übernommene Inhalte als solche kenntlich gemacht.

3. Ich habe nicht die Hilfe einer kommerziellen Promotionsvermittlung oder -beratung in Anspruch genommen.

4. Die Bedeutung der eidesstattlichen Versicherung und der strafrechtlichen Folgen einer unrichtigen oder unvollständigen eidesstattlichen Versicherung sind mir bekannt.

Die Richtigkeit der vorstehenden Erklärung bestätige ich: Ich versichere an Eides Statt, dass ich nach bestem Wissen die reine Wahrheit erkläre und nichts verschwiegen habe.

Plieningen, 20.06.204

Ort und Datum

Unterschrift

A handwritten signature in black ink, written over a horizontal line. The signature is stylized and appears to be 'C. N. B.'.